Reflection based highly nondegenerate Bi-photon HOM interferometry

A thesis on setup design and Fisher information based optimization

by

Freek Looman

Instructor:	Silvania Pereira
Project Duration:	Februari, 2025 - March, 2026
Faculty:	Faculty of Applied Sciences
Department:	ImPhys

Acknowledgements

The first and foremost person I want to thank, is my supervisor Silvania Pereira. During the past year and a half you have helped me a lot. Thanks for giving me the space and time to work on this project while still making sure I actually finished this thesis. I learned a lot from your expertise and see experimental design from a new perspective after this project. I really enjoyed our talks and discussions about the project and other interesting subjects.

I also want to thank the gentlemen working besides me in the student room. I have seen some students come and go in my time. I will remember my time here fondly, albeit longer than expected.

- The first generation: Jaap, Jonas, Hugo en Han
  voor de diepgaande theoretische overleggen, het productieve netwerken en de bruisende vergaderingen
- The second generation Thijs, Jan, Dion, Sander en Luka
  Voor de grootse gezelligheid, de (ondertussen minder) sfeervolle bonsai bomen en de wijze levenslessen

Good luck with the project/internship/jobhunt and see you all in future bruisende vergaderingen and other wijze levenslessen!

At last, I want to share an anecdote on why AI will not just yet be taking the jobs for experimental physicists. while coding I asked chatGPT for some help on my code. I thought it would generate code for making a figure. Instead it generated something resembling an optical diagram for my experiment. The longer you look, the worse it gets. Especially as I never mentioned T or R in any way.

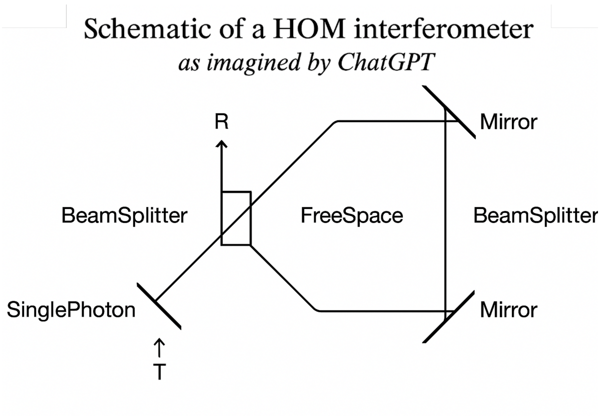

Abstract

The goal of this thesis is to investigate the viability of reflection-based biphoton Hong-Ou-Mandel Interferometry (HOMI) for measuring a sub-nanometer step size. We attempt to push this technology forward by designing for larger separation than has been done before in the literature, resulting in higher possible precision.

This is a Fisher-information-based estimation method. We show that the Quantum Cramér-Rao (QCR) bound can be saturated with our proposed measurement. We propose a mostly common-path interferometer design, where the two optical paths are distinct in polarization instead of spatial mode. This reduces the risk of creating accidental which-path information.

For the production of the photon superposition, we propose a novel biphoton source design specialized for large detuning between the two downconverted wavelengths, similar to the more common beam-displacer entangled photon sources. The proposed photon source can be designed for type-0 and type-II SPDC.

We suggest a detection system based on a combination of visible and NIR single-photon detectors to handle larger detunings than is possible with a single type of detector. The best combination of detectors and type of SPDC was Si-SPAD (visible) and SNSPD (NIR) with weak downconversion focusing ($\xi \ll 1$). This experiment has an expected measurement time of 7.4 seconds for 0.1 nm precision. We conclude that biphoton HOMI is indeed feasible for high-precision metrology.

Contents

Abbreviations and Symbols

Abbreviations

Abbreviation	Definition
GVM	Group Velocity Mismatch
HOM	Hong-Ou-Mandel
HOMI	HOM Interference
HWP	Half-Wave Plate
JSA	Joint Spectral Amplitude
JSI	Joint Spectral Intensity
JTA	Joint Temporal Amplitude
KEM	Knife Edge Mirror
MLE	Maximum Likelihood Estimator
NIR	Near-Infrared
PBS	Polarizing Beam Splitter
ppKTP	Periodically Poled Potassium Titanyl Phosphate
QCR	Quantum Cramér-Rao
QFI	Quantum Fisher Information
QWP	Quarter-Wave Plate
SNSPD	Superconducting Nanowire Single-Photon Detector
SPAD	Single-Photon Avalanche Diode
SPDC	Spontaneous Parametric Down Conversion
TCO	Temperature Controlled Oven

Symbols

Symbol	Definition	Unit
c	Speed of light in vacuum.	[m/s]
D_{si}	Total group velocity dispersion.	[s^2/m]
F	Fidelity. Similarity between a quantum state and a target state.	–
F_τ, F_z	Fisher Information of the delay and step size.	[s^{-2}], [m^{-2}]
L	Length of the nonlinear crystal.	[m]
N	Number of measurement events.	–
P_0, P_1, P_2	Probability of 0, 1 or 2 detectors clicking in case of a downconversion event	–
P_C, P_B	HOMI event outcome probabities	–
Q	Quantum Fisher Information.	–
R_d	Dark count rate of the detector.	[s^{-1}]
R_{si}	Downconverted photon pair rate (brightness).	[s^{-1}]
t_{cw}	Coincidence timing window.	[s]
t_m	Total measurement time.	[s]
u_{si}	Group velocity mismatch (GVM).	[s/m]
w_j	Beam waist of the photon j.	[m]
z, z_{step}	Step depth of reflective surface.	[m]
$\hat{z}$, $\hat{z}_{step}$	Estimated depth of reflective surface.	[m]
α	Experimental visibility.	–
γ	Photon loss probability (subscripts s, i for signal/idler).	–
Δ	Separation in angular frequency between signal and idler.	[rad/s]
$\delta\tau$	Uncertainty/precision of the time delay.	[s]
η	Heralding ratio.	–
κ, κ_{step}	Speed of measurement.	[m^{-2}s^{-1}]
$\lambda_{p,s,i}$	Wavelength (pump, signal, idler).	[m]
ν	Variation in angular frequency around the central frequency.	[rad/s]
ξ_j	Crystal focusing parameter for photon j.	–
σ	Spectral standard deviation in angular frequency.	[rad/s]
τ	Relative temporal delay between paths.	[s]
$\hat{\tau}$	Maximum likelihood estimator of the delay.	[s]
ϕ	Phase between two creation processes / quantum states.	[rad]
$\omega_{p,s,i}$	Angular frequency (pump, signal, idler).	[rad/s]

1

Introduction

The HOM effect is a quantum effect where two indistinguishable photons entering opposite inputs of a beam splitter will always leave the beam splitter at the same output. This is also called photon bunching. The situation where the two photons exit the beam splitter at opposite outputs is generally called a coincidence event, which the HOM effect cancels out.

This effect was first experimentally verified in 1987 [1] by counting the number of coincidences while delaying one incoming photon. The result from this experiment is a dip in coincidences. The HOM effect has been used for new kinds of measurement only in the past 10 years [2, 3, 4].

Leveraging this effect is an interesting direction for high precision optical measurements, as it is known that reaching sub-wavelength precision is quite challenging. In general, the path to achieve high precision is to shorten the wavelength or use high intensities. However, both of these options can be invasive to fragile samples. The experiment we discuss in this thesis is HOM interferometry (HOMI). In HOMI, the illumination is in the visible or near-infrared (NIR) regime and the intensity is measured in photon counts per second, meaning that damaging the sample is not an issue.

This measurement technique has been improved further by the implementation of a Maximum Likelihood Estimator (MLE) based on the gathered Fisher Information [5]. The precision of conventional HOMI using this approach is determined by the linewidth of the light used.

A similar measurement with a twist has been demonstrated by Chen [6]. The twist being that the interacting photons are then prepared in a superposition of wavelengths, Both photons have distinct wavelengths however it is unknown which photon has which wavelength. Such an experiment is called biphoton HOMI. The precision of biphoton HOMI is largely determined by the separation of the two superposed wavelengths instead of the photon bandwidth, allowing for the use of narrow band photons.

Chen build a transmission based interferometer, where they demonstrate they could detect delays introduced by temperature drifts in optical fibers.

The goal of this thesis is to propose a similar optical setup, except our goal is to measure the depth of a reflective surface instead of a transmission-based delay. Additionally, we investigate whether it is realistic to obtain very large wavelength separation between the 2 interacting photons, making for more precise measurements.

This reflection-based measurement is interesting because it is more widely applicable compared to transmission-based setups. The goal will be to reach a precision of 0.1 nm.

Reflection measurements are, in general, more of a challenge due to the higher number of components used. This results in more difficulties in the implementation and alignment of the experiment. Another problem is that non-unity reflection of the sample introduces extra loss compared to transmission-based equivalent setups.

In this thesis, we will suggest a novel method for high-precision measurements, by addressing three main points.

First, we will discuss the theory behind HOMI and adaptations made for large non-degeneracy HOMI. After that, a thorough analysis of the experimental visibility due to superposition overlap is presented. We will finish this part by discussing the theory of producing this non-degenerate superposition.

Secondly, after analyzing several known designs found in the literature, we propose a possible design of the HOM interferometer, including a custom large non-degeneracy biphoton source. We also propose a detection system which allows for both visible and infrared wavelengths, allowing for a larger non-degeneracy.

Finally, we simulate a measurement based on our design and determine optimal operational parameters, which are dependent on the assumed components.

2

Theory

In this chapter, we discuss the theoretical framework behind nondegenerate biphoton HOMI. After that, we will discuss Spontaneous Parametric Down-Conversion (SPDC), which is the physical principle behind our biphoton creation.

2.1. HOM interferomtery

The HOM effect is a quantum effect in which two indistinguishable photons entering opposite inputs of a beam splitter will always leave the beam splitter through the same output. This is also called photon bunching. The situation in which the two photons exit the beam splitter through opposite outputs is generally referred to as a coincidence measurement, which the standard HOM effect suppresses.

2.1.1. Biphoton HOM interferometry

In this thesis, we will discuss the HOM interference pattern for input photons in a frequency superposition. Here, we refer to photons with different frequencies as the signal and idler photons, with wavelengths λ_s and λ_i, respectively. From now on, we also assume $\lambda_s \leq \lambda_i$ by convention. This convention originates from the field of quantum optics; for readability, we maintain it throughout the thesis. The superposition can be described by equation 2.1, where ϕ is the phase between the two states and the subscripts denote the path in which the photon exists. Note that this state is entangled, as it cannot be written as a product of the two independent photon states.

$$|\Phi\rangle = |\lambda_s\rangle_1 |\lambda_i\rangle_2 + e^{i\phi} |\lambda_i\rangle_1 |\lambda_s\rangle_2 \tag{2.1}$$

Later in the thesis, we will describe how we create this state. For now, we state that there are two creation processes, A and B. In creation process A (B), a signal (idler) photon is created in path 1 and an idler (signal) photon is created in path 2. We can experimentally introduce a phase between the two creation processes, meaning we can define the state $|\Phi\rangle = |A\rangle + e^{i\phi}|B\rangle$.

It has been shown that the probability of a coincidence event is given by equation 2.2 [7, 8].

$$P_C = \frac{1}{2} - \frac{1}{2}\cos{(\Delta\tau + \phi)} e^{-2(\sigma\tau)^2} \tag{2.2}$$

Where Δ is defined in angular frequency as $\Delta = \frac{\omega_s - \omega_i}{2}$. σ is the RMS standard deviation of the spectrum, which in this instance is assumed to be normally distributed. It is common to use an odd state where we experimentally choose $\phi = \pi$. This results in the slightly shorter form

$$P_C = \frac{1}{2} + \frac{1}{2}\cos{(\Delta\tau)} e^{-2(\sigma\tau)^2} \tag{2.3}$$

As the only 2 possible outcomes are a bunched measurement or a coincidence measurement, we can also define the probability for a bunched event

$$P_B = 1 - P_C = \frac{1}{2} - \frac{1}{2}\cos{(\Delta\tau)}e^{-2(\sigma\tau)^2} \tag{2.4}$$

From these equations we can gain the following insights:

- The width of the envelope is defined by the spectral width of the photons
- The photons anti bunch at identical arrival time ($\tau = 0$)
- The oscillation is determined by the separation in angular frequency Δ between the 2 photons

These probabilities are idealized, which unfortunately does not perfectly describe how real measurements function. Next, we will introduce three other parameters to take into account more realistic conditions, namely photon loss and experimental visibility.

2.1.2. Accounting for photon loss

Even when both states are perfectly identical, we can still get different outcomes of the experiment. This is due to photon loss in different components. For example, detectors are known to have a low efficiency (SPAD 40%, SNSPD 95%). For example, if we have a coincidence event and we lose one of the photons, we only see one detector clicking. Because of this, we need to introduce γ, the probability a photon does not get measured. Now that we have calculated what the probability for a bunched measurement is, and for a coincidence measurement, we can calculate the chances of 0, 1 and 2 of our detectors clicking in the event of down-conversion. [9, 6]

$$\begin{pmatrix} P_0(\tau) \\ P_1(\tau) \\ P_2(\tau) \end{pmatrix} = \begin{pmatrix} \gamma^2 & \gamma^2 \\ 2\gamma(1-\gamma) & 1-\gamma^2 \\ 1-2\gamma(1-\gamma)-\gamma^2 & 0 \end{pmatrix} \cdot \begin{pmatrix} P_c(\tau) \\ P_b(\tau) \end{pmatrix}. \tag{2.5}$$

Solving these equations we get:

$$\begin{aligned} P_2(\tau) &= \tfrac{1}{2}(1-\gamma)^2\left[1 + a\cos(\Delta\tau)e^{-2\sigma^2\tau^2}\right] \\ P_1(\tau) &= \tfrac{1}{2}(1-\gamma)^2\left[\tfrac{1+3\gamma}{1-\gamma} - a\cos(\Delta\tau)e^{-2\sigma^2\tau^2}\right] \\ P_0(\tau) &= \gamma^2, \end{aligned} \tag{2.6}$$

These equations are already well known in the industry. However, in our case, we are interested in a larger detuning Δ between our signal and idler photons. This can result in our detectors or components having different photon losses for the signal and idler photons. That is why we now introduce γ_s and γ_i, which are the photon losses for the signal and idler photons. We can now do a similar calculation as above by redefining the loss matrix. This results in

$$\begin{pmatrix} P_0(\tau) \\ P_1(\tau) \\ P_2(\tau) \end{pmatrix} = \begin{pmatrix} \gamma_s\gamma_i & \gamma_s\gamma_i \\ \gamma_s(1-\gamma_i)+\gamma_i(1-\gamma_s) & 1-\gamma_s\gamma_i \\ 1-[\gamma_s\gamma_i]-[\gamma_s(1-\gamma_i)+\gamma_i(1-\gamma_s)] & 0 \end{pmatrix} \cdot \begin{pmatrix} P_c(\tau) \\ P_b(\tau) \end{pmatrix} \tag{2.7}$$

which simplifies to

$$\begin{pmatrix} P_0(\tau) \\ P_1(\tau) \\ P_2(\tau) \end{pmatrix} = \begin{pmatrix} \gamma_s\gamma_i & \gamma_s\gamma_i \\ \gamma_s+\gamma_i-2\gamma_s\gamma_i & 1-\gamma_s\gamma_i \\ (1-\gamma_s)(1-\gamma_i) & 0 \end{pmatrix} \cdot \begin{pmatrix} P_c(\tau) \\ P_b(\tau) \end{pmatrix}. \tag{2.8}$$

and once again, solving this matrix multiplication results in

$$\begin{aligned} P_2(\tau) &= \tfrac{1}{2}(1-\gamma_s)(1-\gamma_i)\left[1 + a\cos(\Delta\tau)e^{-2\sigma^2\tau^2}\right] \\ P_1(\tau) &= \tfrac{1}{2}(1-\gamma_s)(1-\gamma_i)\left[\tfrac{1+\gamma_s+\gamma_i-3\gamma_s\gamma_i}{(1-\gamma_s)(1-\gamma_i)} - a\cos(\Delta\tau)e^{-2\sigma^2\tau^2}\right] \\ P_0(\tau) &= \gamma_s\gamma_i \end{aligned} \tag{2.9}$$

These equations form the basis of this thesis.

2.1.3. Determining the HOM visibility

During the measurement, our photon states can degrade, resulting in both inputs of the HOM beam splitter having different states. This results in a loss of experimental visibility, represented by the parameter α. The assumption made is that when the states are not equal, a coincidence and a bunched event have equal probability again.

Most sources state that the strength of the HOM effect is determined by the indistinguishability between the two incoming photons:

$$\alpha = |\langle \Phi_1 \,|\, \Phi_2 \rangle| \tag{2.10}$$

where $|\Phi_{1/2}\rangle$ is the state of the photon in input arm 1/2 of the HOM beam splitter. However, this leaves some room for interpretation in how we can estimate the visibility given two states. In general, we have two photon creation processes, A and B. Process A sends the signal to path 1 and the idler to path 2. Process B does it the other way around. We can then rewrite $|\Phi_{in}\rangle$ using equation 2.1:

$$|\Phi_{in}\rangle = \frac{|A\rangle + e^{i\phi}|B\rangle}{\sqrt{2}} \tag{2.11}$$

We will look at this process from the perspective of the photon creation events A and B, instead of the perspective of arriving photons at the beam splitter.

As you can see, we cannot easily compare both photon sources when comparing the input states at path 1 and 2. A thorough derivation of the biphoton HOM effect from two different creation processes has not been found in the literature. Our goal is not to derive the overall interaction, but to define the effects of small differences in both processes A and B.

Next, we need to introduce the parameters by which the photons from the two processes can be distinguished. One example of distinguishable photons is two photons of the same central frequency, where one has a Gaussian spectrum and the other has a skewed spectrum. In that case, there exists a slight distinguishability between the photons, albeit only partial. We will account for the following properties of the entangled state:

- Polarization
- Spectrotemporal
- Spatial

Now, we can investigate the total Hilbert space containing all these properties for the photons by taking the tensor product of each:

$$\mathcal{H} = \mathcal{H}_{polarization} \otimes \mathcal{H}_{spectrotemporal} \otimes \mathcal{H}_{spatial} \tag{2.12}$$

We can only find the distinguishability when we introduce the possibility for our creation processes to be different. We define the parameter $\bar{x}$ as the collection of parameters which can introduce distinguishability.

From here on out, we start defining our dependent variables represented by $\bar{x}$. The resulting amplitude, completely written out, reads:

$$\bar{x} = \{\nu_s, \nu_i, \tau_s, \tau_i, J_s, J_i, \bar{r}_s, \bar{r}_i\} \tag{2.13}$$

Here $\nu_{s/i} = \omega_{s/i} - \omega^0_{s/i}$ is the variation in angular frequency around the nominal signal/idler angular frequency $\omega^0_{s/i}$. $\tau_{s/i}$ is the signal/idler arrival time, $J_{s/i}$ is the polarization state, and finally $\bar{r}_{s/i}$ is the spatial amplitude.

Based on this, we introduce the state amplitudes $\mathcal{A}(\bar{x})$ and $\mathcal{B}(\bar{x})$ for creation processes A and B respectively. We then define:

$$|A\rangle = \iint d\bar{x} \left[\mathcal{A}(\bar{x}) \hat{a}_1^\dagger(\omega_s, \bar{x}) \hat{a}_2^\dagger(\omega_i, \bar{x}) |0\rangle \right] \tag{2.14}$$

Similarly:

$$|B\rangle = \iint d\bar{x} \left[\mathcal{B}(\bar{x}) \hat{a}_1^\dagger(\omega_i, \bar{x}) \hat{a}_2^\dagger(\omega_s, \bar{x}) |0\rangle \right] \tag{2.15}$$

Do note that these states take into account that Process A creates a signal photon in path 1 and an idler photon in path 2. Process B has the photons the other way around.

Next up, we state that these amplitudes are normalized:

$$\iint \mathcal{A}^*(\bar{x}) \mathcal{A}(\bar{x}) d\bar{x} = 1 \tag{2.16}$$

We derived the coincidence probability, given two distinct creation processes, in Appendix A.2. This derivation uses the simpler degenerate HOM derivation as a reference, which can be found in Appendix A.1. Here we found the following coincidence probability:

$$P_c = \frac{1}{2} - \frac{1}{2} \cos(\Delta\tau + \phi) \left| \iint d\bar{x} \mathcal{A}^*(\bar{x}) \mathcal{B}(\bar{x}) \right| \tag{2.17}$$

Calculating each overlap

The distributions $\mathcal{A}(\bar{x})$ and $\mathcal{B}(\bar{x})$ over many parameters are not all that convenient. To solve equation 2.17 we introduce partial amplitudes that are handy, namely:

- $\mathcal{A}_\nu(\nu_s, \nu_i)$: joint spectral amplitude (JSA)
- $\mathcal{A}_\tau(\tau_s, \tau_i)$: joint temporal amplitude (JTA)
- $\mathcal{A}_p(J_s, J_i)$: polarization state
- $\mathcal{A}_{\bar{r}}(\bar{r}_s, \bar{r}_i)$: spatial mode

We can find the partial distributions by integrating over all other variables. For example, the signal spectrum $\mathcal{A}_{\nu_s}(\nu_s)$ can be found by integrating over parameter space $\bar{y} = \bar{x} \setminus (\nu_s) = \{\nu_i, \tau_s, \tau_i, J_s, J_i, \bar{r}_s, \bar{r}_i\}$:

$$\mathcal{A}_\nu(\nu_s) = \iint d\bar{y} \mathcal{A}(\nu_s, \bar{y}) \tag{2.18}$$

Each of these partial amplitudes can be described easily for both creation events. One can calculate the overlap in that specific property. This gives you a helpful upper bound to the experimental visibility.

One assumption we will be making is that the parameters are independent. This will result in our partial integrals being separable. We assume the independence of the spectral and spatial distribution. Working with a small linewidth, meaning small ν, will not result in different spatial characteristics due to refractive effects. It is also assumed that the polarization and spatial mode are independent. One dependency we need to address is that of the photon arrival times $\tau_{s/i}$ on the spectral characteristics ν, which are determined by the spectral amplitude. This will be discussed later in this section. The creation process is not the only thing influencing the temporal amplitude; other optical components can also introduce wanted and unwanted delays due to refractive elements. Accounting for these kinds of dependencies, we can rewrite:

$$\mathcal{A}(\bar{x}) = \mathcal{A}_{\nu,\tau}(\nu_s, \nu_i, \tau_s, \tau_i) \mathcal{A}_p(J_s, J_i) \mathcal{A}_r(\bar{r}_s, \bar{r}_i) \tag{2.19}$$

Starting here, we will discuss how we calculate each of these separable amplitudes.

Polarization overlap

While this framework does allow for complex polarization distributions, we simply assume perfectly linearly polarized light in this thesis. This assumption reduces our integral to the inner product between the signal and idler polarization $J_{a/b,s/i}$ of both sources:

$$\iint dJ_s dJ_i \left[\mathcal{A}_p^*(J_s, J_i) \mathcal{B}_p(J_s, J_i) \right] = (J_{a,s}^* J_{b,s}) \cdot (J_{a,i}^* J_{b,i}) \tag{2.20}$$

Spatial overlap

Spatial overlap refers to the degree of overlap between the signal and idler photons created by both processes. We will describe this spatial information only qualitatively, as it is primarily dependent on beam shape and alignment.

The experimental visibility depends on the beam overlap. The signal and idler photon beams of both processes need to be well aligned. We will not quantitatively analyze the effects of alignment on visibility; however, we will discuss the ease of alignment when we present the suggested experimental setups in Chapter 3 of this thesis.

Identical beam shapes or, equivalently, spatial modes are also important. Conventionally, single-mode fiber-coupled detectors are used in entanglement research [5, 10]. This removes any spatial information that might introduce accidental distinguishability. One disadvantage of this technique is that it filters out most other spatial modes, which might still hold information. For this reason, we will not assume the use of single-mode fibers in this thesis. Another reason to avoid single-mode fibers is that the coupling efficiency is highly dependent on precise alignment.

One more effect to consider, other than the spatial overlap between the two creation processes, is the general shape of the beams. It has been shown that the interference behavior is dependent on the Hermite-Gaussian modes [11]. This dependency is determined by the parity (oddness or evenness) of the Hermite-Gaussian mode along the transverse axis of the beam splitter, which conventionally corresponds to the horizontal axis. Odd spatial modes will have a peak whenever an even spatial mode has a dip, and vice versa. An equal mix of both odd and even spatial modes will therefore cancel each other out. Selecting only even (or only odd) modes is therefore highly important.

Spectrotemporal overlap

Here we quantify our earlier example of two photons having differently shaped spectra. We assume that for both processes A and B, the signal/idler photons have amplitudes $\mathcal{A}_\nu(\nu_s,\nu_i)$ and $\mathcal{B}_\nu(\nu_s,\nu_i)$, where $\nu_{s/i}=\omega_{s/i}-\omega_{s/i,0}$ is the spectrum with respect to the central frequency $\omega_{s/i,0}$:

$$\iint \mathcal{A}_\nu^*(\nu_s,\nu_i)\mathcal{B}_\nu(\nu_s,\nu_i)d\nu_s d\nu_i \tag{2.21}$$

One assumption we will be making is that we have an infinitesimally small pump linewidth. This means that conservation of energy holds strictly, $\omega_p=\omega_s+\omega_i$, resulting in both amplitudes containing the delta function $\delta(\omega_p-\omega_s-\omega_i)$. When we substitute for $\nu_{s/i}$, we get $\delta(\nu_i+\nu_s)$, meaning $\nu_i=-\nu_s$. This directly relates the signal and idler spectral amplitudes, so we can describe the whole spectral amplitude with a single variable, for which we choose ν_s. From now on, we will implicitly assume this, so we can write:

$$\iint \mathcal{A}_\nu^*(\nu_s,\nu_i)\mathcal{B}_\nu(\nu_s,\nu_i)d\nu_s d\nu_i = \int \mathcal{A}_{\nu_s}^*(\nu_s)\mathcal{B}_{\nu_s}(\nu_s)d\nu_s \tag{2.22}$$

This is not a calculation we directly use for calculating the experimental visibility; however, one can evaluate an upper bound for it using this spectral overlap. As discussed before equation 2.19, the temporal and spectral amplitudes are dependent, meaning we need to integrate over both parameters to arrive at the visibility.

The temporal information is encoded in the phase of $\mathcal{A}_\nu(\nu_s)$. This spectral amplitude is related by the Fourier transform to the temporal one, $\mathcal{A}_\tau(\tau_-)$ [12]. Here τ_- is the arrival time difference between the signal and idler photon. In this thesis, we used this temporal form to more intuitively explain the shape of the envelope in $P_c(\tau)$, as defined in equation 2.2, for any spectral distribution. This explanation can be found in Appendix B.

2.2. Fisher information based measurement

Now that we have discussed the basics of the HOM effect, we want to know how well we can actually measure a path delay. In this section, we will use the concept of Fisher information to quantify the precision of our measurement. We will start by looking at the Quantum Cramér-Rao bound to find the fundamental limit of our biphoton state. After that, we will introduce a classical estimator to see how we can reach this limit using our experimental results. Finally, we will define the ”speed of measure” to see how fast we can perform these measurements in a real-world scenario.

2.2.1. Quantum Cramér-Rao Bound

The Quantum Cramér-Rao (QCR) bound gives the lowest possible uncertainty for a measurement of a state [13]. A measurement $\hat{\tau}$ of a temporal delay τ has its uncertainty $\delta\tau$ bounded by the QCR bound $\delta\tau_{QCR}$. For a given state, the QCR bound is given by:

$$\delta\tau \geq \delta\tau_{QCR} = \frac{1}{\sqrt{NQ}} \tag{2.23}$$

where N is the number of measurements and Q is the Quantum Fisher Information (QFI) of the state of interest. This can be seen as the maximum possible information gatherable on a predefined parameter from the quantum state [6, 14].

A measurement saturating this bound is called quantum-limited.

Our state of interest is the biphoton wavelength superposition defined in equation 2.1, and our parameter of interest is the path delay τ. The QCR bound for measuring a time delay has been calculated [6] and is of the form:

$$\delta\tau_{QCR} = \frac{1}{\sqrt{N}} \frac{1}{\sqrt{\Delta^2 + 4\sigma^2}} \tag{2.24}$$

The measurement precision is dependent on both the angular spectral width σ and the angular separation between the signal and idler frequencies Δ.

This also shows why we are interested in biphoton HOM interferometry. Our precision is dependent on the separation of the two frequencies, and not, as is conventional, on the width of the spectrum.

2.2.2. Fisher information and maximum likelihood estimator

Now that we have discussed the implications of the QCR bound, the next logical step is to examine what can be determined from the classical Cramér-Rao bound. Similarly to the QCR, the classical Cramér-Rao (CR) bound represents the fundamental limit in precision for any estimator $\hat{\tau}$ grounded in classical counting.

Any estimator satisfies the Cramér-Rao bound:

$$\delta\tau_{CR} \geq \delta\tau_{QCR} \tag{2.25}$$

The CR bound defines the minimum uncertainty for a measurement based on classical statistics as follows:

$$\delta\hat{\tau} \geq \delta\tau_{CR} = \frac{1}{\sqrt{N}} \frac{1}{\sqrt{F_\tau}} \tag{2.26}$$

where N is the number of measurements and F_τ is the Fisher Information of a single measurement. F_τ for our model containing distinct photon losses γ_s and γ_i is shown in equation 2.27. The derivation can be found in Appendix C.1.

$$F_\tau = \frac{(1-\gamma_s\gamma_i)\alpha^2 \left[\Delta \sin(\Delta\tau) + 2\sigma^2\tau\cos(\Delta\tau)\right]^2 e^{-4\sigma^2\tau^2}}{\left[\frac{3\gamma_s - 1}{1-\gamma_s} + \frac{2}{1-\gamma_i} - \alpha\cos(\Delta\tau)e^{-2\sigma^2\tau^2}\right]\left[1 + \alpha\cos(\Delta\tau)e^{-2\sigma^2\tau^2}\right]} \tag{2.27}$$

Here τ is the relative delay between the two paths, Δ is the detuning in angular frequency between the signal and idler photon, σ is the down-converted linewidth in angular frequency, and α is the experimental visibility.

The estimator of choice is the Maximum Likelihood Estimator (MLE) [15]. This estimator is widely used in the field of statistics and possesses several desirable qualities. It can be analytically determined and is consistent, meaning it is theoretically perfectly accurate in the limit of large N. Most importantly, it saturates the CR bound, meaning the inequality in equation 2.26 becomes an equality for this estimator.

We will build our estimator based on the quantities we can actually detect: the measured number of events where both detectors click (N_2) and the number of events where one detector clicks (N_1). The number of events is determined by our assumed probabilities defined in equations 2.9. The following MLE $\widehat{\tau}$ has been derived:

$$\widehat{\tau} = \frac{1}{\Delta}\arccos\left(\frac{\left(\frac{3\gamma_s-1}{1-\gamma_s}+\frac{2}{1-\gamma_i}\right)N_2 - N_1}{\alpha(N_1+N_2)e^{-2\sigma^2\tau_s^2}}\right) \tag{2.28}$$

where τ_s is our rough temporal delay set by a delay station. The derivation of our MLE $\widehat{\tau}$ can be found in Appendix C.2.

Both the Fisher Information and $\widehat{\tau}$, along with the outcomes, can be seen in Figure 2.1 for a previously realized near-degenerate experiment [6]. We can draw some interesting takeaways from this.
First, the Fisher Information is largest at its peaks closest to zero path delay. Second, we see that our estimator $\widehat{\tau}$ only maps to the range $\left[0, \frac{2\pi}{\Delta}\right]$. This results in our dynamic range being limited by $\frac{2\pi}{\Delta}$; otherwise, we run into the problem of ambiguity.

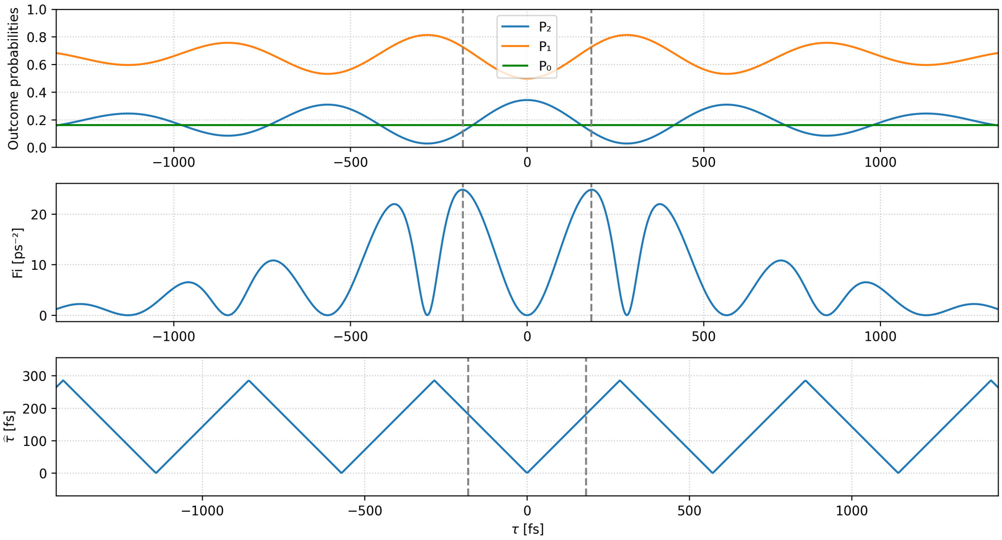

Figure 2.1: Analytical near-degenerate HOMI experiment simulation. Each horizontal axis shows the same path delay. The top figure shows outcome probabilities, the second shows the Fisher Information, and the last shows the calculated $\widehat{\tau}$ assuming no noise on the measurement outcomes. The gray dashed lines show the delay for which the Fisher Information is maximized. Other parameters are $\alpha = 0.9$, $\gamma_s = \gamma_i = 0.4$, $\Delta = 1.75$ THz, and $\sigma = 0.253$ THz.

There is one small detail we skipped over. In equation 2.26, we define the number of measurements N. One might assume that, since we measure N_2 and N_1, the total number of measurements is $N_2 + N_1$. However, in our probabilities, we also considered the case where no photons are detected in an event (P_0). This requires us to include N_0 in the total count. Given that we can estimate our photon losses γ_s and γ_i, we can estimate the total number of photon events for our CR bound to be:

$$N = N_2 + N_1 + N_0 \approx \frac{N_2 + N_1}{1 - \gamma_s\gamma_i} \tag{2.29}$$

The final step is to validate that this measurement is quantum-limited. We already know that $\widehat{\tau}$ saturates the CR bound. If we now assume perfect conditions ($\alpha = 1$ and $\gamma_{s/i} = 0$) and choose our rough delay τ_s optimally, we get:

$$F_\tau = \Delta^2 + 4\sigma^2 \tag{2.30}$$

If we combine this with equation 2.26, we see that we also saturate the QCR bound for the biphoton state in equation 2.24. We can conclude that this measurement scheme is quantum-limited.

2.2.3. Step size measurement from temporal delay

Up to this point, we have discussed the temporal delay τ. However, our goal is to measure a step size $z = \frac{c}{2}\tau$ in nanometers. The step size estimator $\widehat{z}$ and Fisher information can be derived as:

$$\begin{aligned} \widehat{z} &= \frac{c}{2}\widehat{\tau} \\ F_z &= \left(\frac{c}{2}\right)^{-2} F_\tau \end{aligned} \tag{2.31}$$

To make the measurement easier, we will determine the size of the step based on two measurements. Once we have estimated all the parameters, we can begin the measurement. First, we determine the delay for which the Fisher Information is maximized. Then, we will measure for some time t_m at this setting.

We measure the step in a relatively simple way. We assume our step is smaller than the precision of our delay, and that the shift due to this step does not significantly change the delay at which the Fisher Information is maximized. From here, we perform two measurements with a measurement time t_m: one without the step and one with the step. The size of the step is then:

$$\widehat{z}_{\text{step}} = \widehat{z}_1 - \widehat{z}_0 = \frac{c}{2}(\widehat{\tau}_1 - \widehat{\tau}_0) \tag{2.32}$$

Note that a single position measurement is bounded by the QCR bound z_{QCR}. Assuming the two position measurements are independent, we can estimate the standard deviation of our step size estimator to be:

$$\text{Std}[\widehat{z}_{\text{step}}] \leq \sqrt{2} z_{\text{QCR}}(t_m) \tag{2.33}$$

2.2.4. Speed of measurement

The precision of a measurement is based on the information per measurement event (Fisher Information) and the number of events per second. In the literature, we see that most researchers maximize the Fisher Information for HOM interferometry measurements [6, 5]. In this section, we introduce a new parameter, the speed of measurement κ. This quantity is based on the CR bound of our estimator precision and the number of events per second, resulting in:

$$\text{Std}[\widehat{z}] \leq \sqrt{\frac{1}{\kappa t_m}} \tag{2.34}$$

where t_m is the measurement time and Std$[\widehat{z}]$ is the estimation precision. We can calculate κ from the Fisher Information and the photon rate R_{HOM}, which we define as:

$$\kappa \equiv F_z R_{HOM} \tag{2.35}$$

κ is given in units of m^{-2}s^{-1}. Similarly, for the measurement speed of the step size, we get:

$$\kappa_{\text{step}} = \frac{1}{2} F_z R_{HOM} \tag{2.36}$$

This quantity is more directly related to how well your measurement performs compared to using the Fisher Information alone. Therefore, we will maximize this quantity.

2.3. Spontaneous Parametric Down Conversion

Spontaneous parametric down-conversion is the process where light can be down-converted due to a nonlinearity in a material. This nonlinearity is different for different kinds of crystals. In general, this process is performed in birefringent materials, where the index of refraction is dependent on the polarization of the light with respect to the crystal. There are multiple different kinds of materials you can use, such as BBO LN and KTP. During this thesis, we will focus on KTP, as it is known for having a relatively temperature-stable and high down-conversion brightness.

This down-conversion process can also be described on the single-photon level. We will do this in this chapter, so we can discuss how different processes result in different kinds of visibility. At first, we look at what kind of interactions can happen. We are only interested in collinear down-conversion, where the down-converted photons propagate in the exact same direction as the pump photon. These photons need to follow energy conservation, from which we get:

$$\omega_p = \omega_s + \omega_i. \tag{2.37}$$

As can be seen in the figure, momentum conservation determines the angles at which light will be coming out of the crystal. We are interested in the collinear case, meaning all k-vectors are aligned. This means we can treat the momentum as a scalar quantity:

$$\Delta k = k_p - k_s - k_i \tag{2.38}$$

where Δk is the so-called phase mismatch. We can find the central frequencies of the down-converted photons by solving for $\Delta k = 0$.

If bulk crystals were our only option, this is where we would hit a roadblock, as we have no control over which down-converted frequencies are in the collinear spatial mode. To solve this problem, a technique called Quasi-Phase Matching (QPM) is commonly used. The crystals used for QPM are periodically poled during their creation process with a spatial period Λ in the optical axis for down-conversion. This introduces an extra term in the phase-matching equation:

$$\Delta k = k_p - k_s - k_i \pm \frac{2\pi}{\Lambda} \tag{2.39}$$

When we combine this with the dispersion relation $k = \frac{n(\omega)\omega}{c}$ and energy conservation, we can solve for the down-converted frequencies of the signal and idler photons for any Λ we choose. This technique gives us a lot of freedom in choosing a large range of down-converted frequencies. For even more fine-tuning, the temperature of the crystals can be changed, as the refractive indices are dependent on temperature [16, 17].

2.3.1. Types of SPDC

As seen in the previous chapter, control over the different refractive indices of each of the photons is important. Also, having some kind of nonlinearity is needed in down-conversion processes. That is why birefringent nonlinear crystals are a natural solution for these kinds of problems. Here we will quickly go over the two most important types for this project: type-0 and type-II. These types are characterized by the polarization of each photon. A simple schematic can be seen in figure 2.2. For both types in ppKTP, we propagate our photons along the x-axis. For type-0, the photons are all polarized in the z-direction of the crystal. For type-II, the pump and signal are polarized in the y-axis and the idler is in the z-axis.

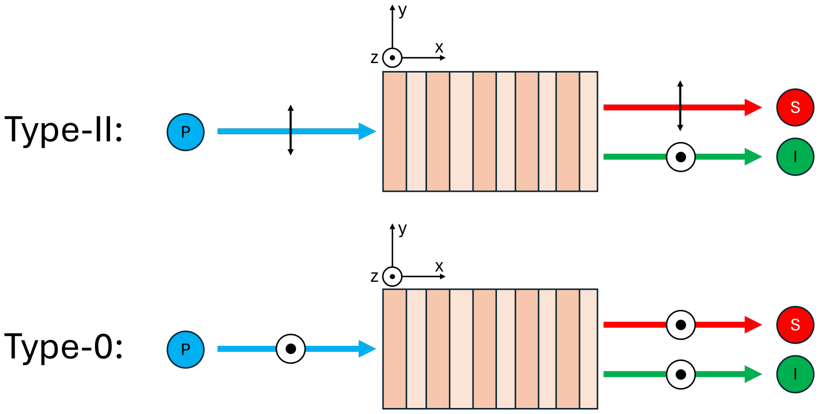

Figure 2.2: Illustration of the crystal orientation and pump, signal and idler polarization in the type-II and type-0 SPDC in ppKTP.

Different kinds of processes also have different strengths. Generally, the strength of the down-conversion is given by the effective nonlinear coefficient d_{eff}, which is different for different down-conversion processes. The strengths of the described processes are, for type-II, $d_{yyz} = 3.9$pm/V and, for type-0, $d_{zzz} = 15.4$pm/V [18].

For ppKTP, the refractive model derived by Kato et al. [16] is commonly used. In our case, our chosen pump wavelength of 405 nm is outside of the approximation range given by Kato, which is 430 nm up to 1530 nm. As will be shown in the rest of this chapter, the down-conversion process is mostly determined by the down-converted refractive properties, meaning the impact of the error in the refractive properties of the pump is negligible for us. One exception is any exact calculation we will be doing for the poling period needed, as can be seen in the phase-matching equation 2.39.

2.3.2. Collinear Spectrotemporal properties

There is one more kind of speed we need to account for whenever our photons are traveling through a bulk medium. This is the group velocity, which can be interpreted as the speed at which a photon traverses a material when considering its arrival time. We will be elaborating on this concept in the chapter Temporal Characteristics. In this chapter, we will first discuss group velocity, and afterwards we will derive how we can find the down-converted photon spectrum and arrival time information from this quantity.

The difference in group velocity between the signal and idler, or in other words the Group Velocity Mismatch (GVM) u_{si}, is our parameter of interest. We will elaborate more on this later, but know it has an influence on the down-conversion efficiency and spectrotemporal properties, which influence the experimental visibility α. In this thesis, we work with the definition given by Trojek [12]:

$$u_{si} = \frac{1}{v_{g,s}} - \frac{1}{v_{g,i}} \tag{2.40}$$

where $v_{g,s/i}$ is the group velocity of the s/i photon, calculated from the refractive index [16] using:

$$\frac{1}{v_m} = \frac{1}{c}\left[n(\lambda_m) - \lambda_m \frac{\mathrm{d}n(\lambda_m)}{\mathrm{d}\lambda_m}\right] = \frac{n_{g,m}(\lambda_m)}{c} \tag{2.41}$$

In Figure 2.3 **a)**, you can see the group velocity for both axes used in our down-conversion process of a KTP crystal. Peculiarly, you can see that there are frequencies for which these are matched. To find these, we take the wavelengths for which the group velocity is equal. We then can calculate the appropriate pump wavelength and plot this, as can be seen in Figure 2.3 **b)**. Here we can find pump wavelengths for different separations. This is a powerful concept, as this results in zero timing jitter.

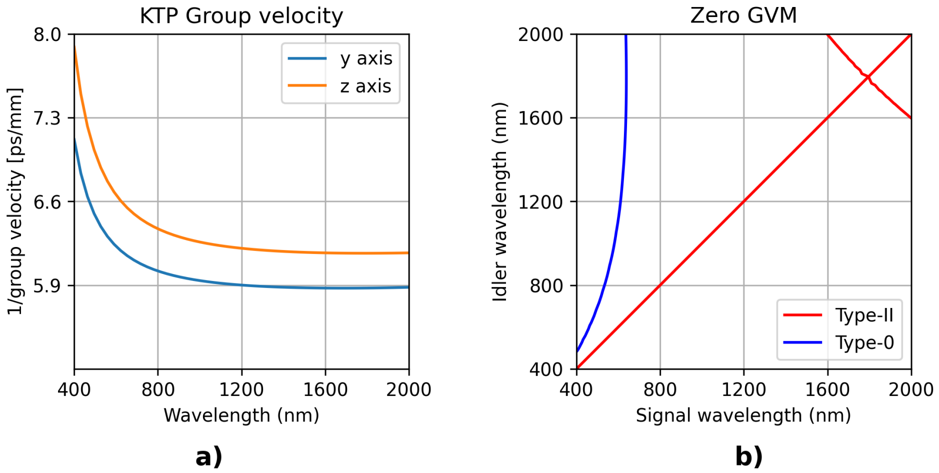

Figure 2.3: The reciprocal of the group velocity in ppKTP along the axes of interest is shown in **a)**. **b)** shows the wavelength combinations where the group velocity mismatch u_{si} is zero for both type-II and type-0 SPDC.

Another important quantity is the total group velocity dispersion D_{si}, once again defined by Trojek [12] as:

$$D_{si} = \mathcal{D}_s + \mathcal{D}_i \tag{2.42}$$

where $\mathcal{D}_j$ is the group velocity dispersion of the signal/idler/pump photon given by:

$$\mathcal{D}_j = \frac{\lambda_j^3}{2\pi c^2}\frac{\mathrm{d}^2 n(\lambda_j)}{\mathrm{d}\lambda_j^2}. \tag{2.43}$$

In general, for small enough linewidths, which we mostly assume, this dispersion can be neglected. However, in some situations we do need this quantity. We will discuss an example of this in the next chapter.
For phase matching, we are interested in the refractive behavior near each central frequency ω_j^0, where $\nu_j = \omega_j - \omega_j^0$. This is why we will make the following assumption:

$$\Delta k \approx u_{si}\nu_s + \frac{D_{si}}{2}\nu_s^2 \tag{2.44}$$

2.3.3. Down-converted spectrum

Here we discuss the basics of the spectrotemporal properties. We start off by discussing the Joint Spectral Amplitude, JSA(ω_s, ω_i), which is determined by the spectrum of the pump in combination with the spectrum resulting from the phase matching. This results in a pump function $\alpha(\omega_s, \omega_i) = \delta(\omega_p - \omega_s - \omega_i)$. We assume our CW pump to have a negligible spectral width, which is achievable as MHz linewidth lasers are available [19].

As stated before, we consider the spectrum and linewidth of the down-converted photons as described by Trojek [20]. For continuous wave pumping and collimated illumination, this results in the spectrum given as:

$$S_s^{(\text{cw})}(\nu_s) \propto L^2\,\text{sinc}^2\left[\frac{L}{2}\left(u_{si}\nu_s + \frac{D_{si}}{2}\nu_s^2\right)\right] \tag{2.45}$$

Where L is the length of the crystal and ν_s is the angular frequency distance from the central frequency of the signal. The spectrum of the idler can be found similarly by substituting the subscripts ”s” and ”i”. For type-II down-conversion in (near-)degenerate ppKTP, $u_{si} \approx 10^{-10}$s/m and $D_{si} \approx 10^{-25}$s^2/m^2. u_{si} is large due to the signal and idler having different polarizations in type-II down-conversion, in combination with the birefringence of the crystal. In Figure 2.4, we compare these degenerate situations. The key takeaway for the spectrum is that type-0 has a much wider spectrum for (near-)degenerate conditions.

For near-degenerate HOM interferometry, type-II has generally been the configuration of choice [6, 21], as the separation should be larger than the single-photon spectrum; otherwise, the beating will not occur.

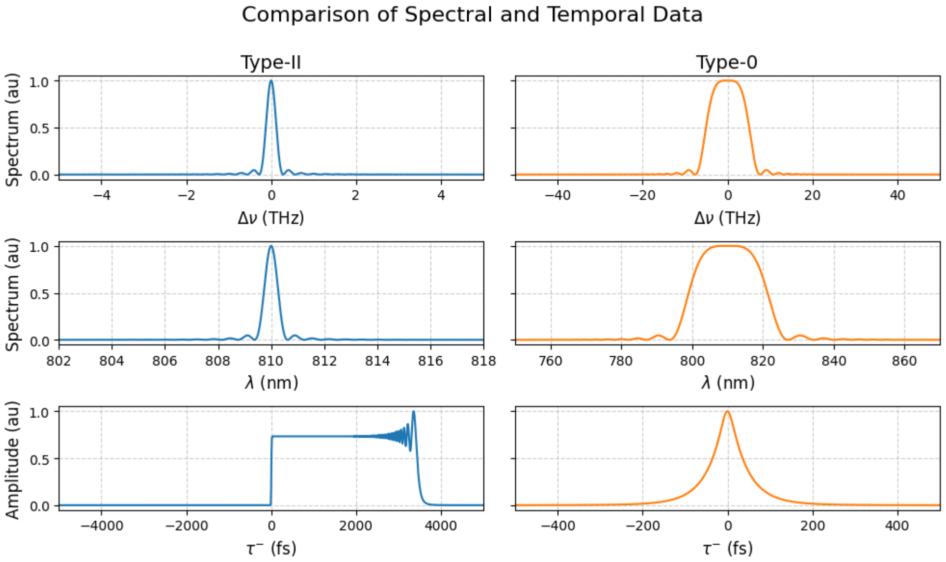

Figure 2.4: Comparison of spectrotemporal characteristics of type-II and type-0 degenerate SPDC CW-pumped with a pump wavelength of 405 nm in ppKTP of 1 cm. The first and second rows show the spectrum of the down-converted photons with respect to the difference in frequency and the wavelength. The last row shows the probability of relative arrival time $\tau^- = \tau_s - \tau_i$.

It has been verified that the ringing in the bottom left of Figure 2.4 is not Gibbs ringing, which is a byproduct of improperly sampled Fourier transforms. It seems to be an effect of the non-negligible D_{si}. Neglecting this term would result in a cleaner square amplitude, which is in line with what we would expect.

Do note that this spectrum is given as a sinc function. The approximation for HOM interference is mostly calculated for normally distributed spectra, as this simplifies the result. A Gaussian filter can be used to suppress the nonvanishing tails of the sinc function. This method will be further discussed in Section 3.5.1.

2.3.4. Temporal characteristics

We are also interested in the phase information of the spectrum when calculating the overlap between two down-conversion processes. This can be more easily understood when working in the time domain. The temporal amplitude can

$\tau_- = \frac{\tau_s - \tau_i}{2}$ is once again the relative arrival time between the signal and idler photon. From Trojek [12] we find the following for the temporal amplitude $\mathcal{A}_{\tau_-}(\tau_-)$ of the down-converted photons for CW-pumped light

$$\mathcal{A}_\tau(\tau_-) \propto e^{\frac{i}{2}\omega_p \tau_-} \int_{-\infty}^{\infty} d\nu_s e^{-i\nu_s \tau_-} \times \mathcal{T}_s(\nu_s)\mathcal{T}_i(-\nu_s)\mathcal{A}_\nu(\nu_s) \tag{2.46}$$

Here ω_p is the angular frequency of the pump photon. $\mathcal{T}_{s/i}$ represents spectral effects of other components in our setup. We will discuss this in a moment. One last remark, is that this is a Fourier transformation.

Here we can place an example of the timings of two different kinds of cases. We can look at this distribution for type-II and type-0 near-degenerate conditions, which can be seen in Figure 2.4. In type-II, the two photons have widely different group velocities due to the different polarizations and birefringence of the crystal, meaning this term dominates. For near-degenerate type-0 situations, there is no group velocity mismatch, as both photons experience identical refractive index profiles. In this situation. Here D_{si} determines the spectral behavior. An example of this can be seen in Figure 2.4

One quantity in this equation not yet named is the transfer function of our measurement setup on the signal/idler photon, $\mathcal{T}_{s/i}$. Here we can add the effects of other components like bulk materials or filters on the temporal characteristic of the down-converted photons [22]. The total transfer function for a bulk crystal can be easily calculated from the single-photon transfer function:

$$\begin{aligned} \text{Filter signal: } & \mathcal{T}_s(\nu_s) = \sqrt{F_s(\nu_s)} \\ \text{Filter idler: } & \mathcal{T}_i(\nu_i) = \mathcal{T}_i(-\nu_s) = \sqrt{F_i(-\nu_s)} \\ \text{Bulk crystal (signal): } & \mathcal{T}_s(\nu_s) = e^{iL\nu_s[1/v_{g,s}+\mathcal{D}_s\nu_s/2]} \\ \text{Bulk crystal (bi-photon): } & \mathcal{T}(\nu_s) = e^{iL\nu_s[u_{si}+D_{si}\nu_s/2]} \end{aligned} \tag{2.47}$$

Notice here, we assume filters only have influence on the amplitude, and propagating through bulk crystal only results in a additional phase. This also has some implication for the arrival times of the photons. in Figure 2.5 the temporal effects of u_{si} and D_{si} are qualitatively illustrated.

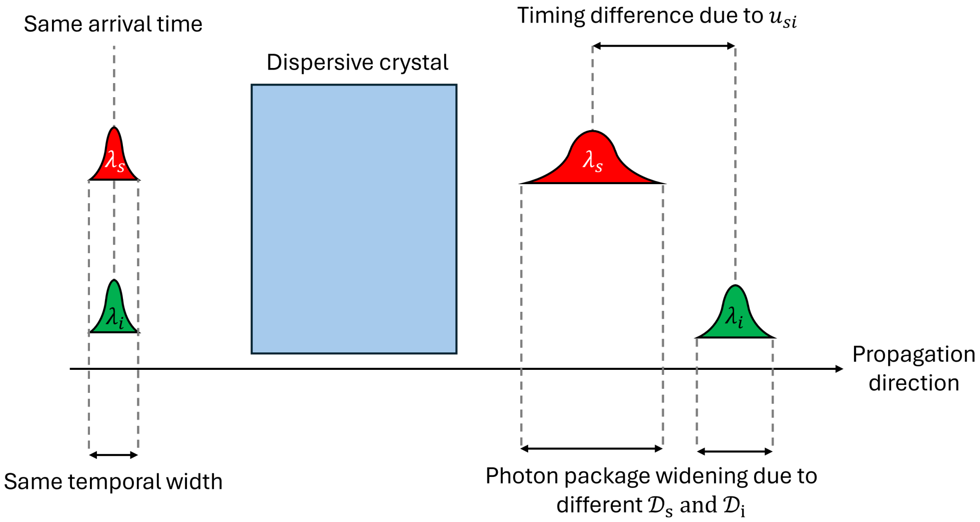

Figure 2.5: Qualitative example of dispersive quantities on the biphoton arrival times.

2.3.5. Beam focusing and SPDC

Up to this point, we have only discussed how light interacts with the crystal as a plane wave. While we can illuminate light in this way, conventionally some level of focusing is used, as it increases the down-conversion rate, albeit at the cost of heralding efficiency [23]. The effects of beam focusing have been rigorously researched by Bennink [23]. Here, he derived equations from which we can optimize the focusing criteria for maximum brightness, heralding ratios, and single-photon spectral purity for unfiltered down-converted photons.

Our goal is to translate the results found in this paper to their effect on our simulation parameters: brightness R_{si}, photon loss $\gamma_{s/i}$, and down-converted linewidth σ.

We will not go over the full derivation. Instead, we will extract some important equations and briefly explain how we interpret them. We make two changes. First, we make the approximation that our laser is monochromatic, meaning $\alpha(\omega) = \delta(\omega - \omega_p)$. Secondly, this paper discusses a number of pump photons $N_p = \frac{E_p}{\hbar\omega_p}$, where E_p is the total energy and $\hbar\omega_p$ is the single-photon energy. As we use continuous-wave lasers, we will instead substitute this number with our laser power, meaning we change the units of the calculated brightness from dimensionality [#photons] to [#photons/s]. For the rest of this chapter, every subscript j can be substituted with s, i, p, which relates to properties for the signal, idler, or pump photon.

Bennink assumes all beams to be Gaussian [23]. The illumination/collection crystal focusing parameter ξ_j is defined as:

$$\xi_j \equiv \frac{L}{k_j w_j^2} \tag{2.48}$$

where w_j is the beam waist of the emitted or collected light and k_j is the refractive index experienced by the photons. Relating ξ_j to the Rayleigh length $z_R = \frac{1}{2} k_j w_j^2$ gives a clear interpretation:

$$\xi_j = \frac{L}{2 z_{R,j}} \tag{2.49}$$

When $\xi_j = 1$, the crystal length is equivalent to the Rayleigh length. Smaller values represent more collinear conditions, while higher values indicate strong focusing.

Restrictions on the focusing parameters

We first investigate the assumptions made by Bennink; after that, we discuss some other restrictions important for our specific use case.

General assumptions

The exact meaning of the assumptions made by Bennink is too convoluted to fully discuss in this thesis. In a simplified sense, the assumptions are as follows:

- $\Delta k \approx -mK$
- $C \ll 1$
- JSI$(\omega_s, \omega_i) = \alpha(\omega_p)\Phi(\omega_s, \omega_i)$
  This holds whenever the bandwidth of all photons is small compared to their wavelength.
- $\delta k_j \approx \frac{1}{v_{g,j}} \delta\omega_j$
  This holds whenever the behavior of Δk can be approximated using the group velocities; in other words, we can neglect the effects of group velocity dispersion.

More details on unnamed quantities in these equations can be found in the paper of Bennink [23]. Do note that we comply with all of these whenever we have sufficiently long crystals, and whenever we are not operating too close to the zero GVM regime. Some of these conditions are not met for large ξ_j. In Figure 2.6, we go over the conditions and show the maximum allowed focusing for different signal and idler wavelength combinations for type-0 and type-II SPDC in a crystal of 1 cm long.

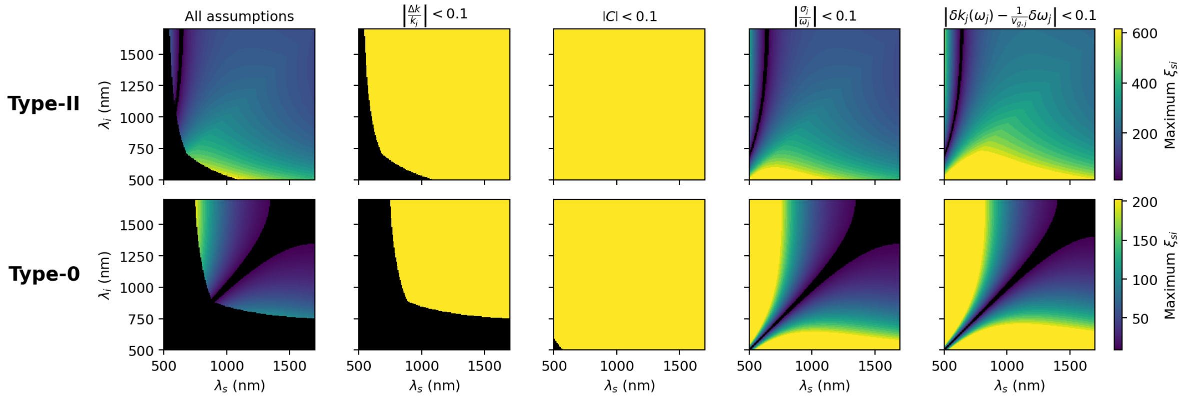

Figure 2.6: Allowed focusing conditions for type-II and type-0 SPDC for different combinations of signal and idler wavelength. The maximum allowed focusing is given by the color bar on the right. The second column shows $\left|\frac{\Delta k}{k_j}\right| < 0.1$, the third $|C| < 0.1$, the fourth $\left|\frac{\sigma_j}{\omega_j}\right| < 0.1$ and finally the fifth $\left|\delta k_j(\omega_j) - \frac{1}{v_{g,j}}\delta\omega_j\right| < 0.1$.

Choosing focusing focal length

The focal lengths of the lenses needed for illumination f_p and collection f_c are determined by two parameters: the divergence angle of the Gaussian beams outside of the crystal $\theta_{vac,j}$, and the collinear beam diameter before illumination or after collection. The collection side does have some challenges. Our goal is to have identical outgoing cones of light for both the signal and idler photons. In the quantum communication sector, the signal and idler are often spatially separated, allowing for collection using separate collection optics [24]. This allows for the efficient collection of both signal and idler photons, as they generally have different emission cones, which we will discuss later in this chapter.

We have the restriction of only using a single lens, as we want both down-converted photons in a single spatial mode. We assume our outgoing cones for the signal and idler are identical if $\theta_{vac,s} = \theta_{vac,i}$. Using Snell's law and the refractive indices experienced by the signal and idler, we find the dependency between ξ_s and ξ_i to be:

$$\xi_s = \frac{k_s}{k_i}\xi_i \tag{2.50}$$

There is one problem with this approach, which is that we do not yet take into account that the difference in refractive indices results in an effective difference in focal point distance dz_{si}. The value dz_{si} can be calculated in the strong-focusing case ($\xi_j > 1$) using ray optics.

$$dz_{si} = \frac{L}{2}\left(\frac{1}{n_s} - \frac{1}{n_i}\right) \tag{2.51}$$

This effect could possibly be solved with a custom achromat, designed for these specific wavelength-dependent focal lengths. In this thesis, we limit ourselves to the situation where this is not needed. For this to be the case, we assume that the focal spot difference between the signal and idler should be smaller than the Rayleigh length for both. This results in the following restriction:

$$\xi_j < \left(\frac{1}{n_s} - \frac{1}{n_i}\right)^{-1} \tag{2.52}$$

where in this case j represents the signal or idler focusing parameter.

Crystal aperture

Another limiting factor on the maximum allowed focusing is the aperture of our down-converting crystal. As stated earlier, beam clipping can have a strong effect on experimental visibility. In the strong-focusing case, ξ_j is then limited by the divergence angle inside the crystal θ_j together with the crystal length.

This also puts a limit on the minimum allowed ξ_j in the weak-focusing regime, as the beam waist gets larger as ξ_j decreases.

In this thesis, we will take both these limits into account. Standard apertures for ppKTP samples are around 1–2 mm. However, some are available at 4x4 mm in case stronger focusing is required.

Parameters for our simulation

From here on, we discuss how we determine our parameters exactly based on the paper by Bennink.

Brightness R_{si}

Bennink defines a pair collection probability P_{si}. This is, however, not a true probability distribution; rather, it also takes into account the number of pump photons N_p. Making our discussed approximations, we can convert this to a calculation of our estimated down-converted photon rate R_{si} by interchanging $N_p \to \frac{I_p}{\hbar\omega_p}$.

R_{si} is then given by equation 2.53. There are two things we can infer from this equation. Firstly, the down-conversion rate is linearly dependent on the pump intensity instead of quadratically. Secondly, the rate is inversely proportional to the group velocity mismatch u_{si}.

$$R_{si} \approx \frac{64\pi^3 \varepsilon n_s n_i}{\varepsilon_0 \omega_p n_p |u_{si}|} \left(\frac{\chi^{(2)}_{\text{eff}}}{\lambda_s \lambda_i} \right)^2 \frac{\arctan(\xi)}{A_+ B_+} I_p. \tag{2.53}$$

One last interesting result can be found when we look at the effect of the detuning Δ. Here we only look at the quantities directly related to Δ, which are λ_s and λ_i. Assuming that the refractive properties are largely independent of Δ, we find:

$$R_{si}(\Delta) \propto \left(1 - \left(\frac{\Delta}{\omega_p} \right)^2 \right)^2 \tag{2.54}$$

This result is rather interesting, as it shows that the brightness is limited by large detuning.

On the experimental side of things, there is also a maximum intensity before the crystal starts breaking down. This is called gray-tracking. For a ppKTP SHG source, a limit of 360 mW with a waist size of 42 μm has been found. This is not the same process as SPDC; however, it is stated that the damage is mostly due to the 405 nm intensity [25].

Down-converted linewidth for focused SPDC

As shown by Bennink, the shape of the spectrum depends on the focusing criteria. Previously, when calculating a spectrum, we used collinear illumination ($\xi_j \ll 1$), resulting in the spectrum acquiring the shape of a sinc function. We can now use this as a rough estimation for any focusing condition. We will not focus on the shape of the spectra in this thesis, and instead use the approximated down-converted linewidth given by:

$$\Delta\omega_s = \Delta\omega_i \sim \frac{2\pi}{|u_{si}|} \max\left(\frac{1}{L}, \frac{1}{10b} \right) \tag{2.55}$$

where $b = L/\xi$, and ξ can be seen as an overall focusing parameter defined as:

$$\xi = \frac{B_+}{A_+} \frac{\xi_s \xi_i}{\xi_p} \tag{2.56}$$

The terms A_+ and B_+ are outside the scope of this explanation. More information on these parameters can be found in the derivation by Bennink [23].

Photon loss $\gamma_{s/i}$

In this section, we will discuss how we can translate the quantities derived by Bennink to the photon losses γ_s and γ_i in our HOMI model. In this thesis, the argument is made that we can find the photon losses from the single-sided heralding ratios η_s and η_i given by Bennink, resulting in:

$$\begin{aligned} \gamma_s &= 1 - \eta_i \\ \gamma_i &= 1 - \eta_s \end{aligned} \tag{2.57}$$

The argument made in this thesis is based on Bayesian probability and can be found in Appendix D. In general, weaker focusing tends to result in higher heralding ratios, meaning lower losses.

Trade-off between tight and loose focusing

Now that we have defined the quantities we are interested in, we can finally discuss the trade-offs for our case. To start off, focusing is a trade-off between heralding ratios and brightness. Stronger focusing ($\xi \gg 1$) results in a higher brightness R_{si} at the cost of higher photon losses $\gamma_{s/i}$. This balancing act, together with the restrictions named, will determine the optimal operational conditions.

3

Experimental design

In this chapter, we present the proposed experimental setup. We begin by outlining the design parameters and design philosophy underlying our experimental choices, which serves as a reference framework for evaluating the different design options. The focus of this chapter lies primarily on the optical design of the experiment and the corresponding implementation choices.

The setup can be split into three distinct parts:

- Biphoton source
  Generation of a photon-pair state from the pump beam
- Interferometer
  Interaction of the photons with the sample
- Detection system
  Measurement of the output state after the HOM beam splitter

The interferometer is discussed first, as it determines the required properties of the biphoton source. The biphoton source is then described in light of these requirements. Finally, the detection system is introduced.

3.1. Design parameters

Beam diameter choice

A beam diameter of 1 mm is chosen for both the pump and down converted beams. Since the experiment is not aimed at imaging the sample but rather at measuring a discrete effect, a tightly focused beam at the sample is not required.

Sample reflectance

We explicitly use the same material for the reference as the sample beam in both situations, as a different reflectance of a reference beam would introduce which path information. One thing we need to consider is the sample reflectivity. We assume the sample is made from silicon. From its refractive index[26] we can expect a reflectivity of around R=0.35 for our wavelengths of interest. Coincidentally, carbon layers have a similar reflectivity [27], which implies that any measurement that works for a silicon sample also works for carbon.

One assumption we will be making is that the sample does not exhibit birefringent effects. That is, the polarization of the light does not change after reflection.

Necessary positioner precision

One parameter we need to decide on is the precision of our delay line. From the measurement outcomes defined in equation 2.9 we learn that we need at least proper sampling of $\cos(\Delta\tau)$. Assuming that Δ will typically be of the order 10^{14}rad/s to 10^{15}rad/s, this results in an spatial delay oscillation period of 1-10μm. Proper sampling needs to be determined for specific operational wavelengths.

Sample interaction

Early on in the designing process it was found that there are 2 distinct options for measuring the step size on a sample. In Figure 3.1 we illustrate these 2 options. In option 1 (Figure 3.1a) the 2 beams are parallel to each other with a shift so that by moving the sample, we have either the 2 beams at the same height or the two beams at a different heights. In option 2 (3.1b)The two beams can be spatially separated and our beam is always at a fixed position on the reference.

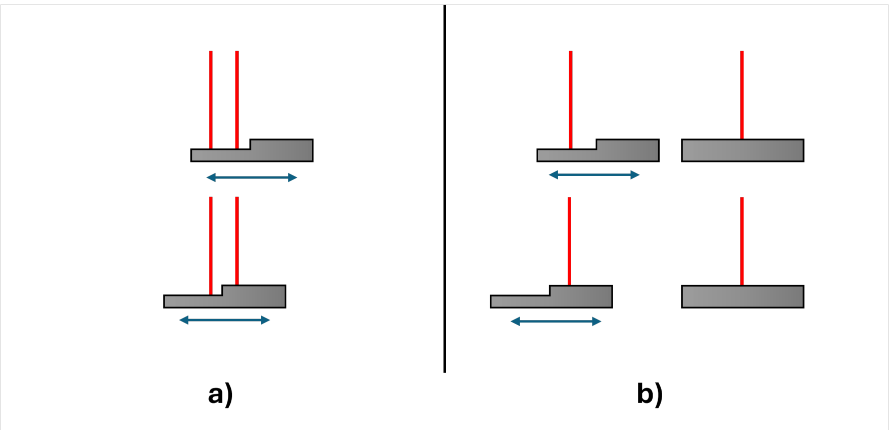

Figure 3.1: Two possible sample interactions: Single sample (a) and sample and a separate reference (b).

The advantage of single sample is that it is more compact, introduces less components meaning less risk for alignment issues and it is common path. One problem is however that this compactness also restricts the geometric design even further. Adopting a reference sample reliefs the geometric design as we no longer need the extra constraint of moving the beams close to each other at the sample. This also allows for future scanning HOMI for full 3D reconstruction of a surface.

3.2. Design philosophy

During the design process, several principles were adopted to minimize the introduction of distinguishability between the photon pairs. As discussed previously, there are many possible sources of distinguishability. In practice, distinguishability can be introduced by unbalanced losses, unequal filtering, or different arrival times at the detectors, among other effects. To reduce such effects, the following principles were applied:

- Maintain path symmetry
- Minimize the number of optical components
- Avoid beam crossings
- Avoid dispersive components
- Ease of alignment and workability

Maintain path symmetry

Path symmetry ensures that both photons experience identical optical conditions. If both photons pass through components with identical losses and filtering characteristics, no which-path information can be inferred. For example, if one interference path contains additional loss, the creation process may become distinguishable.

In this work, components are considered identical only if both the incidence angle and polarization conditions are the same. For example, identical mirrors reflecting light at different angles of incidence are not considered identical, as this may slightly affect their reflectivity. Although this strict requirement may not always be necessary, consistently applying it reduces the number of uncontrolled experimental variables.

Minimizing optical components

Each additional optical component introduces a potential modification of the photon state. Loss, dispersion, or polarization changes may increase distinguishability. Reducing the number of components lowers the risk of unintended losses or state modifications.

Avoiding beam crossings

In theory, beam crossings should not introduce problems, as there is no direct photon–photon interaction. Unfortunately, in a realistic laboratory environment, dust or scattering in the air can reflect light from one path into the other. This may introduce crosstalk and introduce distinguishability.

Avoiding dispersive components

In our experiments, the signal and idler photons have different wavelengths and therefore experience different refractive indices due to material dispersion. This makes some optical designs used for the more common (near)degenerate HOMI, where signal and idler experience the same refractive effects, unpractical for us. Although achromatic optics can partially mitigate chromatic effects, group velocity mismatch and group velocity dispersion within dispersive elements may still introduce temporal distinguishability and spatial walk-off. Dispersive components like bulk crystals are therefore avoided where possible.

Ease of alignment and workability

The experiment should be as simple in alignment as possible. Unneeded long optical paths should be avoided, for example, as aligning the mirrors becomes harder.

Workability is also important. If possible, the experiment should be compact. For example, if a setup needs a long optical path for both the sample and the reference, then both optical paths should be parallel to save space.

Symmetry and beam crossings

The design rules we imposed on the interferometer limit the geometric freedom of the optical layout. We found that it is not possible to maintain complete geometric symmetry in both interferometer arms without introducing beam crossings or violating one of our design rules. Using different optical heights partially alleviates this issue but does not fully resolve it.

We could consider breaking one of our rules, however there is one symmetry that can be relaxed without introducing distinguishability. This symmetry is the order of identical components within each arm. If both arms contain the same reflective optical elements, the sequence in which identical mirrors appear does not provide which-path information. This means we are no longer limited by geometric symmetric paths.

Common path

Two optical paths are in common path whenever they are spatially in the same path, and are distinct in another property. Our separating property will be the photon polarization to distinguish entangled photons. Common path optics is a technique which will be helpful to us, as both beam optical paths experience in general the same influences whenever they are in the spatial path. This would introduce no distinguishability. The only caveat is that polarization based effects like birefringence introduce possible distinguishability.

3.3. Interferometer Design

Designing the interferometer proved to be challenging, as satisfying all previously defined design constraints simultaneously became a hard puzzle to solve. The primary challenge stems from the conventional HOM architecture, which requires two interferometer arms. Designing these 2 arms while respecting our design philosophy significantly constrained the layout.

A similar HOM interference configuration can be realized by illuminating only one input port and replacing the beam splitter with a PBS. In this case, the two input modes are no longer spatially separated at the 2 inputs of the beam splitter, but instead distinguished by polarization. The relevant polarization states are the (anti)diagonal states, A and D. We show in Appendix E that the A/D polarization-based PBS configuration is mathematically equivalent to the conventional beam-splitter configuration with two spatial input modes. A comparison of the 2 photon interferences can be seen in figure 3.2

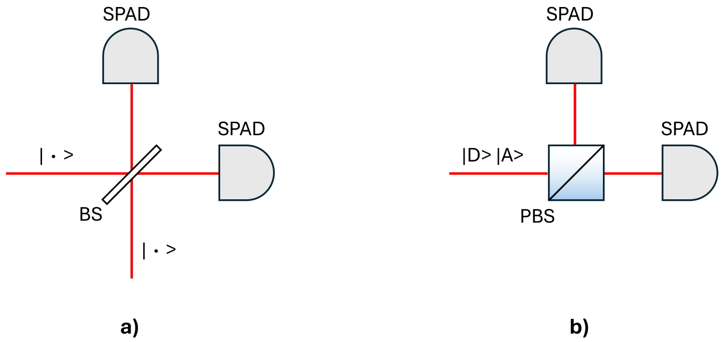

Figure 3.2: Comparison of **a)** the conventional HOMI where both input states have identical polarization and **b)** mathematically equivalent HOMI on a PBS where both states enter using the same input, but they are (anti)diagonally polarized

Such polarization-based biphoton interferometry has been demonstrated by Kaneda [21].

This equivalence allows us to work within a single spatial mode while retaining the same interference behavior. As a result, the interferometer can be designed in a way that better preserves path symmetry and avoids unnecessary geometric complexity, in line with the principles outlined in our design philosophy.

In the final interferometer design, we choose a design similar to that demonstrated by Kaneda [21]. We use a single spatial input PBS-based HOMI as the interference part of the setup in combination with a PBS for separating the polarization modes to 2 distinct spatial modes. A scheme of the design is shown in figure 3.3**a)**.

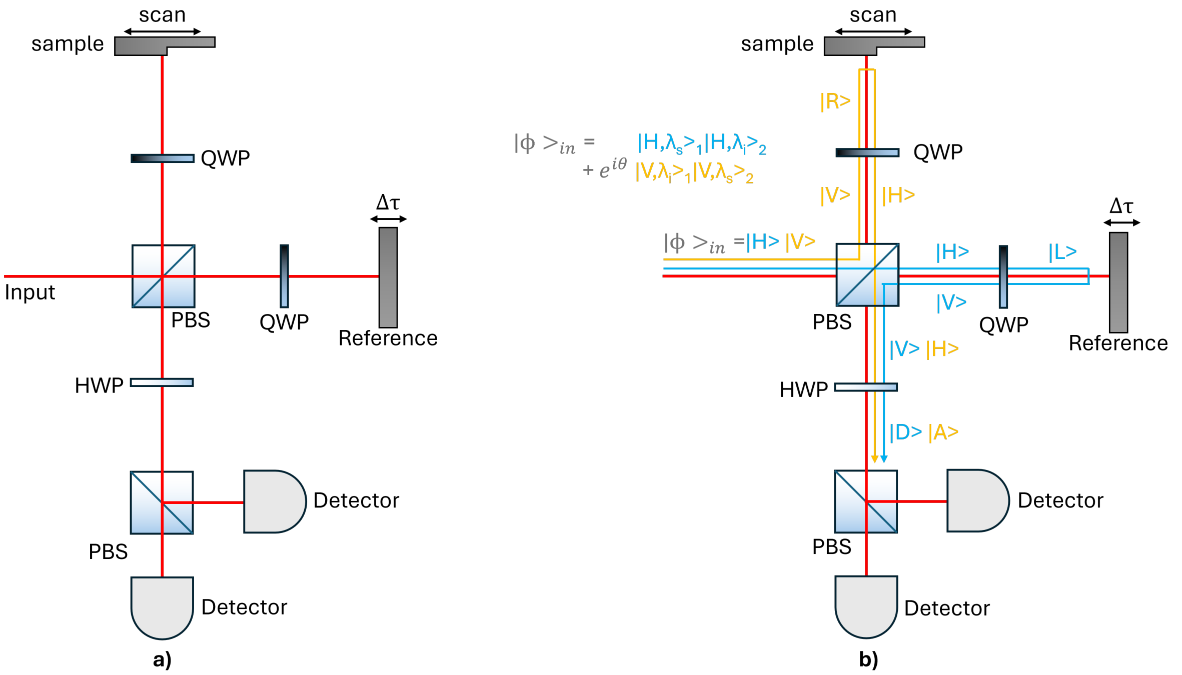

Figure 3.3: **a)** optical scheme of interferometer. **b)** explanation of the polarization states of the superposition. H, V, L, R are the horizontal, vertical, right hand circular and left hand circular rotations respectively

Since the spatial modes are shared, keeping track of the superposition is less intuitive than in interferometers with separate spatial paths. The polarization states are therefore shown explicitly in figure 3.3**b)**.

From the biphoton source we assume that the superposition is based on the H and V polarization modes. The two polarization modes are first separated using a polarizing beam splitter, defining the sample and reference arms with V and H polarization, respectively. In both arms, the light passes through a quarter-wave plate (QWP), converting the polarization to circular R and L polarization. Upon reflection from the sample and a second pass through the QWP, the total transformation is equivalent to a half-wave plate (HWP), provided that the sample does not modify the polarization. As a result, all photons switch from V to H while traversing through the sample and reference branch and vice versa. The outgoing light of both paths than travel to the yet used output of the PBS, recombining in a single spatial mode.

Finally, a HWP set at 22.5° rotates the polarization basis from H/V to D/A, enabling single-input HOM interference at the PBS. we discussed at the beginning of this section.

One advantage of this configuration is that both parts of the superposition propagate in the same spatial mode. In other words, most of the setup can be kept in a common path. As discussed in the previous chapter, this helps ensure that both components experience the same aberrations, thereby minimizing distinguishability.

There is one important distinction from the experiment of Kaneda. Instead of using mirrors in both arms, we use the sample and a reference made of the same material. Both are mounted on piezo stages for precise position control. As discussed earlier, the reference is made of the same material as the sample with the goal to minimize which path information.

A temporal delay can be introduced by translating the reference along the optical axis. This removes the need for a separate delay station, simplifying the design. The sample can be moved laterally to include or exclude the step structure. In principle, this also enables scanning across the sample, allowing for other types of samples in future works.

Alternative interferometer designs

During the design process of the interferometer, other designs have been considered. These designs can be found in appendix F and might be useful for future work or inspiration. Some additional design parameters needed for the previous designs can also be found at the beginning of the appendix.

We started of with the more conventional HOM interference utilizing the 2 spatial inputs of balanced beam splitter. These designs can be found in Appendix F.1 until F.4. We made different attempts to solve the geometric difficulties; however, compared to the suggested interferometer in this thesis, those designs proved to be too complex. More disadvantages of these setups were the nonzero angle of incidence needed at the sample and the need for multiple beam heights.

In Appendix F.5 one final design can be found based on a completely different approach. This design is inspired by the beam displacer based photon sources [28, 24]. This design is geometrically simple and would be a contender for the current design, however, there is one flaw we need to discuss. The displacement of beam displacers is generally wavelength dependent. For (near)degenerate HOMI this would introduce no problems, however, we design for nondegenerate HOMI. This design is still feasible by engineering effective achromatic beam displacers made of multiple birefringent materials [29].

3.4. Biphoton Sources

In this chapter, we discuss the biphoton source needed for our previously discussed interferometer. Our starting point was the cross crystal biphoton source, as this configuration was also used in our starting reference paper [6]. We will shortly describe how it works and present some (dis)advantages of the setup. Next, we will discuss some other commonly used photon source options. At the end of the chapter, we introduce our own scheme, which is more in line with our design philosophy.

Cross crystal scheme

The cross crystal scheme gets its name from the fact that two SPDC crystals in are aligned series rotated by 90 degrees with respect to each other. Now we will illuminate these crystals using a diagonally polarized D pump beam. As discussed in the theory, these crystals can only perform SPDC when the pump photon is aligned with the right axis of the crystal. The H and V basis for the 2 crystals respectively. Assuming identical SPDC processes for the 2 crystals, we now get completely identical photons from both processes, except for the polarization of the outgoing signal and idler photon. These are flipped between H and V, as the 2 creation processes are also rotated by 90 degrees.

A scheme of the cross crystal configuration can be seen in figure 3.4**a)**. A more elaborate bookkeeping of the different photons can be seen in figure 3.4**b)**. The downconverted photons are labeled as $|H/V, \lambda_{s/i}\rangle_{A/B}$. The inside of the ket describes the photon, and the subscript A/B describe the crystal of origin.

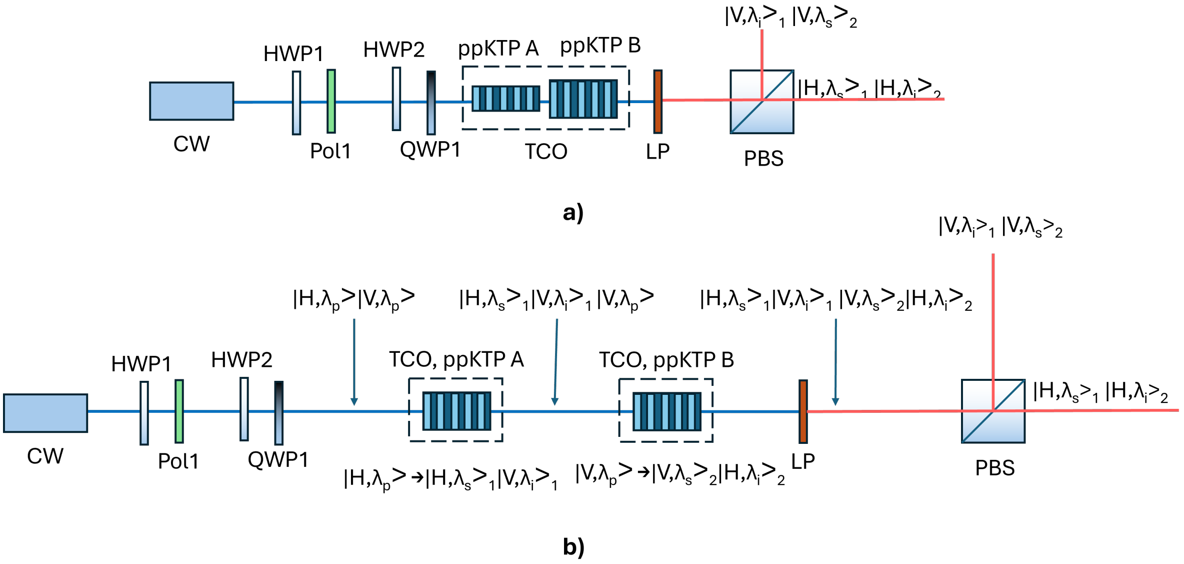

Figure 3.4: A scheme of a cross crystal configuration in **a)** standard scheme, **b)** a more complete explanation of all the photon states of **a)**

The source starts with our CW pumped laser. then HWP1 and Pol1 can be used for tuning the pump power. This method is preferred to changing the pump power of the laser, as the laser power may influence the spectral properties of the beam.

Waveplate HWP2 changes the polarization of the pump to the diagonal D basis. Additionally, HWP2 can be slightly tilted for fine tuning the relative power between the 2 down conversion processes if needed. QWP1 is used to set the phase between the 2 down conversion processes. This can be seen as delaying the vertical component of a photon with respect to its horizontal component of the pump photon.

After this, the 2 crystals ppKTP A and ppKTP B are placed in series, with their axis rotated 90 degrees with respect to each other. These crystals are placed in temperature controlled ovens (TCO) for experimental finetuning. A long pass filter (LP) is placed after the crystal for filtering out the pump beam. A final PBS can then used to spatially separate the photons if desired.

The advantage of this setup, is that alignment is almost trivial compared to other entangled photon sources. However, that comes at some major costs.

The first problem is the downconverted photons of the first crystal travel through more birefringent material compared to the photons downconverted in the second crystal. This introduces additional distinguishability, due to different group velocity dispersion and walk-off effects of the downconverted photons.

An additional problem is that illumination and collection beams are focused on the interface between the crystals. This breaks the discussed theoretical basis of Bennik, as there, it is assumed that the focal point is in the middle of the crystal. A proper derivation similar to Bennink can be done for this setup; however, this is outside the scope of this thesis.

These disadvantages become worse at larger detunings. There are a few other conventional designs; most of these are discussed in the review article on Entangled photon-pair sources of Anwar from 2021 [30]. Some of these designs are listed below:

Sagnac loop

The Sagnac loop is a promising candidate, reaching high luminosity and heralding ratios [31, 32, 10]. However, this setup is in general hard to build due to the need to align the clockwise and counterclockwise traveling light. The difficulty of alignment is considered a big enough downside to not go for this option.

Sandwich method

The sandwich method is based on the Sagnac loop [33]. At first, this looks promising. However, it has a complex custom achromatic waveplate and does not seem to be used in further research.

Beam displacer-based source

At last, we look at the beam displacer design [28, 34, 24]. This is a relatively new concept compared to the others and seems to be promising due to the simplicity of the design. Most of these sources are made for (near)degenerate wavelengths [28, 34] or use different collection optics for the signal and idler photon to account for different emission cones [24]. Unfortunately, this design does not easily work well for our case as we want to collect both wavelengths with the same collection optics.

One can engineer achromatic beam displacers by combining beam displacers of different materials at different orientations[29]. This technique can be used to make an achromatic beam displacer or one that is optimized for our 2 wavelengths of interest. Designing such a beam splitter would be outside of the scope of this thesis. That is why we decided not to follow this route as our design philosophy shifted towards using the least amount of dispersive elements. In the end, we decided to make a design of our own, using some lessons learned from the other designs.

3.4.1. Our biphoton source design

The working principle of our design closely resembles that of the beam displacer based photon source. The design we came up with closely follows our design philosophy. The discussed biphoton source design is for type-0 SPDC. A small alteration for type-II will also be discussed.

The design can be seen in figure 3.5. Similarly to the beam displacer based photon sources, we choose our optical paths of both downconvertion processes to be parallel and close to each other. This makes the setup compact and easy to use in the lab.

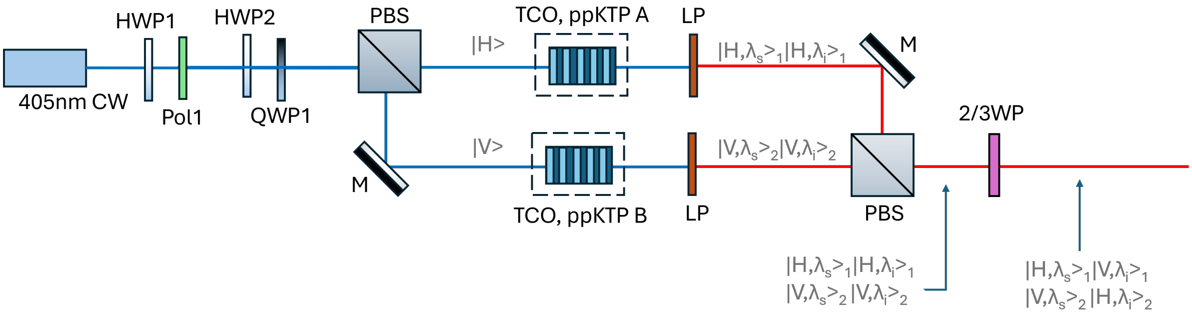

Figure 3.5: A scheme of the PBS based type-0 biphoton source.

The use of HWP1, Pol1 HWP2 and QWP1 are identical to those of the cross crystal photon source seen in figure 3.4. HWP1 and Pol1 are used to control the intensity of the pump beam. HWP2 is used to make the pump beam diagonally polarized. HWP2 can be altered to rebalance the pump intensity between the 2 downconversion processes. QWP2 is used to control the phase ϕ between the 2 creation processes.

A PBS is used to separate the horizontally and vertically polarized parts of the beams. Both beams will go to their respective downconversion crystal ppKTP A/B. The crystals are placed in a temperature controlled oven (TCO) for experimental finetuning. a LP filters out the pump photons. The downconverted photons are recombined with another PBS. At this point the states are not yet frequency entangled. To achieve this, we introduce a 2/3th waveplate. This component acts as a FWP for the signal and HWP for the idler. Placing this 2/3WP at an angle of 45 degrees changes the polarization of the idler between H/V while leaving the signal photons unchanged. This results in the frequency entangled photons that we want. Normally this state mixing is done using beam splitters. mixing the states using waveplate as proposed here is a novel approach as far as we know.

For this thesis we assume perfect 2/3WP. Such custom multi-order waveplates are in fact commercially available.

This design can be altered to allow for type-II SPDC as mentioned. One can use more 2/3WP's after the downconversion crystal, but before the mixing PBS. This is at the risk of introducing more which crystal information due to manufacturing imperfections in the 2 waveplates.

There are still 1 type of component in our scheme that can introduce distinguishability: the mirrors. The reader might have noticed we introduce an asymmetry with the setup. One reflection occurs before downconversion while the other after. This difference might introduce which crystal information, However we assume this effect to be minimal. Another difference is that downconversion A has a larger optical path as a downconverted photon while B has a larger path as a pump. The total path length however is identical. This fact in combination with the air having no chromatic aberrations, meaning no (group)velocity difference, results in no which crystal information being generated.

Geometric variations

This source is spatially highly adaptable. One can choose for the other output of PBS2 by switching the polarization of processes A and B. This makes this biphoton source easy to use in spatially restricted experiments. Other changes can be made to remove the asymmetry in what kind of photon reflects of the mirror in both paths, for example. In figure 3.6, a few alternatives are shown. Each of these has their own pro's and con's.

In **a)** a simplified scheme of the setup as discussed earlier can be seen. In **b)** and **d)** the first PBS is replaced by a Wollaston prism, which separates both polarizations at an angle. Afterwards, both beams are collected by a large lens resulting again in parallel optical paths. This Wollaston design allows for even more compact setups, however **b)** has the disadvantage of having a substantial difference in path length. Choosing a sufficiently small pump linewidth can solve this, as entanglement still occurs when the difference between the downconversion path lengths is smaller than the pump coherence length [20]. **d)** has the same kind of photons interacting at the mirrors, however the shallow angle of incidence makes the mirrors work less optimal.

We do not suggest recombining the two beams using a similar Wollaston prism used for the separation in **b)** and **d)**. Conventional Wollaston prisms have wavelength dependent angles. This would introduce to be the signal and idler are considered to have a large spectral separation.

At last we have option **c)**, which does have identical optical interactions, however takes more space due to its perpendicular optical paths. Choosing between these 4 options is up to the needs of the experimentalist working with this setup.

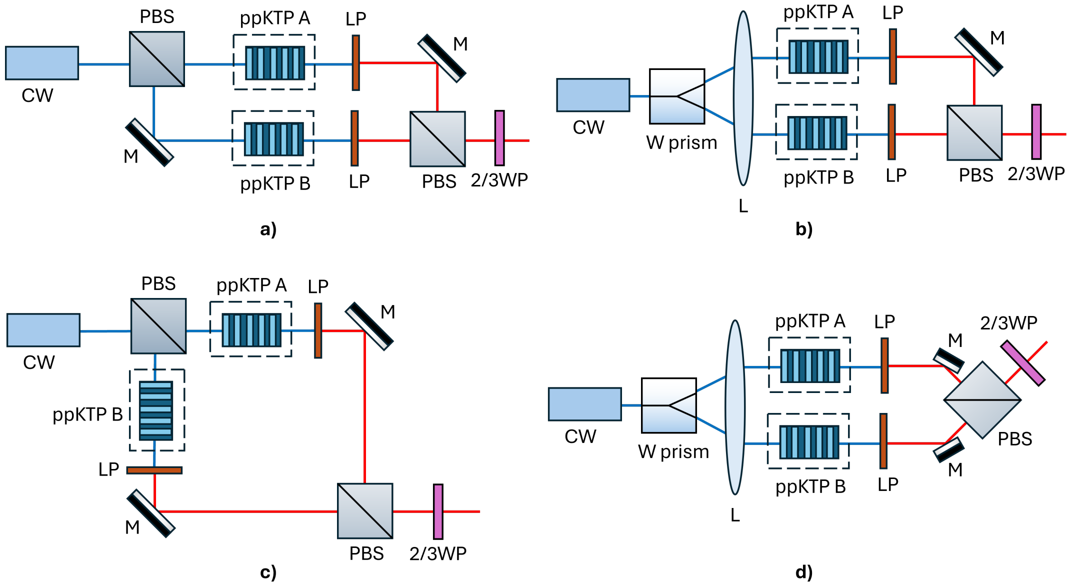

Figure 3.6: Alternative photon source orientations.

During this thesis more designs were considered. We initially focused on biphoton sources where the two outgoing photons are spatially separated, motivated by the more common two-spatial-input HOMI discussed in the interferometer section. In this configuration, a biphoton source with its entangled photons in two distinct spatial modes is the natural design goal. In the early designs we considered type-II SPDC, as the different polarizations of the signal and idler photons make them easier to manipulate. Many of these designs can also be adapted by replacing the mixing PBS with dichroic mirrors, allowing switching between type-II and type-0 implementations. The resulting designs for both type-II and type-0 can be found in Appendix G. These designs do not require the 2/3 waveplate.

3.5. Detection system

In this section we discuss what kind of detection systems we propose. First, we introduce the concept of post selection. After this, we mention some difficulties large detuning HOMI imposes as compared to (near)degenerate HOMI. After this, we discuss an optical design to solve these problems and the type of detectors we consider.

Post selection

Before we can discuss our detectors properly, we need to discuss post selection, which is a commonly used technique in quantum optics. It refers to detecting only a subset of events while discarding the rest. This typically lowers the detected photon rate but can increase the experimental visibility [35]. However, this improvement comes at the cost of reduced photon counts.

Post-selection is commonly implemented spectrally. In practice, the two downconversion processes can have slightly different spectral amplitudes, introducing a small degree of distinguishability. Placing a line filter after the HOM beam splitter forces the detected spectra to become more similar. This effectively erases spectral which-crystal information of the detected photons. Additionally, the single photon temporal coherence of the detected photons increases, as the spectral linewidth decreases. This method does introduce some additional photon loss, caused by the line filters.

Issues of large detuning HOMI detection

We found two problems that large-detuning HOMI runs into, which are absent in (near-)degenerate HOMI.

The first problem is with spectral post-selection. For degenerate HOMI this is a useful technique. However, for non-degenerate HOMI we cannot use such narrow linewidth filters, as we detect highly non-degenerate photons. There are no narrowband filters available that simultaneously support two wavelengths. Luckily, Bennink [23] states that for the focusing criterion $\xi = 2.5$, the spectral purity, and equivalently the experimental visibility, is maximized. Using these focusing conditions is recommended whenever filtering is not possible.

Unfortunately, the second problem does not have such a convenient solution. The problem is that we are encouraged to maximize the difference between the signal and idler wavelength. More precisely, the Fisher information is proportional to the angular separation Δ. Conventional photon detectors have a limited detection range, after which detection efficiency drops. In general detectors can detect either visible or near infrared (NIR) photons, but not both. This results in a balancing act between maximizing Δ and maintaining sufficiently efficient detection.

In the next section, we propose an altered detection system that both allows for spectral post-selection and utilizes the maximum detection efficiency even for large Δ.

3.5.1. Combined visible and NIR detection

We introduce a solution for signal and idler photons in different detection regimes, while also enabling post selection using line filters. In each detection arm after the HOM beam splitter, we split our signal and idler photons using a dichroic mirror, of which a schematic can be seen in figure 3.7. This allows us to use different detectors for the signal and idler photons. Higher Δ can then be achieved by choosing the signal in the visible and the idler in the NIR regime.

The interference filters for both the signal and idler can now be applied to both arms. In practice, most of the times only filtering one side of the interferometer is sufficient [33, 35] . The equivalent for us, is only filtering the signal or the idler. We will filter the signal in case we only want to filter one photon. In general filtering on the photon whichever has the lowest loss due to other components results in the highest Fisher information.

Photon coincidence counting utilizing 2 different detector types has been done before [24], although not in the context of biphoton interferometry. Coincidence counting with this 4 detector setup is surprisingly simple. We need to build 2 independent counting modules. As a coincidence event always sends the signal to one output of the BS and the idler to the other output. The total number of coincidences can be acquired by adding both coincidence counts together.

This adaptation in detection allows for more detectable correlations. Bunched events can now also be correlated by comparing detection events between the two detectors in a single arm. A bunched event would propagate the signal and idler to their respective detectors inside a single HOM output arm. This kind of correlated measurement for determining the bunched count has the same advantage with respect to dark counts as the coincidence measurements we already perform. Working on this is outside the scope of this thesis and is left for future work.

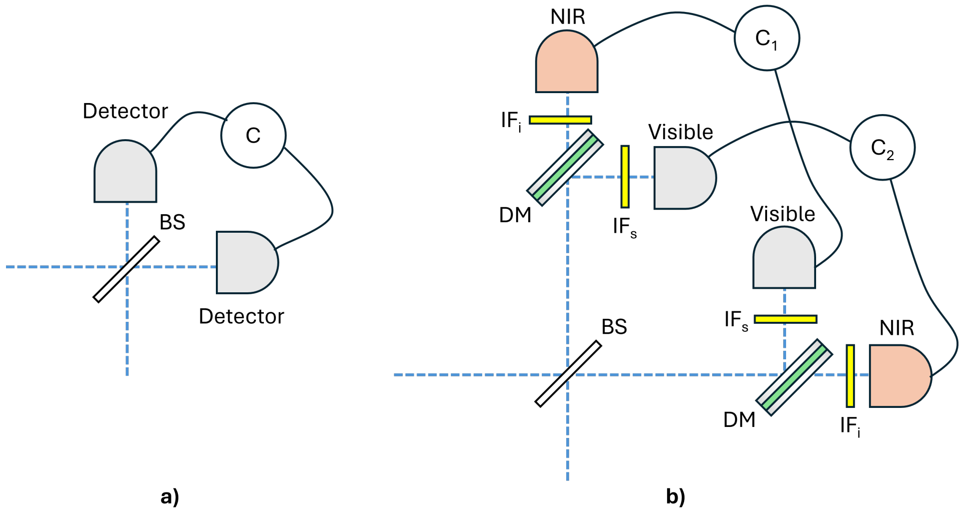

Figure 3.7: Scheme of the detection setup. in figure **a)** general coincidence detection using a correlator (C). in figure **b)** an example scheme for a combined visible and NIR detection can be seen. Here 2 correlators are used, for correlating both possible detection events. In setup **b)** it is possible to use interference filters for increased coherence time and better indistinguishability.

3.5.2. Types of detectors

In this section, we identify and compare the suitability of different kinds of single photon detectors for our experiment. We go over the 2 optical regimes and qualitatively explain the differences between the detectors. For each detector, the assumed parameters can be found in table 3.1 and the efficiency spectrum can be seen in figure 3.8.

Our measurement speed is mainly dependent on 2 quantities: the efficiency and the maximum allowed photon rate. The efficiency of a detector is usually known, while the allowed photon rate is more complex. It is also important to relate the photon rate of your experiment with the dark counts of the detector, which is the false positive detection rate.

The maximum allowed detection rate of a detector is often determined by its dead time, which is the recovery time of a detection event after which a new photon can be detected again. The reciprocal of the dead time sets a hard bound on the measurable photon rate. In general it is advised to operate at photon rates around 10% of the reciprocal of the dead time to prevent missed photon counts [36]. In this thesis, we assume this to be the maximum allowed photon rate at the detector, unless other photon rates are stated in the datasheet.

One design choice in the detection system is to only use free-space detection. The main reason for this is that coupling into single-mode fibers introduces additional loss and requires more careful alignment. In this thesis, we assume a fiber coupling efficiency of 80% whenever we do need it. We only consider fiber coupled detectors when they have considered advantages.

Optical regime

For the visible regime we consider silicon-based single-photon avalanche detectors (Si-SPADs). Si-SPADs provide high detection efficiency in the visible range, low dark counts, and stable timing performance. At elevated count rates, nonlinearities in the readout electronics may occur, and operation is therefore typically maintained below the maximum specified rate. The timing jitter, as stated in the datasheet, determines the minimum practical coincidence window.

Our reference model is the Excelitas SPCM-AQRH-TR [37], and all specifications are taken from the corresponding datasheet.

Infrared regime

For the infrared regime, we considered 2 options: InGaAs SPAD and SNSPD detectors.

InGaAs SPAD

The first one is a InGaAs SPAD detector. Compared to silicon detectors, InGaAs SPADs exhibit lower detection efficiency and higher dark count rates. Controlling these dark counts requires extensive hold of times or Gated measurement. gated measurements are commonly used in pulsed illumination, as the pulse arrival time can be used as a trigger. The only trigger we can use is a signal photon detection event at the Si-SPAD. This is possible, by introducing an extensive delay line for the idler photon to make sure the InGaAs detector can be turned on in time.

In this thesis the InGaAs detector is based on the Micro Photon Devices MDP-PDM-IR free-space version [38], with specifications taken from the manufacturer's datasheet. We will minimize the darkcount by running the detector with a bias voltage of 2V, which will be around 5kc/s. The detector efficiency is not directly stated, however when extrapolating from the datasheet we can assume a peak efficiency between 20% and 25%.

SNSPD

Superconducting nanowire single-photon detectors (SNSPDs) offer significantly higher detection efficiency and improved timing resolution compared to SPAD-based systems [39]. These devices are not yet commercially available and are fiber coupled as these operate cryogenically. SNSPDs do have far better timing precisions than the more affordable Si-SPAD. However, the dead time is still comparable to that of a Si-SPAD. The SNSPD will be modeled after the one used by Chang [40].

SNSPD exist for a wide range of wavelengths. Still, we do not examine SNSPD detectors for the visible regime in this thesis. This is due to the Si-SPAD detectors already working at comparable speeds and efficiencies when accounting for the 80% fiber coupling efficiency.

We investigate a total of 3 different combinations of detectors. The first being a purely visible light setup utilizing only the Si-SPAD detectors as shown in figure 3.7**a)**. For the combined visible and NIR we will investigate both options for infrared regime detectors in combination with the Si-SPAD. Although our focus will be towards the SNSPD detector, because the InGaAs detector needs convoluted gating and optical delays while performing worse across the board.

Detector	Optical range	Peak efficiency	Dark counts	Timing jitter	Ideal detected counts	Hold-off time
Si-SPAD	Visible	75%	1 kc/s	225 ps	1 Mc/s	35 ns
InGaAs SPAD[1]	Infrared	20–25%	5 kc/s	130 ps	100 kc/s	1 μs
SNSPD	Infrared	99%[2]	0.1 kc/s	26 ps	1 Mc/s	97 ns

[1] Operating in gated mode. [2] Achievable under optimal cryogenic conditions.

Table 3.1: Comparison of detector characteristics for the considered single-photon detectors. Values are based on datasheet specifications and model assumptions.

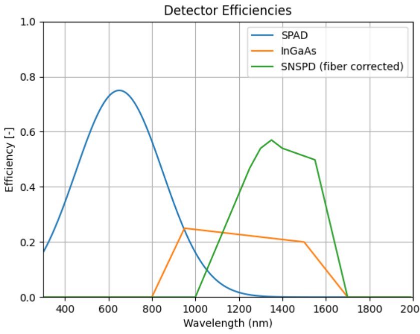

Figure 3.8: Estimated detector efficiencies given for a Si-SPAD detector (SPCM-AQRH-TR) and a InGaAs SPAD (MDP-PDM-IR) and fiber coupling corrected (NIR) SNSPD based on numbers stated in their respective datasheets and paper.

Categorization of coincidence and bunched events

Earlier in the Theory we mentioned we are interested in the number of coincidence and bunched events, as these are the only values we can directly measure. In this section, we discuss how we categorize a detection event as a coincidence or as a bunched event.

This classification is done by time tagging electronics. This device compares the electronic output of 2 (or more) detectors. A coincidence count will be registered whenever it perceives a detection event from both detectors within a specified time window called the coincidence window t_{cw}. Alternatively a bunched event is counted whenever no detection event is perceived from the corresponding detector in the other arm within the coincidence window.

Commercially available devices, for which we take the PicoHarp 330 as an example, are one order of magnitude faster than the detectors we will be analyzing. That is why we will ignore any timing precisions and saturation rates due to time taggers.

the value of t_{cw} is decided by the total uncertainty in detected arrival time of both photons. If the window is to small, we might mislabel some coincidence events. The total uncertainty is a combination of the detector jitter together with the inherent photon jitter. For 1cm ppKTP the photon timing jitter can be calculated to be around the of order 1-10ps. This is negligible compared to the detection jitters found in table 3.1. In table 3.2 we define some rough estimated window sizes.

There is one thing we still need to take into account with these timing windows. We do not want multiple downconverted photons arriving within the same window. As a rule of thumb, having on average 1% of the windows exhibiting a photon pair is considered good for this cause. [41] In table 3.2, the maximum detection rate is based on this rule.

Detector	coincidence window	max detection rate
Si-SPAD	2ns	5Mc/s
Si+InGaAs SPAD	2ns	5Mc/s
Si+SNSPD	1ns	10Mc/s

Table 3.2: Detection system coincidence window estimation with rates, assuming on average 0.01 pairs inside the window to prevent multi pair events.

A comparison of the maximum photon rates based on detector dead time and coincidence window reveals that the detection rate is limited by the recovery time. As a result, minimizing the coincidence window is not one of the priorities for improving the allowed photon rate. Instead, detectors with faster recovery are of importance for further optimization. Switching the Si-SPAD for a visible light SNSPD will not improve the photon rate. That is why no such SNSPD is taken into account in this thesis.

4

Simulations

4.1. HOM simulation

For the HOM simulation we used the probabilities of different HOM outcomes P_1 and P_2 from equation 2.9, the Fisher information from equation 2.27 and finally the MLE estimator $\hat{\tau}$ from equation 2.28.

Here we use the calculated experimental visibility α and photon loss for both wavelengths $\gamma_{s/i}$ from the optical setup simulation.

The next step is to calculate the number of events that 1 or 2 detectors click $N_{1/2}$ in a given measurement time t_m. For this, we use the estimated downconversion rate R_{si} and dark count rate for the detectors R_d. We assume both N_2 and N_1 to be randomly distributed, as both processes occur randomly. Although we create 2 photons, the creation process is based on 1 photon meaning we can use single photon counting statistics. These kinds of processes are Poisson distributed. Now also using the Raikov's theorem which states that the sum of 2 Poisson distributed processes (dark counts and downconverted counts in a given time window) is also Poisson distributed with the parameter being the sum of both parameters.

Up to this point we discussed the effects of different parts of the setup. Now we need to combine the effects of the crystal, spectral filtering and detection into singular values for $\alpha, \Delta, \gamma_{s/i}$ and σ.
Δ is determined by the signal and idler wavelengths of interest, σ is taken from the spectro temporal properties of these downconverted photons arriving at the detector. The total photon loss is given by the probability of the photon not being lost in each part of the process

$$\gamma_{s/i} = 1 - \prod_{e}(1 - \gamma_{s/i,e}) \tag{4.1}$$

Where e is each optical element contribution to the photon loss. In this thesis, we look at the loss acquired by: the crystal focusing, the spectral filtering and the detectors.

4.2. Parameter estimation from a delay scan

During measurements, we assume we do not fully know each parameter, however, we can estimate them. In this part of the simulation, we will look at our ability to estimate these parameters.

We assume rough apriori knowledge of our parameters. For example, we can preemptively do a measurement for the total dark counts. The parameters are estimated by scanning the reference arm delay z. As a reminder, z is the spatial delay equivalent to a temporal delay τ mentioned earlier in the theory.

From here on, we call our collection of simulation parameters θ, and the estimation of the parameters $\hat{\theta}$. We consider the following experiment:

We assume fixed operational wavelengths $\lambda_s = 750$ nm and $\lambda_i = 880$ nm. The photons are created using type-II SPDC in 1cm ppKTP, considering weak focusing ($\xi \leq 1$) for simplicity. These decisions determine the parameters Δ and σ .

For the photon losses $\gamma_{s/i}$ we consider a sample made of silica and detection based on Si-SPAD detectors. R_d is the assumed dark count rate of the Si-SPAD as well.

Finally, we assume $\alpha = 0.8$ and $R_{si} = 100$ kcps. We scan a 5 μm range with a step size of 5 nm. Together with the singular scanning time $t_{scan} = 0.1$ s, this results in an approximate total elapsed time of around 100 s.

R_{si} is considered on the low side so that we can investigate the influence of R_d on our fit quality. The exact values of all mentioned parameters can be found in the second column of table 4.1.

For our parameter estimation, we compare 2 methods of estimation. Both methods are based on least square fitting a reference scan z. We test the most intuitive fitting method based on the coincidence counts (N_2 based fitting) against a fitting method considering both the coincidence counts and single counts (N_2 and N_1 based fitting). We assume Poisson statistics (variance equal to the mean) when determining the weights.

Each parameter has allowed ranges based on apriori knowledge mentioned earlier. For each parameter an allowed range equal to a ratio of the true parameter is given to the fitting function. These ratios can be found in the third column of table 4.1.

Parameter	Value	Relative uncertainty
Δ	3.72×10^{14} rad/s	0.1
σ	2.38×10^{12} rad/s	0.2
α	0.8	0.2
γ_s	0.78	0.4
γ_i	0.88	0.4
R_{si}	100 kcps	0.3
R_d	500 cps	0.3
t_{scan}	0.1 s	1 ns
t_{cw}	2 ns	0.8
step size	5 nm	-
Scan range	5 μm	-

Table 4.1: Model parameters and their assumed relative uncertainties. the parameter t_{scan} has is the exception, as the absolute uncertainty is given.

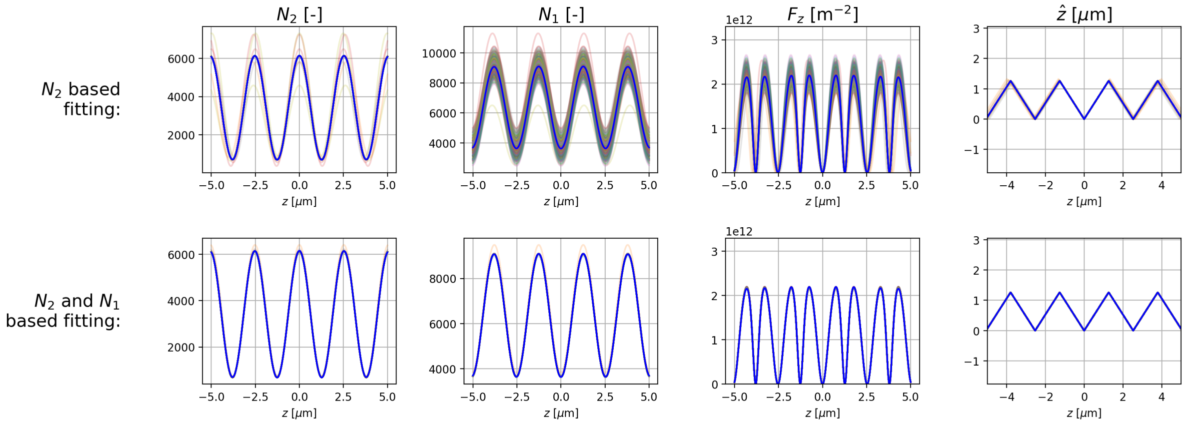

Figure 4.1: Estimated quantities based on the true parameters (blue) and the fitted parameters (half transparent multicolor). The quantities shown are the coincidence counts N_2, single detection counts N_1, Fisher information F_z and position estimation $\hat{z}$

We simulated 300 scans and determined the fitted parameters based on our 2 fitting methods. In figure 4.1, 4 different estimated quantities are shown based on the true parameters and the estimated parameters.

We see that both fitting methods work well for approximating the true N_2 data. N_2 based fitting does a surprisingly well estimation of the delay position, however the uncertainty in N_1 and the dependent parameters result in a larger error in the Fisher information. Fitting based on both the coincidence and bunched seems to be better. In the next simulation, we will focus on the second part of the measurement, determining the step size.

During this thesis, we define 2 methods for quickly checking the quality of the fit. These can be used for controlling the quality of the scan. The first one is a measure based on a normalized L2 distance of the measured data and the fitted curve. More details on this measure can be found in appendix H. The other one is more visual and might be helpful in diagnostics of an experimental setup. Plotting the estimated position $\hat{z}$ over our z scan should show a clear sawtooth. Disfiguration of this pattern indicate improper fitting. In last column on the right in figure 4.1, this quantity is plotted.

4.3. MLE estimation of the step size

Once the parameters are estimated, we can finally measure the depth of a step. The goal of this simulation is to investigate the influence of errors in $\hat{\theta}$ in our measurement of the step.

In this, and the following simulations where we measure the step size, we follow the following scheme. First, we estimate the parameters $\hat{\theta}$ as explained in section 4.2. Then, we move our delay to the position which has the highest estimated Fisher information as defined in equation 2.27. Then we do 2 measurements of 60 seconds. One for each side of the step being $\hat{z}_1(\hat{\theta})$ and $\hat{z}_0(\hat{\theta})$. The step measurement is as defined in section 2.2.3.

We run 300 simulated measurements. Here we consider both parameter estimation methods as a comparison of good and bad fitting. In figure 4.2, the resulting single measurement error is shown, together with the error due to parameter fitting ($\hat{z}(\hat{\theta}) - \hat{z}(\theta)$) and the error of the estimator itself ($\hat{z}(\theta) - z$). The last subplot shows the total measurement error of the step.

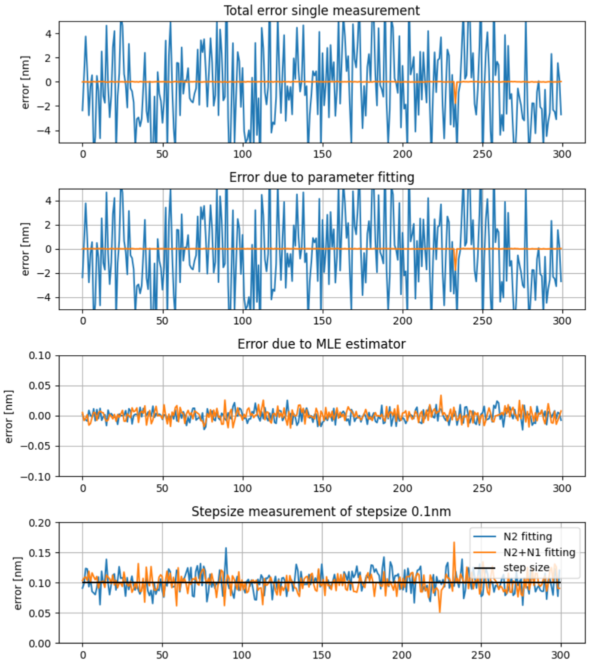

Figure 4.2: Plot showing the noise effects of different parts of the measurement. The first figure shows $\hat{z}(\hat{\theta}) - z$, the second $\hat{z}(\hat{\theta}) - \hat{z}(\theta)$, the third $\hat{z}(\theta) - z$. At last, the measurement of a 0.1 nm step $\hat{z}_{step}$

Here we see something interesting happening. For both methods, we get similar error margins for the step size measurement, while the single point measurements show far larger uncertainties for N_2 based fitting in comparison to N_2 and N_1 based fitting. We can interpret these results as the fitting error of both sides of the step being in ”common mode”. This means that they have identical errors, so the difference in depth should not contain this error. This does imply that this step size measurement is robust for mistakes in parameter estimation.

Effect of dark counts on measurement precision

In this simulation, we look at the breaking point of our parameter estimation. In principle, the Fisher information (and therefore measurement precision) are completely independent of R_d. However, we do want to find the effect of dark counts on our measurement precision. for this simulation we assume the true parameters $\alpha = 0.8$, $\Delta = 10^{15}$rad/s, $\gamma_s = 0.4$, $\gamma_i = 0.8$, $R_{si} = 100$, $t_{scan} = 60$s, $t_m = 3600$s.

We use a similar simulation as before. The difference being that we vary R_d. With proper sampling, we expect a constant precision while varying . In figure 4.3 these results can be seen.

Similar to the results found in the previous simulation, the single point measurement error is dominated by fitting errors. Both fitting methods seem to not have their estimation affected by R_d up to a maximum threshold. N_2 based fitting seems to break for $R_d/R_{si} > 0.2$ while N_2 and N_1 based fitting degrades for $R_d/R_{si} > 100$.

The error due to MLE estimation $\hat{z}(\theta) - z$ seems to increase for $R_d/R_{si} > 1$. This could be explained in future works with thorough analysis the statistical effects of Poisson-distributed noise.

Finally, step size error seems to be constant for $R_d/R_{si} \leq 1$, implying proper sampling. From here on out, we assume proper sampling for our simulations.

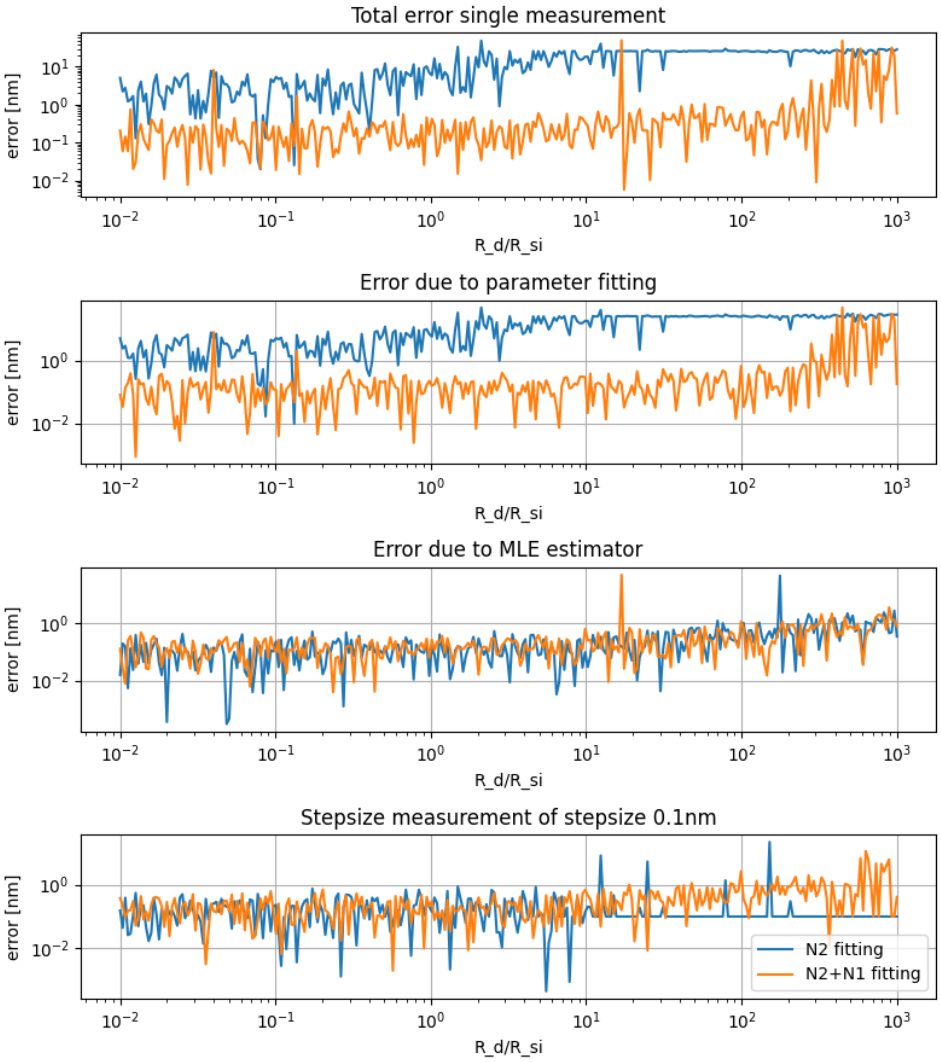

Figure 4.3: Plot showing the noise effects of different parts of the measurement.the horizontal axis shows R_d, normalized with respect to R_{si}. The first figure shows $\hat{z}(\hat{\theta}) - z$, the second $\hat{z}(\hat{\theta}) - \hat{z}(\theta)$, the third $\hat{z}(\theta) - z$. At last, the measurement of a 0.1 nm step $\hat{z}_{step}$

4.4. QCR saturation

The goal of the next simulation is to show that our overall proposed methodology saturates the QCR method. As a reminder, our proposed method is making a scan for parameter estimation, followed by a Fisher information maximized measurement.

We want to test our methodology for a wide range of variables. That is why we will run a large Monte-Carlo simulations with combinations of randomly generated parameters.

Here we check the average behavior of the average standard deviation over the QCR bound. The ratio $\frac{\text{Std}[\hat{z}_{step}(\hat{\theta})]}{z_{step,QCR}}$ should be equal to 1 whenever the measurement is quantum limited. The results of this simulation can be seen in figure 4.4.

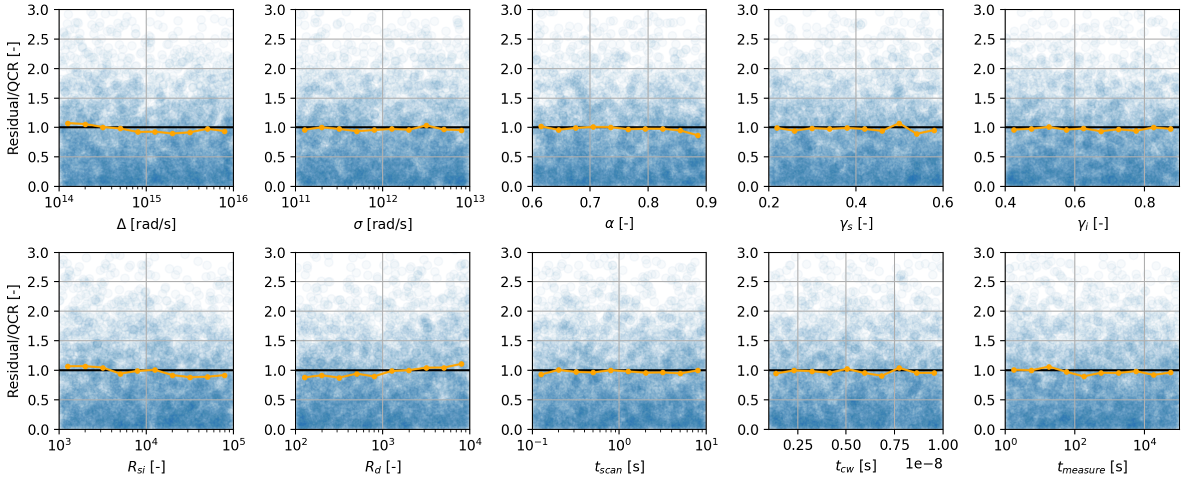

Figure 4.4: Results of Monte Carlo simulation,in blue residual of a measurement over the QCR limit of that simulation. In orange, the local standard deviation in residuals over QCR bound. The vertical label refers to Std$[\hat{z}_{step}(\hat{\theta})]/z_{step,QCR}$.

Here we see that we are operating around the QCR bound, implying that this measurement method is in practice quantum limited as well.

This also verifies what we stated in section 2.2.2. Which is, that the events where both downconverted photons are lost N_0 needs to be considered for the overall number of measurements when calculating $z_{step,QCR}$. Otherwise, the predicted $z_{step,QCR}$ would have been to large resulting in a smaller ratio.

4.5. Optimized wavelength and SPDC focusing

In this part, we move to a more experimental approach. Here, we determine the optimal operational parameters for our proposed HOM interferometer. As discussed, we will focus on the Si-SPAD + SNSPD detection system. We investigate both type-II and type-0 SPDC. Also, the possibility to do a measurement with or without post selection is investigated.

This simulation will no longer do a full measurement simulation as we did previously. To save computational complexity, we instead focus on optimization of the measurement speed κ_{step} as defined in section 2.2.4.

We optimize over the downconverted wavelengths $\lambda_{s/i}$ and the illumination/collection focusing. The illumination and collection focusing will be represented by the parameters ξ_p and ξ_s respectively as discussed in section 2.3.5. In this section we also discuss how these quantities are experimentally chosen by selecting the right focal lengths f_p and f_c.

The pump intensity we can use is limited by a number of constraints. The first set of constraints is set by the detection system. Here, we keep the detector and coincidence window saturation as discussed in section 3.5 in mind. The second set of constraints are crystal based and are discussed in section 2.3.5. More explicitly, these are based on model assumptions [23], intensity damage treshold [25] and signal/idler walkoff effects (equation 2.52.

Implementation filter/filterless interference

For filterless interference we know that the visibility is maximized for $\xi \approx 2.5$ [23]. Our approach will be to choose $\xi_p = 2.5$ and find the best fitting collection focusing. For filtered experiments, we are free to choose any focusing condition.

The exact calculations on α and the effect of filtering is outside the scope of this thesis. We will assume a tradeoff in visibility. We assume an experimental visibility $\alpha = 0.8$ for filterless interference. For filtered interference we assume $\alpha = 0.9$ and signal photon loss of 10% due to filtering.

The simulation results for κ_{step} with optimized focusing can be found in figure 4.5.

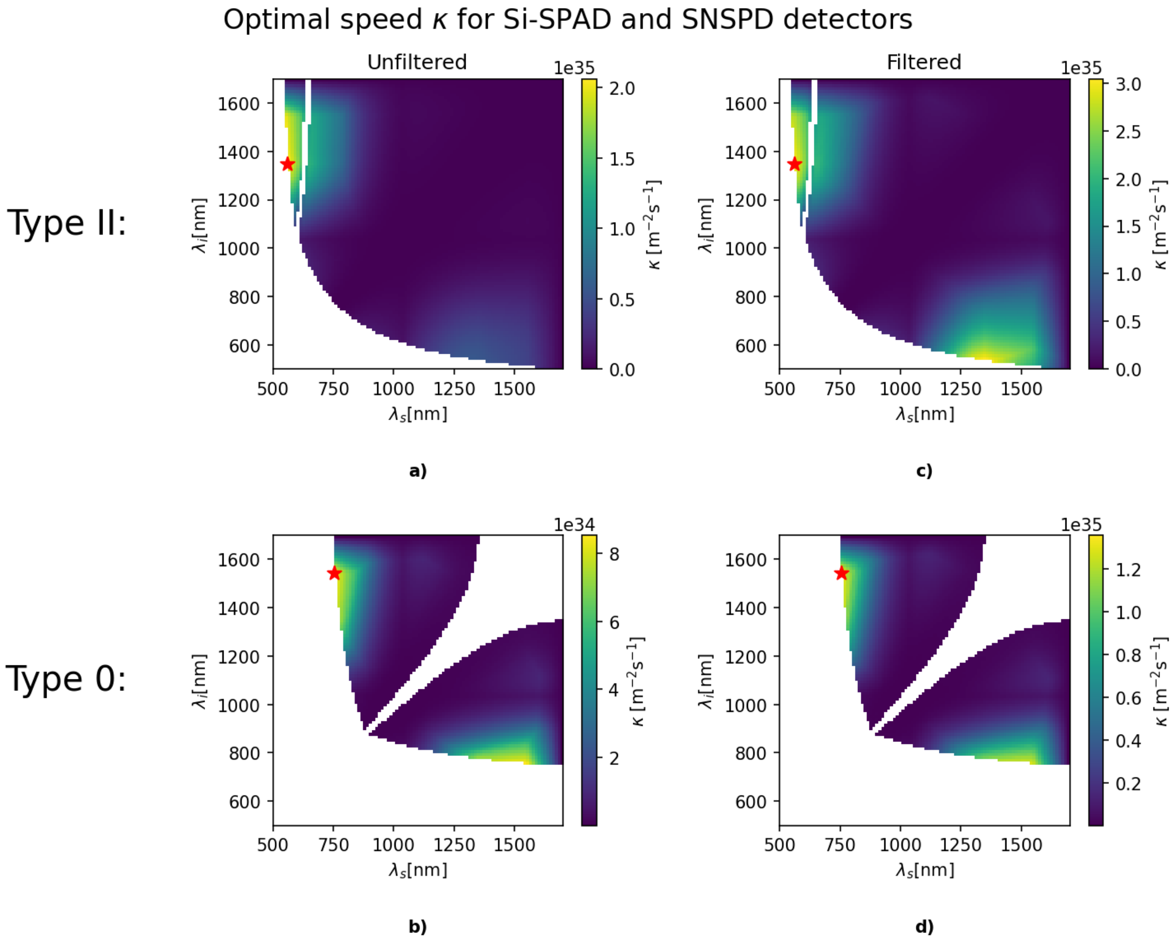

Figure 4.5: Optimized measurement speed κ for type-II and type-0 SPDC and with or without post selection in the form of spectral filtering.

One interesting result we find, is that both filtered and unfiltered situation result in the same optimal operational wavelengths. For type-II these are $\lambda_s = 561$ nm and $\lambda_i = 1348$ nm. The optimal measurement speed is in the filtered case with a speed of measure $\kappa_{step} = 3.04 \times 10^{35}$ m^{-2}s^{-1}. This is equivalent to a measurement time of around 7.4 seconds for a standard deviation of 0.1 nm.

For type-0 we have $\lambda_s = 755$ nm and $\lambda_i = 1542$ nm. We again have the highest speed of measure in the filtered case, being $\kappa_{step} = 1.36 \times 10^{35}$ m^{-2}s^{-1}. This is equivalent to a measurement time of around 716.6 seconds for a standard deviation of 0.1 nm.

More details on the optimal settings and values can be found in appendix I.

The optimal focusing criteria in the filtered simulation are far in the weak focusing regime, As far as the bounds of our simulation. This is the case for both kinds of SPDC processes. We further investigate the space of focusing criteria ξ_p and ξ_s at the optimal operational wavelengths. The results can be seen in figure 4.6

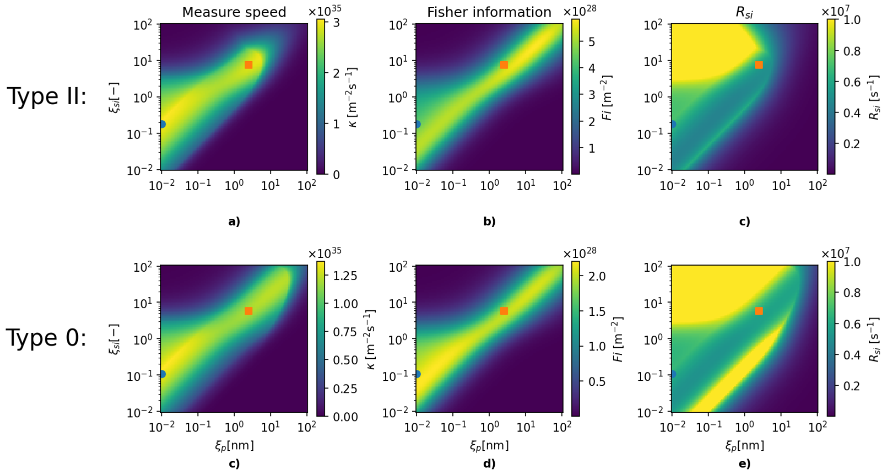

Figure 4.6: Evaluation of the focusing conditions at optimal operational wavelengths. measurement speed κ_{step}, related Fisher information and photon rate R_{si} for both type-II and type-0 SPDC are shown.The blue circle and orange square are the optimal focusing condition for the filtered and filterless focusing conditions, respectively.

As we can see here, the measurement speed is optimized for low focusing criteria. It seems the lower photon losses of weak focusing are more of an advantage than the increased downconversion efficiency of strong focusing. Interestingly, there are 2 local maxima around both focusing conditions mentioned: the optimal weak focusing ($\xi \ll 1$) we found, and one close to the conditions as mentioned by Bennik[23].

We do now see a smaller difference between the measurement speed at the 2 earlier found optimal focusing conditions compared to the previous simulation. That is because we now assume for the whole simulation the increased visibility due to filtering. When comparing the filterless focusing condition, to the freely chosen filtered condition, we see for type-2, a 5% increase and, for type-0, a 15% increase.

R_{si} has a more complicated shape. The reason for this, is that this number is proportional to the pump power, which we maximize up to our conditions mentioned at the beginning of this section. In figure 4.7, we show the saturation of these bounds for this simulation. The saturation of the bounds can be used as a way to characterize the limiting factor of the setup. For both focusing criteria, this is due to the Si-SPAD maximum allowed detection rate. However, the pump power for the optimal focusing is closer to the maximum.

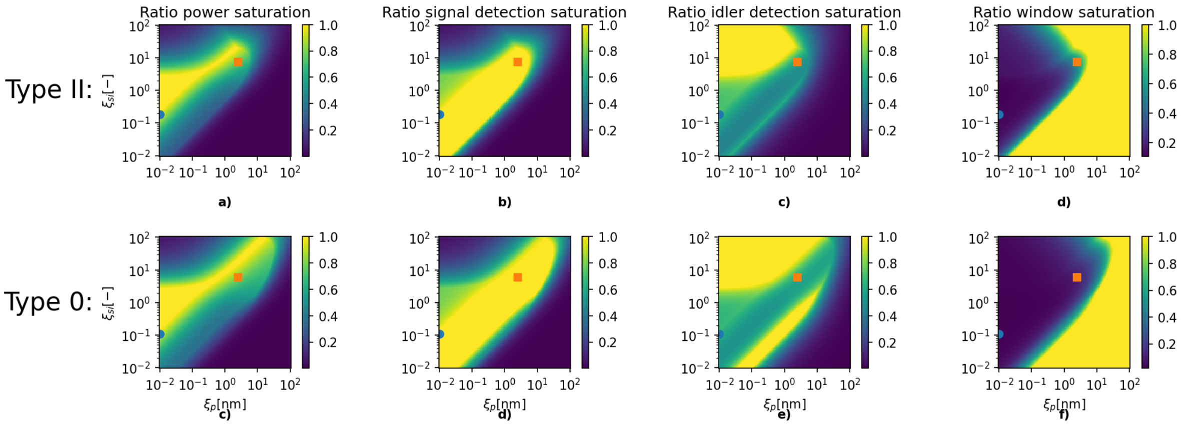

Figure 4.7: Saturation of the different restrictions at different focusing conditions at the optimal wavelength for both type-II and type-0 SPDC.

4.6. Sensitivity analysis

The last simulation we show is a sensitivity analysis of our best setup found in the previous section, which is the filtered type-II setup utilizing detection based on Si-SPAD and SNSPD. We once again base this analysis on a Monte-Carlo simulation, similar to our QCR saturation simulation. This time, the goal is to make the parameter range small instead. We choose a maximum deviation of $\pm 10\%$.

The sensitivity is defined as the normalized slope of a linear fit.

A linear fit is applied to find the average standard deviation. Also, the QCR limit is plotted. This analysis technique could easily be adopted for other parameters such as detector efficiency or SPDC misalignment. The results can be seen in figure 4.8. Here, we see for example that the biggest impact can be made by minimizing the photon losses.

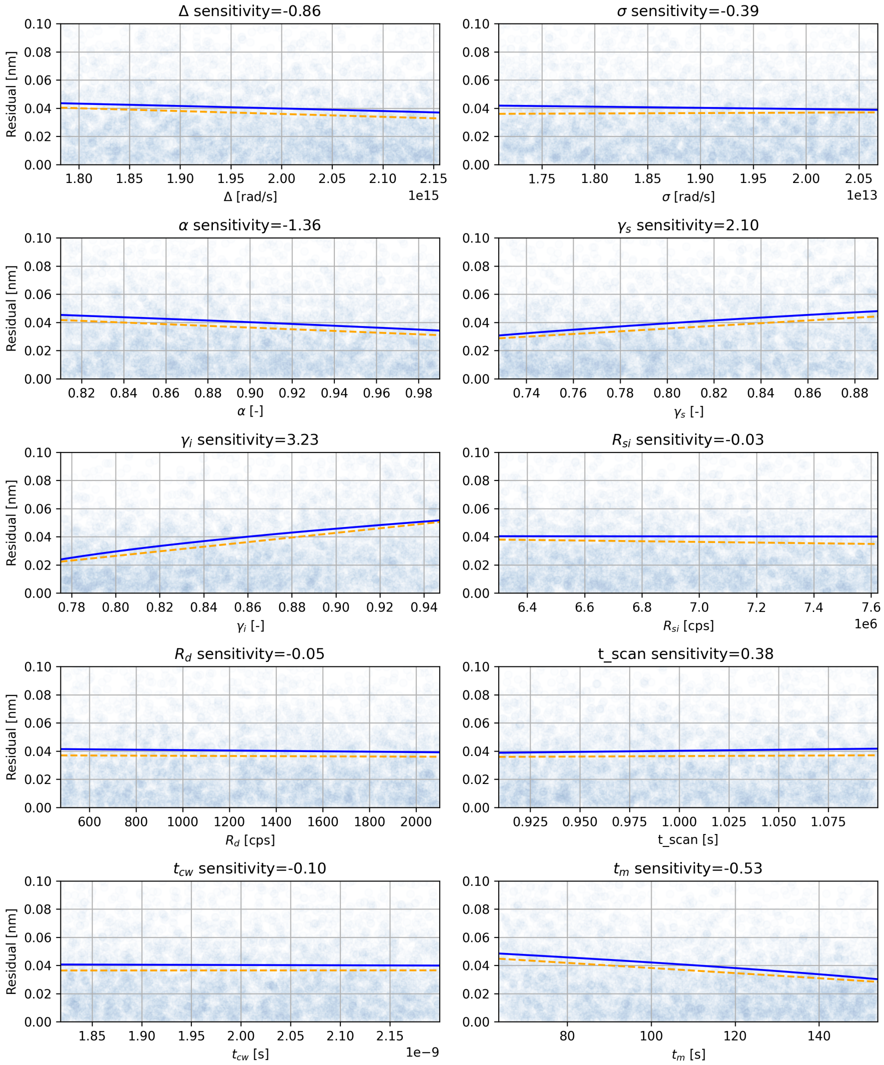

Figure 4.8: Sensitivity analysis performed on the optimal parameters estimated before. The blue background are individual simulations. The blue line is the fitted average measurement error. The orange dashed line is the average QCR bound.

5

Discussion

Theoretical basis

During simulation we saw that, even for perfectly estimated parameters, dark counts had an influence on the single spatial measurement for $R_d/R_{si} > 1$. This effect can be seen in figure 4.3. Although a logical outcome, this is not accounted for in our mathematical background. A more thorough statistical derivation of randomly distributed dark counts could explain this dependency.

Setup design

In this thesis, we assume CW pumping, with a linewidth negligible to the downconversion linewidth. However, when the processes are spectrally distinguishable (for example, when the 2 downconversion crystals are not identical), we can use a broader pump to dominate the spectral behavior, erasing the spectral distinguishability [42].

We did not go into further detail into all setups discussed in the appendix. Some of the concepts are still promising, albeit not for our purposes. The beam displacer based interferometer in appendix F.5 is the most promising, however, for large detuning HOMI engineering achromatic beam displacers should be considered.

As mentioned in the detector part, the detectors themselves could be further optimized. This can result in higher measurement precision than reported here.

The introduced combined detector setup allows for heralded bunched events as discussed. This might improve the measurement, however, one does need to reconsider the Fisher information based derivation for proper evaluation of what is possible.

The use of SNSPD detectors is interesting for future research. These detectors are also available around even larger wavelengths, resulting in considerably higher possible detunings. Additionally, this is a quickly changing research field, meaning, that a lot is possible in the near future.

Simulation

The simulated photon counts could be more realistic. Random photon counts are considered Poisson distributed. However, if there exists a large enough uncertainty in the average rate, the distribution becomes effectively negative binomial [43].

The process of parameter estimation by fitting can be improved upon. We did discuss 2 different methods, however both of these are still rather basic. Optimizing these scans is up to a future experimentalist. A suggested improvement would be to do an additional rough scan to better determine the envelope of the interference. This would determine the downconverted linewidth σ directly as well.

Some quantities have been estimated in the simulation process. One of these is effect of filtering. Due to time constraints, the exact spectrum from the SPDC focusing theory of Bennink [23] was not implemented. This made it impossible to properly calculate the exact effects of spectral filtering.

The best optimized operational resulting from our simulations in section 4.5 parameters do have one flaw. The optimal solutions found are in the weak focusing regime, resulting in the need for higher pump powers. For Si-SPAD and SNSPD type-2 filtered setup, which is our best performing setup, we get a needed pump power of 842 mW. This is most likely enough power to introduce thermal effects [25], which we did not account for in this thesis. A possible workaround is using longer crystals. Switching to 3cm long ppKTP could reduce the needed pump power by a factor 9, as the downconversion rate in the weak focusing regime scales with the square of the crystal length.

The sensitivity analysis we did can be expanded for any kind of parameter. Currently, it is only applied on the model parameters. However, the framework can be easily altered to more experimental parameters as mirror reflectivity or even the effect of alignment errors.

6

Conclusion

In this thesis, we looked at the feasibility of a Biphoton HOM interferometer for measuring a step size with a sub nm precision.

We derived a model for biphoton HOMI with unbalanced photon losses between the signal and idler photon. Furthermore, we derived an expression for the experimental visibility and identified possible causes for loss in the experimental setup. This expression is highly flexible for adaptation of other sources of distinguishability.

A useful quantity directly relating to the effectiveness of a detection system has been introduced. The quantity in question is the speed of measure κ_{step} and is based on the Fisher information and the downconverted photon pair rate. It was found and verified in simulation that undetected pairs also need to be accounted for in this quantity.

Guidelines have been made for making effective HOM interferometry setups. Using these guidelines, a robust experimental design has been proposed.

A biphoton source, which works similar to beam displacer based entangled photon sources, has been proposed. Our design is highly adaptable and does not use dispersive components, minimizing the need for chromatic corrections. We found experimentally viable type-II and type-0 SPDC based photon sources utilizing the signal photon in the visible and idler in the NIR regime.

The suggested HOM interferometer is based on a shown mathematical equivalent beam splitter interaction. This interaction utilizes a singular spatial input of a PBS instead of the two spatial inputs used in conventional HOMI. This allows for a lot of common path, minimizing which path information.
We propose a detection scheme which could help realize larger detuning than previously done before, with the signal and idler photons in different optical regimes. This method also allows for spectral post selection, which did not seem achievable for non degenerate HOMI.
We investigated 2 methods of parameter investigation based on least square fitting a scan over the delay with a theoretical model. The best estimation was achieved where we fit the parameters to both the coincidence and single counts simultaneously.

We found that our proposed measurement of a step is robust to errors in parameter estimation, making it a reliable technique. Additionally, we found that QCR limited measurements are experimentally achievable with our suggested measurement of a sub-nanometer step.

Experimental parameters have been optimized for each suggested setup, and optimized signal and idler wavelengths for experimentally viable type-II and type-0 SPDC based photon sources utilizing the signal photon in the visible and idler in the NIR regime.

We found the best results for a biphoton state generated using type-II SPDC based on Si-SPAD and NIR SNSPD detectors, resulting in an estimated measure time of 7.4 seconds for a 0.1 nm standard deviation of the measured step size. Type-0 SPDC might be slightly easier to achieve due to this variant of the setup not needing extra waveplates. The time needed for an equivalent precision would be 16.6 seconds.

Finally, we introduce a sensitivity analysis based on a Monte-Carlo simulation, which is highly adaptable to find the influence of any parameter on the sensitivity.

References

[1] C. K. Hong, Z. Y. Ou, and L. Mandel. “Measurement of Subpicosecond Time Intervals between Two Photons by Interference”. In: *Physical Review Letters* 59.18 (Nov. 1987), pp. 2044–2046. ISSN: 0031-9007. DOI: `10.1103/PhysRevLett.59.2044`. (Visited on 01/08/2025).

[2] S. Ramelow et al. “Discrete, Tunable Color Entanglement”. In: *Physical Review Letters* 103.25 (Dec. 2009), p. 253601. ISSN: 0031-9007, 1079-7114. DOI: `10.1103/PhysRevLett.103.253601`. arXiv: `0904.4916 [quant-ph]`. (Visited on 11/27/2025).

[3] Fabrice Devaux et al. “Imaging Spatiotemporal Hong-Ou-Mandel Interference of Biphoton States of Extremely High Schmidt Number”. In: *Physical Review X* 10.3 (Aug. 2020), p. 031031. ISSN: 2160-3308. DOI: `10.1103/PhysRevX.10.031031`. (Visited on 08/14/2025).

[4] Yuanyuan Chen, Ling Hong, and Lixiang Chen. “Quantum Interferometric Metrology with Entangled Photons”. In: *Frontiers in Physics* 10 (Sept. 2022), p. 892519. ISSN: 2296-424X. DOI: `10.3389/fphy.2022.892519`. (Visited on 01/08/2025).

[5] Ashley Lyons et al. “Attosecond-Resolution Hong-Ou-Mandel Interferometry”. In: *Science Advances* 4.5 (May 2018), eaap9416. ISSN: 2375-2548. DOI: `10.1126/sciadv.aap9416`. arXiv: `1708.08351 [quant-ph]`. (Visited on 01/29/2025).

[6] Yuanyuan Chen et al. “Hong-Ou-Mandel Interferometry on a Biphoton Beat Note”. In: *npj Quantum Information* 5.1 (May 2019), p. 43. ISSN: 2056-6387. DOI: `10.1038/s41534-019-0161-z`. (Visited on 01/08/2025).

[7] Agata M. Brańczyk. *Hong-Ou-Mandel Interference*. Oct. 2017. DOI: `10.48550/arXiv.1711.00080`. arXiv: `1711.00080 [quant-ph]`. (Visited on 06/10/2025).

[8] Christian Drago and Agata M. Brańczyk. “Hong–Ou–Mandel Interference: A Spectral–Temporal Analysis”. In: *Canadian Journal of Physics* 102.8 (Aug. 2024), pp. 411–421. ISSN: 0008-4204, 1208-6045. DOI: `10.1139/cjp-2023-0312`. (Visited on 06/10/2025).

[9] Nicolas Fabre and Simone Felicetti. “Parameter Estimation of Time and Frequency Shifts with Generalized HOM Interferometry”. In: (2021). DOI: `10.48550/ARXIV.2106.00653`. (Visited on 03/12/2025).

[10] Neng Cai et al. “Broadband-Laser-Diode Pumped Periodically Poled Potassium Titanyl Phosphate-Sagnac Polarization-Entangled Photon Source”. In: *Journal of the Optical Society of America B* 39.1 (Jan. 2022), p. 77. ISSN: 0740-3224, 1520-8540. DOI: `10.1364/JOSAB.437808`. (Visited on 01/17/2025).

[11] S. P. Walborn et al. “Multimode Hong-Ou-Mandel Interference”. In: *Physical Review Letters* 90.14 (Apr. 2003), p. 143601. ISSN: 0031-9007, 1079-7114. DOI: `10.1103/PhysRevLett.90.143601`. arXiv: `quant-ph/0212017`. (Visited on 08/14/2025).

[12] Pavel Trojek. *Efficient Generation of Photonic Entanglement and Multiparty Quantum Communication*. 2007.

[13] Samuel L. Braunstein, Carlton M. Caves, and G. J. Milburn. “Generalized Uncertainty Relations: Theory, Examples, and Lorentz Invariance”. In: *Annals of Physics* 247.1 (Apr. 1996), pp. 135–173. ISSN: 00034916. DOI: `10.1006/aphy.1996.0040`. arXiv: `quant-ph/9507004`. (Visited on 01/08/2025).

[14] Baihong Li et al. *Quantum Metrology Timing Limits of Biphoton Frequency Comb*. Oct. 2024. DOI: `10.48550/arXiv.2410.16841`. arXiv: `2410.16841 [quant-ph]`. (Visited on 03/25/2025).

[15] Fetsje Bijma, Marianne Jonker, and Aad W. van der Vaart. *An Introduction to Mathematical Statistics*. Amsterdam: Amsterdam University Press, 2017. ISBN: 978-94-6298-510-0.

[16] Kiyoshi Kato and Eiko Takaoka. “Sellmeier and Thermo-Optic Dispersion Formulas for KTP”. In: *Applied Optics* 41.24 (Aug. 2002), p. 5040. ISSN: 0003-6935, 1539-4522. DOI: 10.1364/AO.41.005040. (Visited on 03/28/2025).

[17] H. Zhao, I. T. Lima Jr., and A. Major. “Peculiarities of Temperature-Dependent Sellmeier Equations for Periodically Poled KTiOPO 4 Crystal in the near-Infrared and Visible Ranges”. In: *Photonics North 2010*. Ed. by Henry P. Schriemer and Rafael N. Kleiman. Niagara Falls, Canada, June 2010, p. 77501D. DOI: 10.1117/12.872906. (Visited on 03/28/2025).

[18] Michael V. Pack, Darrell J. Armstrong, and Arlee V. Smith. “Measurement of the χ^(2) Tensors of KTiOPO_4, KTiOAsO_4, RbTiOPO_4, and RbTiOAsO_4 Crystals”. In: *Applied Optics* 43.16 (June 2004), p. 3319. ISSN: 0003-6935, 1539-4522. DOI: 10.1364/AO.43.003319. (Visited on 10/28/2025).

[19] Insight Scientific. *External cavity diode laser (ECDL) – 405 nm system*. Accessed: 2026-03-25. n.d. URL: https://www.insight-scientific.us/ecdllaser.

[20] P. Trojek and H. Weinfurter. “Collinear Source of Polarization-Entangled Photon Pairs at Nondegenerate Wavelengths”. In: *Applied Physics Letters* 92.21 (May 2008), p. 211103. ISSN: 0003-6951, 1077-3118. DOI: 10.1063/1.2924280. (Visited on 03/19/2025).

[21] Fumihiro Kaneda et al. “Direct Generation of Frequency-Bin Entangled Photons via Two-Period Quasi-Phase-Matched Parametric Downconversion”. In: *Optics Express* 27.2 (Jan. 2019), p. 1416. ISSN: 1094-4087. DOI: 10.1364/OE.27.001416. (Visited on 03/25/2025).

[22] Natalia Kamanina, ed. *Nonlinear Optics*. InTech, Feb. 2012. ISBN: 978-953-51-0131-4. DOI: 10.5772/2073. (Visited on 03/12/2025).

[23] Ryan S. Bennink. “Optimal Collinear Gaussian Beams for Spontaneous Parametric Down-Conversion”. In: *Physical Review A* 81.5 (May 2010), p. 053805. ISSN: 1050-2947, 1094-1622. DOI: 10.1103/PhysRevA.81.053805. (Visited on 01/17/2025).

[24] Minjae Hong et al. “Polarization-Entangled Photon-Pair Source Using Beam Displacers and Thin Crystals”. In: *Optics Letters* 49.19 (Oct. 2024), p. 5467. ISSN: 0146-9592, 1539-4794. DOI: 10.1364/OL.536820. (Visited on 03/14/2025).

[25] Ole Bjarlin Jensen et al. “Generation of more than 300 mW diffraction-limited light at 405 nm by second-harmonic generation of a tapered diode laser with external cavity feedback”. In: ed. by Peter E. Powers. San Jose, CA, Feb. 2007, p. 645503. DOI: 10.1117/12.700276. URL: http://proceedings.spiedigitallibrary.org/proceeding.aspx?doi=10.1117/12.700276 (visited on 02/19/2026).

[26] Martin A. Green. “Self-consistent optical parameters of intrinsic silicon at 300K including temperature coefficients”. en. In: *Solar Energy Materials and Solar Cells* 92.11 (Nov. 2008), pp. 1305–1310. ISSN: 09270248. DOI: 10.1016/j.solmat.2008.06.009. URL: https://linkinghub.elsevier.com/retrieve/pii/S0927024808002158 (visited on 12/19/2025).

[27] Masahiro Kamada, Ken-ichi Sasaki, and Tomohiro Matsui. “Comprehensive Study of Optical Contrast, Reflectance, and Raman Spectroscopy of Multilayer Graphene”. In: *Carbon Trends* 16 (Sept. 2024), p. 100389. ISSN: 26670569. DOI: 10.1016/j.cartre.2024.100389. (Visited on 12/17/2025).

[28] Riza Fazili et al. “Simple but Efficient Polarization-Entangled Photon Sources”. In: *Journal of the Optical Society of America B* 41.12 (Dec. 2024), p. 2692. ISSN: 0740-3224, 1520-8540. DOI: 10.1364/JOSAB.531089. (Visited on 03/14/2025).

[29] Tingkui Mu et al. “Achromatic Savart Polariscope: Choice of Materials”. In: *Optics Express* 22.5 (Mar. 2014), p. 5043. ISSN: 1094-4087. DOI: 10.1364/OE.22.005043. (Visited on 03/31/2025).

[30] Ali Anwar et al. “Entangled Photon-Pair Sources Based on Three-Wave Mixing in Bulk Crystals”. In: *Review of Scientific Instruments* 92.4 (Apr. 2021), p. 041101. ISSN: 0034-6748, 1089-7623. DOI: 10.1063/5.0023103. (Visited on 03/17/2025).

[31] Yuanyuan Chen et al. “Polarization Entanglement by Time-Reversed Hong-Ou-Mandel Interference”. In: *Physical Review Letters* 121.20 (Nov. 2018), p. 200502. ISSN: 0031-9007, 1079-7114. DOI: 10.1103/PhysRevLett.121.200502. arXiv: 1807.00383 [quant-ph]. (Visited on 01/29/2025).

[32] Sandra Meraner et al. “Approaching the Tsirelson Bound with a Sagnac Source of Polarization-Entangled Photons”. In: *SciPost Physics* 10.1 (Jan. 2021), p. 017. ISSN: 2542-4653. DOI: `10.21468/SciPostPhys.10.1.017`. (Visited on 03/14/2025).

[33] Fabian Steinlechner et al. “Phase-Stable Source of Polarization-Entangled Photons in a Linear Double-Pass Configuration”. In: *Optics Express* 21.10 (May 2013), p. 11943. ISSN: 1094-4087. DOI: `10.1364/OE.21.011943`. arXiv: `1305.1519 [quant-ph]`. (Visited on 01/19/2025).

[34] G. Paganini et al. “High-Quality Entangled Photon Source by Symmetric Beam Displacement Design”. In: *APL Photonics* 10.3 (Mar. 2025), p. 031302. ISSN: 2378-0967. DOI: `10.1063/5.0225901`. (Visited on 03/31/2025).

[35] Si Wang et al. “Research on the Hong-Ou-Mandel Interference with Two Independent Sources”. In: *Scientific Reports* 9.1 (Mar. 2019), p. 3854. ISSN: 2045-2322. DOI: `10.1038/s41598-019-40720-5`. (Visited on 08/12/2025).

[36] W. Becker. *The bh TCSPC handbook*. 11th edition. 2026. URL: `www.becker-hickl.com`.

[37] Excelitas. *Data Sheet SPCM-AQRH Single Photon Counting Module*. 2020.

[38] *MPD_PDM-IR_Datasheet_Freespace*. URL: `https://www.micro-photon-devices.com/products/single-pixels/pdm-ir`.

[39] Iman Esmaeil Zadeh et al. “Superconducting nanowire single-photon detectors: A perspective on evolution, state-of-the-art, future developments, and applications”. en. In: *Applied Physics Letters* 118.19 (May 2021), p. 190502. ISSN: 0003-6951, 1077-3118. DOI: `10.1063/5.0045990`. URL: `https://pubs.aip.org/apl/article/118/19/190502/1062620/Superconducting-nanowire-single-photon-detectors-A` (visited on 02/20/2026).

[40] J. Chang et al. “Detecting telecom single photons with 99.5−2.07+0.5% system detection efficiency and high time resolution”. en. In: *APL Photonics* 6.3 (Mar. 2021), p. 036114. ISSN: 2378-0967. DOI: `10.1063/5.0039772`. URL: `https://pubs.aip.org/app/article/6/3/036114/831362/Detecting-telecom-single-photons-with-99-5-2-07-0` (visited on 02/10/2026).

[41] Fabian Steinlechner et al. “A High-Brightness Source of Polarization-Entangled Photons Optimized for Applications in Free Space”. In: *Optics Express* 20.9 (Apr. 2012), p. 9640. ISSN: 1094-4087. DOI: `10.1364/OE.20.009640`. arXiv: `1204.5330 [quant-ph]`. (Visited on 01/08/2025).

[42] Fumihiro Kaneda et al. “Heralded Single-Photon Source Utilizing Highly Nondegenerate, Spectrally Factorable Spontaneous Parametric Downconversion”. In: *Optics Express* 24.10 (May 2016), p. 10733. ISSN: 1094-4087. DOI: `10.1364/OE.24.010733`. (Visited on 09/05/2025).

[43] Lior Cohen et al. “Measuring the Schmidt Number of Parametric down Conversion by Exploiting Photon Distribution”. In: *AVS Quantum Science* 5.2 (June 2023), p. 025002. ISSN: 2639-0213. DOI: `10.1116/5.0147694`. (Visited on 01/15/2025).

[44] Heonoh Kim, Sang Min Lee, and Han Seb Moon. “Two-photon interference of temporally separated photons”. en. In: *Scientific Reports* 6.1 (Oct. 2016), p. 34805. ISSN: 2045-2322. DOI: `10.1038/srep34805`. URL: `https://www.nature.com/articles/srep34805` (visited on 01/24/2026).

[45] Onur Kuzucu et al. “Joint Temporal Density Measurements for Two-Photon State Characterization”. en. In: *Physical Review Letters* 101.15 (Oct. 2008), p. 153602. ISSN: 0031-9007, 1079-7114. DOI: `10.1103/PhysRevLett.101.153602`. URL: `https://link.aps.org/doi/10.1103/PhysRevLett.101.153602` (visited on 01/24/2026).

[46] N. L. Carothers. *Real Analysis*. Cambridge university press, 2006.

A

HOM mathematics

A.1. Derivation and visibility calculation: HOM effect

Here we derive the general HOM effect together with a measure of the visibility. This part is also a stepping stone for the reader to better follow the steps taken for the Bi-photon derivation in appendix A.2. This one follows similar steps and is less cumbersome.

As an input state we have:

$$|\Phi_{in}\rangle = |1\rangle_1|1\rangle_2 = \hat{a}_1^\dagger\hat{b}_2^\dagger|0\rangle \tag{A.1}$$

Here we label the (creation) operators of the photon on the second path of the beam splitter with operators $\hat{b}$, which behaves the same as $\hat{a}$. We do this to make it possible to distinguish the 2 photons for distinguishability calculations. As a reminder, annihilation and creation operators are each others complex conjugate with the following commutation relation:

$$\left[\hat{a}_j, \hat{a}_k^\dagger\right] = \delta_{jk} \tag{A.2}$$

The beam splitter has the following transformation for creation operators for transforming photons from the inputs to the outputs:

$$\hat{a}_1^\dagger \rightarrow \frac{\hat{a}_3^\dagger - i\,\hat{a}_4^\dagger}{\sqrt{2}}, \quad \hat{a}_2^\dagger \rightarrow \frac{\hat{a}_4^\dagger - i\,\hat{a}_3^\dagger}{\sqrt{2}} \tag{A.3}$$

Taking the Hermitian conjugate gives the same relation annihilation operators

$$\hat{a}_1 \rightarrow \frac{\hat{a}_3 + i\,\hat{a}_4}{\sqrt{2}}, \quad \hat{a}_2 \rightarrow \frac{\hat{a}_4 + i\,\hat{a}_3}{\sqrt{2}} \tag{A.4}$$

Now we can calculate the effect of this beam split on our input state in equation A.1

$$|\Phi_{in}\rangle = \hat{a}_1^\dagger\hat{b}_2^\dagger|0\rangle \rightarrow \frac{1}{2}(\hat{a}_3^\dagger - i\hat{a}_4^\dagger)(\hat{b}_4^\dagger - i\hat{b}_3^\dagger)|0\rangle \tag{A.5}$$

Working out the algebra gives:

$$|\Phi_{out}\rangle = \frac{1}{2}\left[\left(\hat{a}_3^\dagger\hat{b}_4^\dagger - \hat{a}_4^\dagger\hat{b}_3^\dagger\right) - i\left(\hat{a}_3^\dagger\hat{b}_3^\dagger + \hat{a}_4^\dagger\hat{b}_4^\dagger\right)\right]|0\rangle \tag{A.6}$$

The left part of this state is the coincidence state, as we have both a photon in path 3 and path 4.

$$|\Phi_c\rangle = \frac{1}{2}\left(\hat{a}_3^\dagger\hat{b}_4^\dagger - \hat{a}_4^\dagger\hat{b}_3^\dagger\right)|0\rangle \tag{A.7}$$

Now calculating the probability of photons being coincidence by taking its inner product with itself

$$P_C = \langle \Phi_c \,|\, \Phi_c \rangle = \frac{1}{4}\langle 0| \left(\hat{b}_4\hat{a}_3 - \hat{b}_3\hat{a}_4\right)\left(\hat{a}_3^\dagger\hat{b}_4^\dagger - \hat{a}_4^\dagger\hat{b}_3^\dagger\right)|0\rangle, \tag{A.8}$$

The different paths commute, however the same paths do not. this leaves us at the following formula after working through the algebra

$$P_C = \frac{1}{4}\langle 0| \left(\hat{a}_3\hat{b}_4\hat{a}_3^\dagger\hat{b}_4^\dagger - \hat{a}_3\hat{b}_4\hat{a}_4^\dagger\hat{b}_3^\dagger - \hat{a}_4\hat{b}_3\hat{a}_3^\dagger\hat{b}_4^\dagger + \hat{a}_4\hat{b}_3\hat{a}_4^\dagger\hat{b}_3^\dagger\right)|0\rangle. \tag{A.9}$$

Now, using the commutation relations we get:

$$P_C = \frac{1}{4}\langle 0| \left(\hat{a}_3\hat{a}_3^\dagger\hat{b}_4\hat{b}_4^\dagger - \hat{a}_3\hat{b}_4\hat{a}_4^\dagger\hat{b}_3^\dagger - \hat{a}_4\hat{b}_3\hat{a}_3^\dagger\hat{b}_4^\dagger + \hat{a}_4\hat{a}_4^\dagger\hat{b}_3\hat{b}_3^\dagger\right)|0\rangle \tag{A.10}$$

Using some factorization of the 2 distinct spatial modes, we can solve for the first and last term

$$\langle 0|\hat{a}_3\hat{a}_3^\dagger\hat{b}_4\hat{b}_4^\dagger|0\rangle = \langle 0|(1-\hat{n}_{a_3})(1-\hat{n}_{b_4})|0\rangle = 1, \tag{A.11}$$

And for the middle 2 terms:

$$\langle 0|\hat{a}_3\hat{b}_4\hat{a}_4^\dagger\hat{b}_3^\dagger|0\rangle = \langle 0|\hat{a}_3\hat{b}_3^\dagger\hat{b}_4\hat{a}_4^\dagger|0\rangle = \langle 0|\hat{a}_3\hat{b}_3^\dagger|0\rangle\langle 0|\hat{b}_4\hat{a}_4^\dagger|0\rangle = \langle a\,|\,b\rangle_3\,\langle b\,|\,a\rangle_4 = |\,\langle a\,|\,b\rangle\,|^2. \tag{A.12}$$

In the last step, we assume perfect beam split, meaning both outputs are identical and we do not care about the difference in paths 3 and 4. So, putting it all together:

$$P_C = \frac{1}{2}\left(1 - |\,\langle a\,|\,b\rangle\,|^2\right) \tag{A.13}$$

Now, this is interesting. This result shows that the strength of this HOM dip is decided by how indistinguishable the 2 input photons are. This means that this in-product between the 2 input photons can be easily calculated, for all its properties.

A.2. Derivation and visibility calculation: biphoton HOM interference

The reader is advised to first look at the previous derivation in appendix A.1, as this one is similar, however with less grindy mathematics.

Lets take our superposition and assume we have creation processes A and B as we did in the thesis.

$$|\Phi_{in} > | = \frac{|A\rangle + e^{i\phi}|B\rangle}{\sqrt{2}} \tag{A.14}$$

For this derivation we use our formalisms defined in section 2.1.3. As a reminder, $\bar{x}$ is the collection of parameters which can introduce distinguishability and the states $|A\rangle$ and $|B\rangle$ are defined using equations 2.14 and 2.15. These equations state:

$$\begin{aligned} |A\rangle &= \iint d\bar{x}\left[\mathcal{A}(\bar{x})\hat{a}_1^\dagger(\omega_s,\bar{x})\hat{a}_2^\dagger(\omega_i,\bar{x})|0\rangle\right] \\ |B\rangle &= \iint d\bar{x}\left[\mathcal{B}(\bar{x})\hat{a}_1^\dagger(\omega_i,\bar{x})\hat{a}_2^\dagger(\omega_s,\bar{x})|0\rangle\right] \end{aligned} \tag{A.15}$$

Also, it is normalized for over the full parameter space $\bar{x}$

$$\iint \mathcal{A}^*(\bar{x})\mathcal{A}(\bar{x})d\bar{x} = 1. \tag{A.16}$$

We introduce a delay τ in path 2, which is due to the controlled delay in our reference path resulting in a phase delay dependent on the angular frequency of the photon existing there.

$$|\Phi_{in}\rangle = \frac{1}{\sqrt{2}}\iint d\bar{x}\left[e^{i\omega_i\tau}\mathcal{A}(\bar{x})\hat{a}_1^\dagger(\omega_s,\bar{x})\hat{a}_2^\dagger(\omega_i,\bar{x}) + e^{i\phi}e^{i\omega_s\tau}\mathcal{B}(\bar{x})\hat{a}_1^\dagger(\omega_i,\bar{x})\hat{a}_2^\dagger(\omega_s,\bar{x})\right]|0\rangle \tag{A.17}$$

To get the state at the output of the beam splitter, we apply beam splitter transform from beam splitter inputs 1 and 2 to outputs 3 and 4 described in equation A.4

$$\begin{aligned}|\Phi_{out}\rangle = \frac{1}{\sqrt{2}}\iint d\bar{x}\Bigg[&\frac{1}{2}e^{i\omega_i\tau}\mathcal{A}(\bar{x})\Big(\hat{a}_3^\dagger(\omega_s,\bar{x})\hat{a}_4^\dagger(\omega_i,\bar{x}) - \hat{a}_4^\dagger(\omega_s,\bar{x})\hat{a}_3^\dagger(\omega_i,\bar{x})\\ &-i\big(\hat{a}_3^\dagger(\omega_s,\bar{x})\hat{a}_3^\dagger(\omega_i,\bar{x}) + \hat{a}_4^\dagger(\omega_s,\bar{x})\hat{a}_4^\dagger(\omega_i,\bar{x})\big)\Big)\\ &+e^{i\phi}\frac{1}{2}e^{i\omega_s\tau}\mathcal{B}(\bar{x})\Big(\hat{a}_3^\dagger(\omega_i,\bar{x})\hat{a}_4^\dagger(\omega_s,\bar{x}) - \hat{a}_4^\dagger(\omega_i,\bar{x})\hat{a}_3^\dagger(\omega_s,\bar{x})\\ &-i\big(\hat{a}_3^\dagger(\omega_i,\bar{x})\hat{a}_3^\dagger(\omega_s,\bar{x}) + \hat{a}_4^\dagger(\omega_i,\bar{x})\hat{a}_4^\dagger(\omega_s,\bar{x})\big)\Big)\Bigg]|0\rangle\end{aligned} \tag{A.18}$$

Now, we take only the part of the state which results in a coincidence measurement $|\Phi_C\rangle$. That is, the part of the output state which produces a photon in both output 3 and output 4

$$\begin{aligned}|\Phi_C\rangle = \frac{1}{\sqrt{2}}\iint d\bar{x}\Bigg[&\frac{1}{2}e^{i\omega_i\tau}\mathcal{A}(\bar{x})\Big(\hat{a}_3^\dagger(\omega_s,\bar{x})\hat{a}_4^\dagger(\omega_i,\bar{x}) - \hat{a}_4^\dagger(\omega_s,\bar{x})\hat{a}_3^\dagger(\omega_i,\bar{x})\Big)\\ &+e^{i\phi}\frac{1}{2}e^{i\omega_s\tau}\mathcal{B}(\bar{x})\Big(\hat{a}_3^\dagger(\omega_i,\bar{x})\hat{a}_4^\dagger(\omega_s,\bar{x}) - \hat{a}_4^\dagger(\omega_i,\bar{x})\hat{a}_3^\dagger(\omega_s,\bar{x})\Big)\Bigg]|0\rangle\end{aligned} \tag{A.19}$$

We can calculate the coincidence probability $P_c = \langle\Phi_c\,|\,\Phi_c\rangle$. We split each product term into its own integral to make it easier to read. We also introduce $\Delta = \omega_s - \omega_i$. In the self interacting cases, we see that the phase due to τ disappears:

$$\begin{aligned}P_c = \frac{1}{8}\iint d\bar{x}\mathcal{A}^*(\bar{x})\mathcal{A}(\bar{x})\langle 0|&\Big(\hat{a}_4(\omega_i,\bar{x})\hat{a}_3(\omega_s,\bar{x}) - \hat{a}_3(\omega_i,\bar{x})\hat{a}_4(\omega_s,\bar{x})\Big)\\ &\times\Big(\hat{a}_3^\dagger(\omega_s,\bar{x})\hat{a}_4^\dagger(\omega_i,\bar{x}) - \hat{a}_3^\dagger(\omega_i,\bar{x})\hat{a}_4^\dagger(\omega_s,\bar{x})\Big)|0\rangle\\ +e^{i[(\Delta)\tau+\phi]}\frac{1}{8}\iint d\bar{x}\mathcal{A}^*(\bar{x})\mathcal{B}(\bar{x})\langle 0|&\Big(\hat{a}_4(\omega_i,\bar{x})\hat{a}_3(\omega_s,\bar{x}) - \hat{a}_3(\omega_i,\bar{x})\hat{a}_4(\omega_s,\bar{x})\Big)\\ &\times\Big(\hat{a}_3^\dagger(\omega_i,\bar{x})\hat{a}_4^\dagger(\omega_s,\bar{x}) - \hat{a}_4^\dagger(\omega_i,\bar{x})\hat{a}_3^\dagger(\omega_s,\bar{x})\Big)|0\rangle\\ +e^{-i[(\Delta)\tau+\phi]}\frac{1}{8}\iint d\bar{x}\mathcal{B}^*(\bar{x})\mathcal{A}(\bar{x})\langle 0|&\Big(\hat{a}_4(\omega_s,\bar{x})\hat{a}_3(\omega_i,\bar{x}) - \hat{a}_3(\omega_s,\bar{x})\hat{a}_4(\omega_i,\bar{x})\Big)\\ &\times\Big(\hat{a}_3^\dagger(\omega_s,\bar{x})\hat{a}_4^\dagger(\omega_i,\bar{x}) - \hat{a}_3^\dagger(\omega_i,\bar{x})\hat{a}_4^\dagger(\omega_s,\bar{x})\Big)|0\rangle\\ +\frac{1}{8}\iint d\bar{x}\mathcal{B}^*(\bar{x})\mathcal{B}(\bar{x})\langle 0|&\Big(\hat{a}_4(\omega_s,\bar{x})\hat{a}_3(\omega_i,\bar{x}) - \hat{a}_3(\omega_s,\bar{x})\hat{a}_4(\omega_i,\bar{x})\Big)\\ &\times\Big(\hat{a}_3^\dagger(\omega_i,\bar{x})\hat{a}_4^\dagger(\omega_s,\bar{x}) - \hat{a}_3^\dagger(\omega_s,\bar{x})\hat{a}_4^\dagger(\omega_i,\bar{x})\Big)|0\rangle\end{aligned} \tag{A.20}$$

Working out the commutator relationships assuming different paths and different wavelengths commute, we get:

$$\begin{aligned}P_c = \frac{1}{4}\iint d\bar{x}\mathcal{A}^*(\bar{x})\mathcal{A}(\bar{x}) - e^{i[(\Delta)\tau+\phi]}\frac{1}{4}\iint d\bar{x}\mathcal{A}^*(\bar{x})\mathcal{B}(\bar{x})\\ -e^{-i[(\Delta)\tau+\phi]}\frac{1}{4}\iint d\bar{x}\mathcal{B}^*(\bar{x})\mathcal{A}(\bar{x}) + \frac{1}{4}\iint d\bar{x}\mathcal{B}^*(\bar{x})\mathcal{B}(\bar{x})\end{aligned} \tag{A.21}$$

Now we can simplify, using the fact that the amplitudes are normalized. We also state, that ϕ is the phase between the 2 states. This implies that we can choose the integral of $\iint d\bar{x}\mathcal{B}^*(\bar{x})\mathcal{A}(\bar{x})$ to be real valued. Also notice how the second and third term are each others complex conjugate. Using this information we can rewrite:

$$P_c = \frac{1}{2} - 2\text{Re}\left[e^{i[(\Delta)\tau+\phi]}\frac{1}{4}\iint d\bar{x}\mathcal{A}^*(\bar{x})\mathcal{B}(\bar{x})\right] \tag{A.22}$$

Finally, we can conclude that:

$$P_c = \frac{1}{2} - \frac{1}{2}\cos\left(\Delta\tau + \phi\right)\left|\iint d\bar{x}\mathcal{A}^*(\bar{x})\mathcal{B}(\bar{x})\right| \tag{A.23}$$

Here the absolute value over the integral is taken to make sure that all global phase information is accounted for in ϕ.

B

Derivation of the temporal envelope

In this appendix we will discuss the temporal representation of the biphoton amplitude as a first step towards the temporal envelope.

We take the consideration of temporal overlap similar to Trojek [12]. We will lower the dimensionality of the spectral amplitude similarly as we did with the spectral amplitude. To make this work we need to transform τ_s and τ_i to $\tau_+ = \frac{\tau_s+\tau_i}{2}$ and $\tau_- = \frac{\tau_s-\tau_i}{2}$. The interpretation of these quantities is that τ_+ is the average arrival time of the signal and idler photon of a single creation process, while τ_- being the difference in arrival time between the signal and idler inside of the creation process. A visualization can be seen in figure B.1.

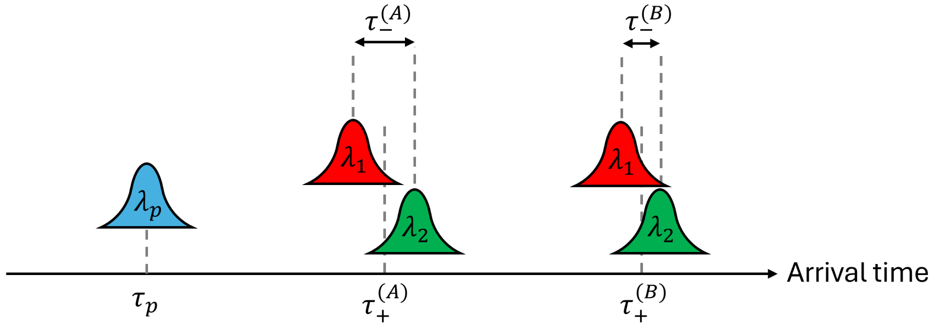

Figure B.1: Visualization of photon arrival times of 2 different processes A and B. The width of each photon envelope is a visualization of the single photon coherence time.

In our CW approximation we assume that the pump photon has a negligible small linewidth. This results in a long coherence time, with the corresponding coherence length being in the meter scale. This coherence length can be seen as uncertainty in the pump photon arrival time, which introduces an equivalent uncertainty in the average downconverted photon arrival time τ_+, implying a stretching of the downconverted photon amplitude in the τ_+ direction [12].

From here one can see that we cannot have distinguishability due to τ_+ as long as the difference in average arrival time of both processes $\tau_+^{(A)}$ and $\tau_+^{(B)}$ is small in comparison to the pump coherence time. We result in the temporal overlap of

$$\iint \mathcal{A}_\tau^*(\tau_s,\tau_i)\mathcal{B}_\tau(\tau_s,\tau_i)d\tau_s\tau_i = \int \mathcal{A}_\tau^*(\tau_-)\mathcal{B}_\tau(\tau_-)d\tau_- \tag{B.1}$$

Up to now we have discussed 2 creation processes, however we can find one more interesting thing when we consider what happens to our biphoton amplitudes when we add a delay τ in path 2 for our interferometry. This delays the idler of creation process A and the signal of process B. the states $|A\rangle$ and $|B\rangle$ are defined using equations 2.14 and 2.15.

Assuming for convenience $\tau > 0$ results in the idler photon being delayed for process A and the signal photon for process B. For CW pumped processes, the temporal amplitude is temporally only dependent on the relative arrival time of the photons $\tau_- = \tau_s - \tau_i$. From here we can effectively describe the effects of the delay τ on the partial amplitude functions:

This is also reflected in our state amplitudes, resulting in the transformations:

$$\begin{aligned} \mathcal{A}_\tau(\tau_-) &\to \mathcal{A}_\tau(\tau_- - \tau) \\ \mathcal{B}_\tau(\tau_-) &\to \mathcal{B}_\tau(\tau_- + \tau) \end{aligned} \tag{B.2}$$

This will result in an equal and opposite shift in the τ_- axis for both amplitude functions. From here we can rewrite equation 2.17 to:

$$P_c = \frac{1}{2} - \frac{1}{2}\alpha \cos(\Delta\tau + \phi) \left| \iint d\tau_- \mathcal{A}^*(\tau_- + \tau)\mathcal{B}(\tau_- - \tau) \right| \tag{B.3}$$

where we define α as the amplitude overlap due to nontemporal parameters. The integral resembles a convolution. The temporal shape is related to the Fourier transform of the downconverted spectrum. When one assumes spectral normally distributed downconverted photons we reproduce equation 2.2. Another common spectral amplitude shape is the sinc function. This results in a triangle based envelope. Both these resulting envelopes agree with degenerate HOM interferometry with the same spectra [7].

One thing we can see from equation B.3 is that HOMI does occur even when both signal and idler are temporally separated. That is, the τ_- for which the $\mathcal{A}_\tau(\tau_-)$ is nonzero being larger than both the signal and idler coherence time. This does agree with degenerate temporally separated HOMI experimental results [44, 45].

Here we have a problem with the arrival times of the photons. We found out it works differently than we first expected. Interference occurs even when signal and idler do not temporally overlap ($\tau_- >$coherence time). Only distinguishability between the 2 creation amplitudes is important.

C

Derivation Fisher based estimator

C.1. Fisher information

This HOMI measurement is based on making a maximum likelihood estimator (MLE) based on Fisher information. All the definitions and theorems are taken from the statistics book from Bijma [15].

Fisher information gives an upper bound on the information you can gain from a measurement, based on the probabilities attached to them. A biphoton event has 3 possible outcomes. Either 2, 1 or 0 photons end up getting detected, given a delay τ.

Given a measurement X:

$$P_\tau(X) = P_{\tau,0}(X)P_{\tau,1}(X)P_{\tau,2}(X) \tag{C.1}$$

$\dot{l}_\Theta(X)$ is the score function. which is the derivative of the log of the likelihood.

$$\dot{l}_\tau(X) = \sum_{i=0,1,2} \partial_\tau \log P_\tau(X = i) \tag{C.2}$$

Solving this differential equation and moving around some terms we get:

$$\dot{l}_\tau(X) = \frac{\partial_\tau P_0}{P_0} + \frac{\partial_\tau P_1}{P_1} + \frac{\partial_\tau P_2}{P_2} \tag{C.3}$$

Now, the Fisher information is defined as the variance with respect to the distribution parameter τ.

$$F_\tau = \mathsf{E}_\tau\left[\left(\dot{l}_\tau(X_1)\right)^2\right] \tag{C.4}$$

This expected value we can easily take, by taking a weighted average over the 3 outcomes (subscripts 0, 1 and 2) we can work out the formula for the Fisher information:

$$F_\tau = \frac{(\partial_\tau P_2(\tau))^2}{P_2(\tau)} + \frac{(\partial_\tau P_1(\tau))^2}{P_1(\tau)} + \frac{(\partial_\tau P_0(\tau))^2}{P_0(\tau)}. \tag{C.5}$$

When looking at equation 2.9 we see $\partial_\tau P_0(\tau) = 0$. Using this information we can simplify equation C.5 to get:

$$F_\tau = \frac{P_1(\tau)(\partial_\tau P_2(\tau))^2 + P_2(\tau)(\partial_\tau P_1(\tau))^2}{P_1(\tau)P_2(\tau)} \tag{C.6}$$

Here we once again look at equation 2.9 and see $\partial_\tau P_1(\tau) = -\partial_\tau P_2(\tau)$ which implies $(\partial_\tau P_1(\tau))^2 = (\partial_\tau P_2(\tau))^2$. We can than further simplify to get:

$$F_\tau = \frac{[P_1(\tau)+P_2(\tau)](\partial_\tau P_2(\tau))^2}{P_1(\tau)P_2(\tau)} \tag{C.7}$$

Also, from equation 2.9: $[P_1(\tau)+P_2(\tau)=1-P_0(\tau)=1-\gamma_s\gamma_i$

$$F_\tau = \frac{(1-\gamma_s\gamma_i)(\partial_\tau P_2(\tau))^2}{P_1(\tau)P_2(\tau)} \tag{C.8}$$

Now we need to calculate the derivative of $P_2(\tau)$

$$\partial_\tau P_2(\tau) = \frac{1}{2}(1-\gamma_s)(1-\gamma_i)\alpha\left[\Delta\sin(\Delta\tau)-2\sigma^2\cos(\Delta\tau)\right]e^{-2\sigma^2\tau} \tag{C.9}$$

Squaring this and substituting it gives rise to

$$F_\tau = \frac{(1-\gamma_s\gamma_i)\alpha^2(1-\gamma_s)^2(1-\gamma_i)^2\left[\Delta\sin(\Delta\tau)+2\sigma^2\cos(\Delta\tau)\right]^2 e^{-4\sigma^2\tau^2}}{4P_1(\tau)P_2(\tau)} \tag{C.10}$$

Also subbing in $P_1(\tau)$ and $P_2(\tau)$ gives

$$F_\tau = \frac{(1-\gamma_s\gamma_i)\alpha^2\left[\Delta\sin(\Delta\tau)+2\sigma^2\tau\cos(\Delta\tau)\right]^2 e^{-4\sigma^2\tau^2}}{\left[\frac{3\gamma_s-1}{1-\gamma_s}+\frac{2}{1-\gamma_i}-\alpha\cos(\Delta\tau)e^{-2\sigma^2\tau^2}\right]\left[1+\alpha\cos(\Delta\tau)e^{-2\sigma^2\tau^2}\right]} \tag{C.11}$$

C.2. Maximum Likelihood Estimator

Now, to try and saturate the QCR bound, we make an estimator of τ based on the measurement of coincidences and bunched events, for which the probabilities are given by equation 2.9. We show that we can define this estimator, and show that the uncertainty (in perfect conditions) will give an uncertainty equal to the QCR bound.

The maximum likelihood estimator is an estimator of a quantity. The precision of this is given by $\frac{1}{\sqrt{F_\tau}}$. Now, we want our measurement to be as precise as possible, so, for this, we need to find a maximum of the likelihood function

$$\mathcal{L}(N_0, N_1, N_2 \mid T) \propto P_0(T)^{N_0}P_1(T)^{N_1}P_2(T)^{N_2} \tag{C.12}$$

Here, $N_{0/1/2}$ are the number of events resulting in 0/1/2 detectors clicking. To find a maximum of this function, we take the derivative with respect to τ, and take the log of the likelihood for simplicity of calculation. This results in

$$0 := (\partial_\tau \log\mathcal{L})_{\tilde{\tau}_{\text{MLE}}} = \frac{N_0P_0'(\tau)}{P_0(\tau)}+\frac{N_1P_1'(\tau)}{P_1(\tau)}+\frac{N_2P_2'(\tau)}{P_2(\tau)}, \tag{C.13}$$

When looking at equation 2.6 we see $\partial_\tau P_0(\tau)=0$ and $\partial_\tau P_1(\tau)=-\partial_\tau P_2(\tau)$. So, given that $\partial_\tau P_1(\tau)\neq 0$. from this we can determine an estimator $\tilde{\tau}_{MLE}$ for which the equation above is satisfied, meaning this is the MLE estimator.

$$N_1P_2(\tau)|_{\tilde{\tau}_{MLE}} = N_2P_1(\tau)|_{\tilde{\tau}_{MLE}} \tag{C.14}$$

which allows us to determine the estimator $\tilde{\tau}_{MLE}$ For the case of both photons having the same photon loss γ this results in

$$\hat{\tau}_{\text{MLE}} = \arccos\left(\frac{\frac{1+3\gamma}{1-\gamma}N_2-N_1}{\alpha(N_1+N_2)e^{-2\sigma^2\tau_s}}\right)/\Delta \tag{C.15}$$

Using equation 2.9 for the case of different photon losses for the signal and idler photon, this results in;

$$\widehat{\tau} = \arccos\left(\frac{\left(\frac{3\gamma_s-1}{1-\gamma_s}+\frac{2}{1-\gamma_i}\right)N_2-N_1}{\alpha(N_1+N_2)e^{-2\sigma^2\tau_s}}\right)/\Delta \tag{C.16}$$

D

Reasoning for photonloss based on single sided heralding

First we will look at the single sided heralding ratio as defined by Bennink [23].

$$\eta_s \equiv \frac{R_{si}}{R_s} \tag{D.1}$$

Which can be interpreted as the probability that the idler photon is in a measurable mode, given that the signal photon is in one. In a similar fashion, η_i is defined. R_s is the brightness of only signal photons in a measurable mode. An important note is that $R_s \geq R_{si}$ always holds. The reason is that a detection event where both signal and idler are in a measurable mode always implies that the signal is in a measurable mode. This results in the heralding ratio always being between 0 and 1, making it interpretable as a probability.

Now, we define the event of the signal photon being in a measurable mode as S. For the idler, we define I similarly. Using the reasoning from the previous paragraph, we can write the conditional probability:

$$\eta_s = P(I|S) \tag{D.2}$$

$P(S)$ is the probability of the signal photon not being lost, which equates to $1 - \gamma_s$. $P(I)$ can be found similarly From here we can use some Baisian probability theory to find

$$\eta_s = P(I|S) = \frac{P(I \cap S)}{P(S)} = \frac{(1-\gamma_i)(1-\gamma_s)}{1-\gamma_s} = 1 - \gamma_i \tag{D.3}$$

Similarly, we find $\eta_i = 1 - \gamma_s$

E

Proof of equivalence between conventional and single input HOMI

In this proof we show that 2 photons entering a beam splitter from each side is equivalent to 2 photons with (anti)diagonally D(A) polarized photon entering a PBS in a single spatial mode. We show that the beam splitter transformation on the incoming photon pair results in an identical output for both situations.

We argue from the operator level; the A (anti)diagonally D(A) polarized photon annihilation operator are.

$$\hat{a}_{1,D} = \frac{\hat{a}_{1,H} + \hat{a}_{1,V}}{\sqrt{2}} \quad \hat{a}_{1,A} = \frac{\hat{a}_{1,H} - \hat{a}_{1,V}}{\sqrt{2}} \tag{E.1}$$

Now we assume the PBS to be defined similarly to the ideal beam splitter from appendix A.3. The only difference being the transmission and reflection coefficients, which are dependent on the polarization of the photons

$$\hat{a}_1 \to t\hat{a}_3 + ir\,\hat{a}_4 \quad \hat{a}_2 \to t\hat{a}_4 + ir\,\hat{a}_3 \tag{E.2}$$

We can model a perfect PBS where the horizontal polarization gets transmitted choosing t and r:

$$t = \begin{cases} 1, & \text{if pol} = H \\ 0, & \text{if pol} = V \end{cases} \quad \text{and} \quad r = \begin{cases} 0, & \text{if pol} = H \\ 1, & \text{if pol} = V \end{cases}$$

We use this beam splitter transformation for the diagonal and anti-diagonal operators.

$$\hat{a}_{1,D} \to \frac{\hat{a}_{3,H} + i\,\hat{a}_{4,V}}{\sqrt{2}} \quad \hat{a}_{1,A} \to \frac{\hat{a}_{3,H} - i\,\hat{a}_{4,V}}{\sqrt{2}} \tag{E.3}$$

Now this is exact the same transformation, omitting a global phase for the anti-diagonal transformation as we would have had if we had both photons at different inputs at a non polarizing beam splitter. More explicitly, the mapping is identical to equation A.4.

The only thing we did not account for yet, is that in a normal beam splitter, it is important that $\hat{a}_1$ and $\hat{a}_2$ commute. Meaning $\hat{a}_{1,D}$ and $\hat{a}_{1,A}$ should also commute. This is easily proven as the A and D state are orthogonal.

Now that all conditions are met, we can conclude mathematical equivalence.

F

Other interferometer designs

In this chapter of the appendix we start with some general remarks for the interferometer designs. These remarks are not of importance for the main body of this thesis, but we add them for completeness.

Beam separation and angle of incidence

The designs in the main body of this thesis had no need to consider the following experimental restrictions. However, every of the designs mentioned in this chapter does need at least one of these:

- parallel beams should be separated by at least 3 times their beam diameter.
- angle of incidence at the sample is at most 6 degrees

The beam separation is needed to prevent crosstalk between both beams as Gaussian beams do not abruptly stop existing outside of their diameter.

A small angle on the sample is needed to prevent noticeable differences in Fresnel reflections between the 2 paths and the 2 frequencies. Below 6 degrees, the difference between S and P reflectivity, is negligible.

The polarization state of both arms should also have the same polarization considering the angle of incidence on the sample.

Dichroic mirrors

As a last point, we advise to use dichroic mirror cubes for the interferometer and source of the experiment whenever a dichroic mirror is mentioned. Generally, dichroic mirrors reflect on a singular surface of a glass of crystal substrate. This substrate does introduce some spatial walk-off between the signal and idler photons due to chromatic effects as can be seen in figure F.1. Even worse, the walk-off is different for both inputs of the mirror. Only one input needs to travel through the substrate before reaching the mirror. All these different kinds of spatial walk-off can be prevented with dichroic mirror cubes, which function similar to the more conventional PBS cubes. The spatial walk-off in conventional dichroic mirrors is even worse when we use both inputs of the mirror.

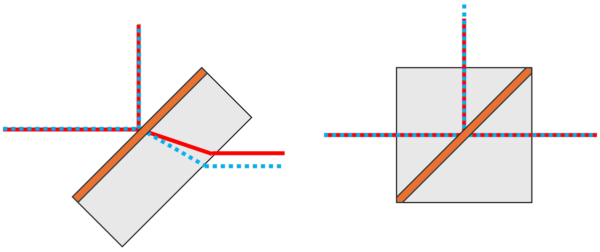

Figure F.1: Qualitative example of standard mirror vs cubed mirror walk-off due to chromatic dispersion in the substrate of a light beam entering from the left.

F.1. Tilted dual sample interferometer

Please look at the beginning of this appendix chapter for some extended restrictions compared to the main body of the thesis.

The scanning design shown in F.2 uses 2 periscopes (P). In contrast to the single sample setup we are not limited to small elevations of the beams. This is due to the fact of the elevation that is only applied to cross the beams, and not to scan the sample at 2 different locations. We can choose them to a height difference of a few centimeter, which we can easily work with. Both reference and sample are at the same side of the setup, meaning we only need to allocate one part of the table to this empty long space. This design also is more modular, as we can easily make blocks of the different parts of the setup.

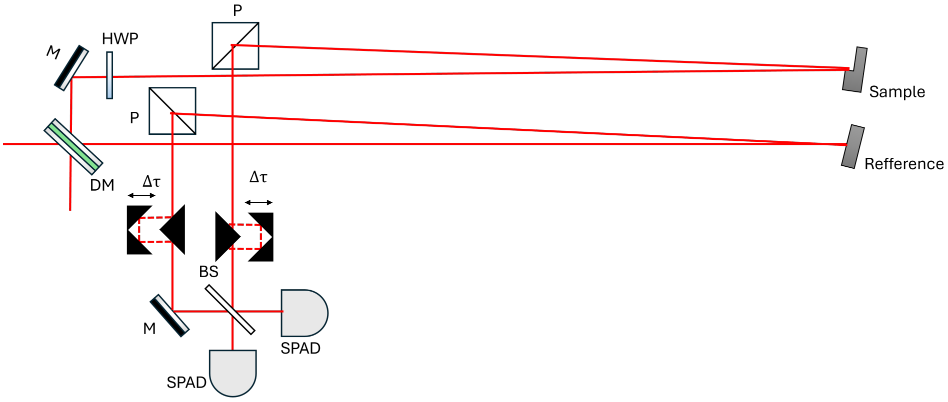

Figure F.2: Tilted dual sample interferometer design

One of the problems in this design is that the distances to the sample and reference need to be large, making alignment more complicated.

F.2. Tilted single sample interferometer

Please look at the beginning of this appendix chapter for some extended restrictions compared to the main body of the thesis.

Complexities needed for the design shown in F.3 are the periscopes (P) and the knife edge mirrors (KEM).

Ideally we want to use dichroic mirrors as these have high efficiency. However, physically mounting them is a bit of a concern, as the housing of the mirrors might block the path. That is why we will be using clear edge mounts. Total internal reflection prisms also are a good alternative. One remark about these is that these also introduce a group velocity mismatch between the signal and idler photons. This can however be compensated for by making the compensation KTP crystal longer.

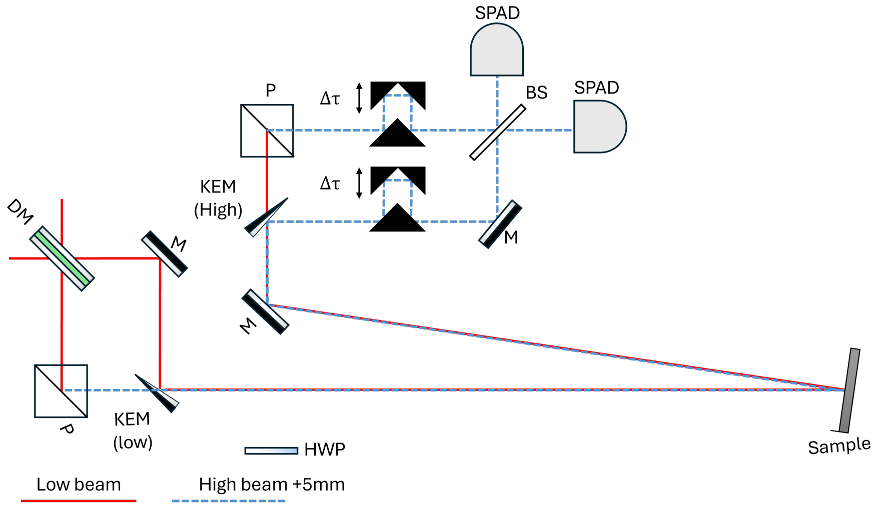

Figure F.3: Tilted single sample interferometer design

F.3. Prism based single sample interferometer

Please look at the beginning of this appendix chapter for some extended restrictions compared to the main body of the thesis.

We have a prism based single sample setup, which is further discussed in appendix F.3. This one was a contender, however it still had some major flaws. 2 spots on the sample where located diagonally, making the displacement in the vertical and horizontal direction even smaller and harder to work with.

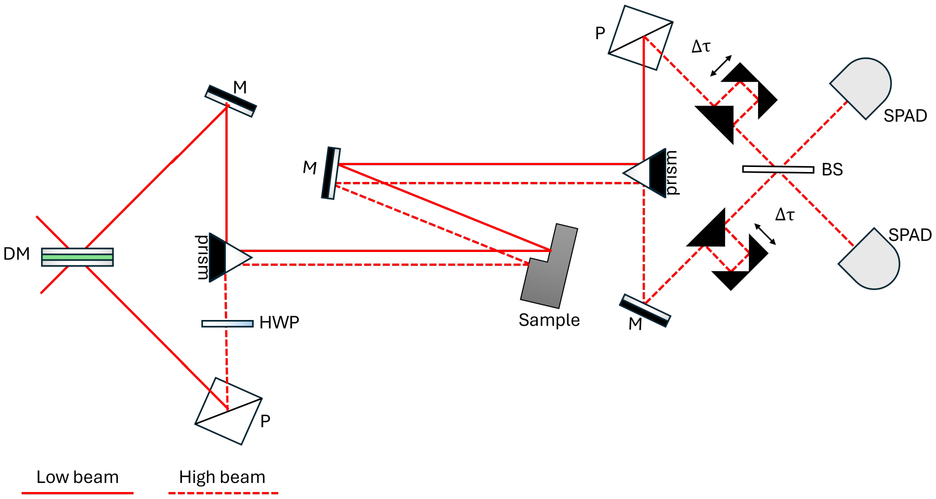

Figure F.4: Prism based single sample interferometer design

F.4. Lens-based single sample interferometer

Please look at the beginning of this appendix chapter for some extended restrictions compared to the main body of the thesis.

One idea we had was using the Fourier plane of a large aperture lens. Here we can control the separation of the focal points by choosing the incident angle of a beam on the lens. Beam crossings can be prevented by giving one beam an offset in the horizontal axis compared to the optical axis, while the other one has a vertical offset. The problem with this, is that the setup gets far more complicated as can be seen in figure F.4. 3 distinct heights need to be determined. Having identical component angles and path length also made this design far too complicated.

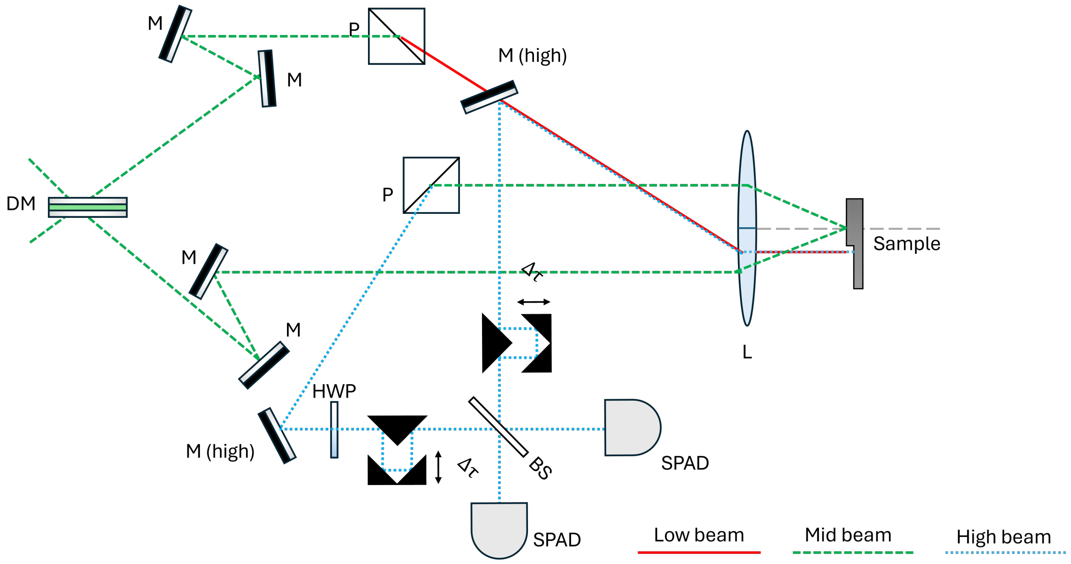

Figure F.5: Lens based single sample interferometer design

F.5. Beam displacer based single sample interferometer

Please look at the beginning of this appendix chapter for some extended restrictions compared to the main body of the thesis.

Here we discuss a design with some major advantages. A lot is common path, there is no angled reflectance at the sample and the full optical path is at a single height. This design is inspired by the beam displacer-based photon sources [28, 24]. We assume our entangled light to be in a single spatial mode, with entangled polarization and in the H and V basis. In figure F.6 you can see the suggested interferometer. Here we separate the 2 polarizations using the same orthogonally placed beam displacer. This separation is used to probe both sides of the step on the sample.
To separate the illumination and the collection from/to the sample we use a similar trick with a QWP as we did in the interferometer in the main script of this thesis. Reflecting directly to the sample would normally result in the light returning to the single spatial mode. However, if we change all polarizations with QWP at 45 degrees, which effectively is a HWP due to the double passing of the light, this behavior changes. Instead of returning to the same spatial location of the pump mode, we get a outgoing separation twice as large as it is on the sample. Choosing a 5mm beam separation at the sample results in a separation of 1cm for the outgoing beams. This is enough to separate the beams towards a further standard interferometer. We can even put the HOM beamsplitter and detectors after the sample, as this setup is rather compact.

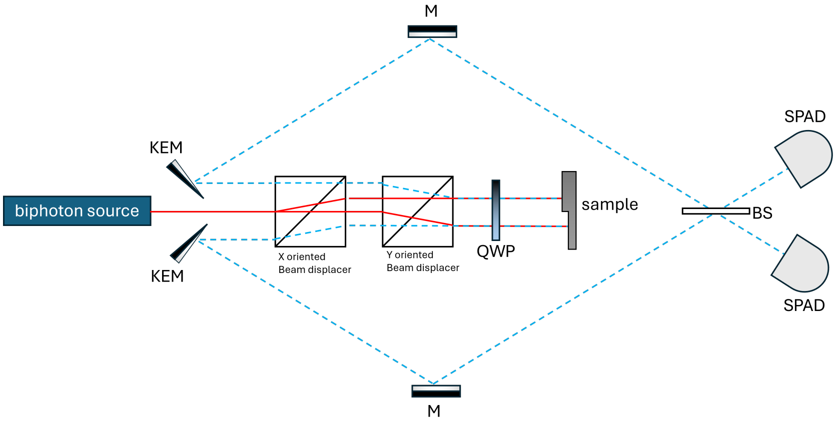

Figure F.6: Beam displacer based single sample interferometer.

Similarly to the beam displacer based photon sources, this design is limited by chromatic dispersive effects. For degenerate HOMI, this is not a problem, however, for a large detuning the signal and idler will experience wildly different refractive indexis resulting in different displacements. This problem could be solved with effective achromatic beam displacers made of multiple materials [29]. This does make the displacers longer, meaning more dispersive effects and more absorption. This interferometer becomes feasible with more engineered beam displacers however.

G

Other biphoton source design

G.1. PBS based biphoton source

Here we discuss the idea of a photon source without the need for temporal compensation. This method is similar to beam displacer from literature [24] setups. The problem of these displacer based setups is their need for dispersive components. Our design does not contain any of these components, and can be seen in figure G.1. The source for type-II can be seen in **a)** and type-0 in **b)**. The W prism (Wollaston prism) splits the horizontally and vertically polarized light by giving them different exit angles. A lens can then be used to make the light parallel again. Then, the light passes through the 2 ppKTP crystals, of which ppKTP2 is rotated by 90 degrees, making downconversion of vertical light possible. After the crystals, a long-pass filter (LP) is applied to filter out the pump light. Both beams get recombined using a Dichroic mirror (DM), resulting in 2 superposed states needed, with minimal which crystal information.

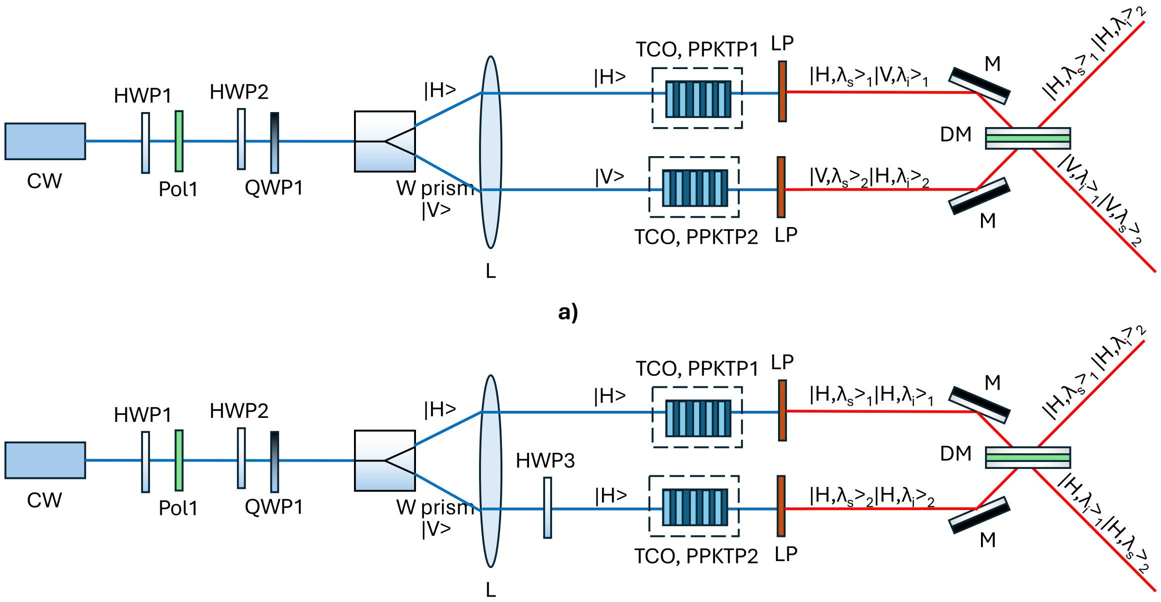

Figure G.1: Schematics for Wollaston based biphoton sources with 2 distinct spatial outputs. **a)** shows the design for type-2 SPDC and **b)** the adjusted design for type-0 SPDC.

We assume long-pass dichroic mirrors, which for large enough detunings should be easily available.

Conventionally $\lambda_s \leq \lambda_i$, meaning the signal photon will get reflected and the idler transmitted. Do note that the idler photons now get an extra phase due to its transmission through the dichroic mirror, which at first seems to make things complicated. Assuming we use the dichroic mirror cubes discussed at the beginning of appendix F, this will have no effect on the photon timing distinguishability, since this additional phase will be identical for both output paths.

We could also replace the Wollaston prism and lens configuration with a second PBS and 2 mirrors as can be seen in figure G.2. This is mostly about convenience, as the parts interacting with the pump beam before the crystals only apply a phase between the creation processes we can correct for.

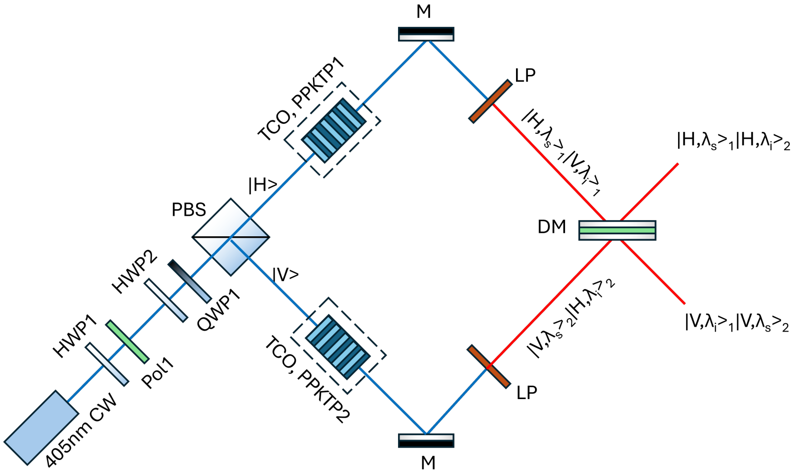

Figure G.2: Entangled photon source, with PBS instead of Wollaston and lens setup.

H

Diagnostic measure for a delay scan

We define how far a fit is from the data. From a scan we get $N_{2,fit}(z)$ and $N_{2,measure}(z)$ where z is the scanner position.

In measure theory [46], a commonly used measure of a function is the L2 norm:

$$||\bullet||_2 = \int \left(\bullet\right)^2 dx \tag{H.1}$$

The distance between functions can be measured with respect to a norm. For functions $f(x)$ and $g(x)$ the distance is given by

$$||f-g||_2 = \int_0^{L_x} \left(f(x)-g(x)\right)^2 dx \tag{H.2}$$

Where L_x is the integration window. We now define our relative distance LS as the distance between the measured and fitted coincidences, normalizing with respect to the measured coincidences

$$LS(z) = \frac{||N_{2,measured} - N_{2,fit}||_2}{||N_{2,measured}||_2} = \frac{\int_0^{L_z} \left(N_{2,measured}(z) - N_{2,fit}(z)\right)^2 dz}{\int_0^{L_z} \left(N_{2,measured}(z)\right)^2 dz} \tag{H.3}$$

Now, assuming our fit to be perfect, we can state that all deviations are due to the Poisson distributed noise in the measurement $(N_{2,measured} - N_{2,fit})^2 \approx \text{Var}[N_{2,measured}] = \lambda_m(z)$. where $\lambda_m(z)$ is the Poisson variable for a coincidence measurement.

$$LS \approx \int dz \left[\frac{\text{Var}[N_{2,measured}]}{N_{2,measured}^2}\right] = \frac{\lambda_2}{\lambda_2^2} = \frac{1}{\lambda_2} \tag{H.4}$$

This does go to zero as our average counts go higher. This metric is scale invariant. For example, if we have a relative error ϵ due to fitting ($N_{2,fit} = (1+\epsilon)N_{2,measured}$, we get measurement outcome:

$$LS(z) \approx \int dz \left[\frac{(\epsilon N_{2,measured})^2}{N_{2,measured}^2}\right] = \epsilon^2 \tag{H.5}$$

Do note that this is independent of the scale of λ, meaning that we do only compare this relative deviation ϵ to the fitting errors. Now, we can set a threshold where we accept a scan as sufficient for measurement. We will assume that LS should be smaller than 0.05 to consider a fit successful.

I

Optimized settings

The experiments are named based on the detection setup used, the type of SPDC (II/0), and whether the experiment is filtered or not (Fil./Unf.). All simulations assume 1 cm ppKTP for downconversion. The experimental and HOM parameters can be found in Table I.1, and the resulting measurement speed, pump power, and restrictions can be found in Table I.2.

	Experimental Parameters										HOM Parameters				
Experiment	λ_p [nm]	λ_s [nm]	λ_i [nm]	$\delta\lambda_s$ [nm]	$\delta\lambda_i$ [nm]	$w_{0,p}$ [μm]	ξ_p [-]	ξ_{si} [-]	f_p [mm]	f_c [mm]	α [-]	γ_s [-]	γ_i [-]	Δ [rad/s]	σ [rad/s]
Si+SNSPD II (Unf.)	396	561	1348	3	18	11.68	2.5	7.4	93	46	0.80	0.809	0.868	1.96×10^{15}	1.88×10^{13}
Si+SNSPD 0 (Unf.)	507	755	1542	3	12	13.04	2.5	5.8	81	44	0.80	0.821	0.871	1.28×10^{15}	9.30×10^{12}
Si+SNSPD II (Fil.)	396	561	1348	3	18	184.75	1.0×10^{-2}	1.8×10^{-1}	1466	293	0.90	0.856	0.861	1.96×10^{15}	1.88×10^{13}
Si+SNSPD 0 (Fil.)	507	755	1542	3	12	206.15	1.0×10^{-2}	1.1×10^{-1}	1278	316	0.90	0.845	0.854	1.28×10^{15}	9.30×10^{12}
Si+InGaAs II (Fil.)	402	548	1506	2	17	11.79	2.5	4.6	92	59	0.80	0.783	0.977	2.19×10^{15}	1.39×10^{13}
Si+InGaAs 0 (Fil.)	508	755	1555	3	12	13.06	2.5	2.8	81	63	0.80	0.804	0.980	1.29×10^{15}	9.27×10^{12}
Si+InGaAs II (Fil.)	402	548	1506	2	17	12.96	2.1	3.4	101	69	0.90	0.798	0.979	2.19×10^{15}	1.39×10^{13}
Si+InGaAs 0 (Fil.)	508	755	1555	3	12	206.44	1.0×10^{-2}	2.6×10^{-2}	1277	654	0.90	0.806	0.980	1.29×10^{15}	9.27×10^{12}
Si type-II (Unf.)	382	633	961	5	10	11.44	2.5	4.6	94	55	0.80	0.784	0.955	1.01×10^{15}	2.12×10^{13}
Si type-0 (Unf.)	464	827	1058	7	12	12.42	2.5	3.6	84	54	0.80	0.864	0.980	4.96×10^{14}	2.06×10^{13}

Table I.1: Experimental and HOM Parameters. The experimental parameters mentioned in this table are the operational wavelengths $\lambda_{p/s/i}$, Downconverted linewidth $\delta\lambda_{s/i}$, illumination spot size $w_{0,p}$, illumination, focusing criteria $\xi_{p/s}$ and collection focal length $f_{p/c}$

	Simulation Outcome				Pump power and relative saturation of the restriction				
Experiment	$t_{0.1nm}$ [s]	κ_{step} $[m^{-2}s^{-1}]$	F_z $[m^{-2}]$	HOM-rate $[s^{-1}]$	P_{opt} [mW]	$P_{opt}/P_{p,max}$ [-]	$P_{opt}/P_{s,max}$ [-]	$P_{opt}/P_{i,max}$ [-]	$P_{opt}/P_{w,max}$ [-]
Si+SNSPD II (Unf.)	1.09×10^1	2.06×10^{35}	3.95×10^{28}	5.22×10^6	15.06	0.54	1.00	0.69	0.52
Si+SNSPD 0 (Unf.)	2.63×10^1	8.54×10^{34}	1.53×10^{28}	5.58×10^6	3.38	0.10	1.00	0.72	0.56
Si+SNSPD II (Fil.)	7.41	3.04×10^{35}	4.38×10^{28}	6.93×10^6	842.37	0.12	1.00	0.96	0.69
Si+SNSPD 0 (Fil.)	1.66×10^1	1.36×10^{35}	2.10×10^{28}	6.45×10^6	179.87	0.02	1.00	0.94	0.65
Si+InGaAs II (Fil.)	5.45×10^1	4.13×10^{34}	9.37×10^{27}	4.40×10^6	16.59	0.58	0.96	1.00	0.88
Si+InGaAs 0 (Fil.)	1.75×10^2	1.29×10^{34}	2.57×10^{27}	5.00×10^6	2.62	0.08	0.98	1.00	1.00
Si+InGaAs II (Fil.)	4.14×10^1	5.43×10^{34}	1.16×10^{28}	4.68×10^6	18.24	0.53	0.95	1.00	0.94
Si+InGaAs 0 (Fil.)	1.25×10^2	1.80×10^{34}	3.62×10^{27}	4.97×10^6	186.78	0.02	0.96	1.00	0.99
Si type-II (Unf.)	1.43×10^2	1.58×10^{34}	3.96×10^{27}	3.97×10^6	4.97	0.19	1.00	1.00	0.79
Si type-0 (Unf.)	1.76×10^3	1.28×10^{33}	2.56×10^{26}	5.00×10^6	0.41	0.01	0.77	0.77	1.00

Table I.2: Measurement outcomes and saturation of the restrictions in pump power. The parameters shown in this table are the measurement time $t_{0.1nm}$ needed for a 0.1 nm standard deviation error of the step size estimation, speed of measure κ_{step}, the single measurement Fisher information F_z and the estimated downconverted photon rate HOM-rate. The optimal pump power P_{opt} is compared to the maximum allowed pump power due to experimental restrictions. These restrictions are the maximum allowed intensity inside the crystal ($P_{p,max}$), the signal/idler detector saturation ($P_{s/i,max}$) and finally the coincidence window saturation ($P_{w,max}$)